

Synthesis of heterogeneous catalysts with metal oxide overcoat for renewable catalysis applications

Présentée le 26 juin 2020

à la Faculté des sciences de base
Laboratoire des procédés durables et catalytiques
Programme doctoral en chimie et génie chimique

pour l'obtention du grade de Docteur ès Sciences

par

Yuan-Peng DU

Acceptée sur proposition du jury

Prof. K. Sivula, président du jury
Prof. J. Luterbacher, directeur de thèse
Prof. J. van Bokhoven, rapporteur
Prof. Ph. Christopher, rapporteur
Prof. O. Kröcher, rapporteur

Acknowledgements

The completion of this thesis would not have been possible without the invaluable helps from many people. First, I would like to express my gratitude to my thesis advisor Prof. Jeremy S. Luterbacher who has been guiding me throughout my PhD study and always gives me a high freedom to work on the projects that interest me. The way he organizes and gets research updates from the group is also very inspiring for me. I am also grateful to my thesis committee for the valuable suggestions and the funding from European Research Council. Many thanks to my outstanding collaborator Dr. Alimohammad Bahmanpour who helped me perform CO₂ hydrogenation measurements and many experts who gave me characterization supports, including Dr. Arnaud Magrez (XRD), Dr. Wen Hua Bi (XRD), Dr. Mounir D. Mensi (XPS), Dr. Pierre Mettraux (XPS), Dr. Natalia Gasilova (ICP), Dr. Emilie Baudat (ssNMR) and Tzu-Hsien Shen (TEM). I would also like to acknowledge all the current and former members in LPDC who have ever helped me in the Lab. Among them, my particular gratitude first goes to Dr. Florent E. Héroguel who has patiently taught me the necessary skillset for catalysis research since I arrived as a clueless rookie. In addition, I want to thank Luca Sivioli who is a super bright chemist and also taught me many things in science and beyond. I really enjoyed the time when developing the overcoating methods with him in my first year. Thank the master students I have taught, Nguyen Xuan Trung and Luka Milošević, for their great input to my projects. Besides, I am grateful to my several language teachers in the Lab including Dr. Graham Dick (English), Lorenz P. Manker (English), Stefania Bertella (Italian), Jessica Rohrbach (French) and Dr. Wu Lan (Cantonese). Lastly, special thanks to my alma maters, NTHU and NTU whose educations gave me an indispensable solid background for pursuing PhD, as well as my families, former band fellows, and friends in Taiwan and Switzerland who have been giving me tremendous spiritual supports during my time of studying abroad.

Abstract

Metal oxide deposition is an emerging synthetic technique for designing heterogeneous catalysts. Depositing a nanoscale overcoat of metal oxide on heterogeneous catalysts can modify their structural and chemical characteristics. Many deposition approaches, especially for coating transition metal oxides, have relied on atomic layer deposition (ALD). However, ALD requires an expensive instrument, large excesses of precursors and several purging steps. In this thesis, I present a novel kinetically controlled sol-gel strategy to overcoat heterogeneous catalysts. Using non-hydrolytic sol-gel (NHSG) or chelation chemistry, the hydrolysis/condensation rates of alumina precursor can be well-controlled, which enables us to overcoat alumina on high-surface-area catalysts with high uniformity that approaches what can be seen in ALD processes. Specifically, the chelation method was used to synthesize a sintering resistant $\text{Al}_2\text{O}_3@\text{Cu}/\text{Al}_2\text{O}_3$ catalyst, whose nanoparticles remained well-dispersed after five cycles of liquid phase furfural hydrogenation. In comparison, the application of NHSG pathway is to create more Lewis acid-Pt interfacial sites on $\text{Al}_2\text{O}_3@\text{Pt}/\text{SBA-15}$ and this catalyst could convert lignin-derived 4-propylguaiaicol to propyl cyclohexane with 87% selectivity via hydrodeoxygenation. The kinetic control can be extended to overcoat other transition metal oxides. Specifically, in Chapter 3 I describe the deposition of Nb_2O_5 on SBA-15, which results in a mesoporous solid acid catalyst. This $\text{Nb}_2\text{O}_5@\text{SBA-15}$ has a more thermally stable amorphous structure that prevents it from losing acidity during thermal regenerations at 500 °C. This niobia solid acid outperforms commercial niobia catalysts in both xylose dehydration and Friedel–Crafts alkylation due to its optimal Brønsted/Lewis acid ratio and favorable nanostructure. Lastly, I describe the synthesis of an atomically dispersed material using metal coordination complex. The metal-metal oxide interface of this material can be further engineered using sol-gel overcoating techniques. In contrast to the deposition on

catalysts with nanoparticles, overcoating the material with atomically dispersed Pd before reductive treatment enabled us to limit the particle growth during thermal activation steps, yielding highly accessible, sinter-resistant Pd clusters less than 2 nm in diameter. Notably, engineering the Pd-ZrO₂ interface of Pd/ZrO₂ into inverted ZrO₂-Pd interface using ZrO₂ overcoat leads to an unprecedented 100% CO selectivity during CO₂ hydrogenation. The results of this thesis show that sol-gel based overcoating is a promising, quick and straightforward strategy for designing robust and selective heterogeneous catalysts for a wide range of sustainable applications.

Keywords: nanostructured catalyst, metal oxide deposition, sol-gel chemistry, biomass conversion, CO₂ hydrogenation.

Résumé

Le dépôt d'oxydes métalliques est une technique de synthèse émergente pour la conception de catalyseurs hétérogènes. Déposer une couche nanométrique d'oxyde métallique sur un catalyseur métallique supporté peut modifier ses caractéristiques structurales et chimiques. De nombreuses approches de dépôt, en particulier pour l'enrobage d'oxydes de métaux de transitions, se basent sur le dépôt de couches atomiques (*atomic layer deposition* - ALD). Cependant, l'ALD nécessite une instrumentation coûteuse, un large excès de précurseurs et plusieurs étapes de purge. Dans cette thèse, je présente une nouvelle stratégie sol-gel contrôlée cinétiquement pour l'enrobage de catalyseurs hétérogènes. En utilisant les chimies du sol-gel non hydrolytique ou de la chélation, les vitesses d'hydrolyse/condensation d'un précurseur d'alumine peuvent être bien contrôlées, ce qui nous permet de déposer de l'alumine sur des catalyseurs à haute surface spécifique avec hautes conformités et uniformités, proches de ce qui est observé avec le procédé ALD. Cette méthode a été utilisée pour synthétiser un catalyseur $\text{Al}_2\text{O}_3@\text{Cu}/\text{Al}_2\text{O}_3$ résistant au frittage pour l'hydrogénation du furfural en phase liquide et un catalyseur $\text{Al}_2\text{O}_3@\text{Pt}/\text{SBA-15}$ hautement actif pour l'hydrodéoxygénation sélective de monomères de lignine. Plus important encore, le contrôle cinétique peut être étendu pour le dépôt d'autres oxydes de métaux de transitions. Spécifiquement, je décris par la suite que le dépôt de Nb_2O_5 sur SBA-15 peut conduire à un catalyseur acide solide mésoporeux. $\text{Nb}_2\text{O}_5@\text{SBA-15}$ possède une structure amorphe qui évite la perte d'acidité lors des régénérations thermiques. Cet oxyde de niobium acide surpasse le catalyseur d'oxyde de niobium commercial pour la déshydratation du xylose et l'alkylation de Friedel-Crafts grâce à son équilibre idéal entre sites acides de Brønsted et de Lewis. Finalement, je décris la synthèse d'un matériau atomiquement dispersé en utilisant un complexe de coordination métallique. L'interface métal – oxyde métallique de ce matériau peut être modifiée en utilisant des

techniques d'enrobage sol-gel suivis d'une réduction pour former un catalyseur aux propriétés sur-mesure. A l'inverse du dépôt de nanoparticules sur un catalyseur, l'enrobage de ce matériau avant le traitement réducteur peut limiter la croissance des particules pendant l'étape d'activation thermique, produisant des clusters de palladium inférieurs à 2 nm, résistant au frittage et hautement accessibles. En particulier, le contrôle de l'interface Pd-ZrO₂ au sein de Pd/ZrO₂ pour former une interface inversée ZrO₂-Pd grâce à un enrobage mène à une sélectivité sans précédent de 100% vers le monoxyde carbone durant l'hydrogénation du CO₂. Les résultats de cette thèse montrent que l'enrobage sol-gel est une stratégie prometteuse, rapide et simple pour la conception de catalyseurs hétérogènes robustes et sélectifs.

Mots-clés: catalyseur nano-structuré, dépôt d'oxyde métallique, réaction sol-gel, conversion de la biomasse, hydrogénation du CO₂

Astratto

Depositare ossidi di metalli è una tecnica emergente nella sintesi di catalizzatori eterogenei. Quando uno strato di un ossido di metallo dell'ordine di grandezza del nanometro viene depositato su un catalizzatore eterogeneo, le caratteristiche strutturali e chimiche di quest'ultimo possono variare. Molti approcci di deposizione sviluppati finora, specialmente per il rivestimento con metalli di transizione, hanno fatto affidamento sulla deposizioni di strati atomici (ALD). Tuttavia questa tecnica richiede una strumentazione costosa, un grande eccesso di precursori e molti passaggi di spurgo per eliminare tali precursori in eccesso.

In questa tesi presento una nuova strategia a controllo cinetico per il rivestimento di catalizzatori eterogenei. Usando la tecnica di sol-gel non idrolitico (NHSG) o la chimica di chelazione, la velocità di idrolisi/condensazione del precursore a base di allumina può essere ben controllata. Questo ci permette di rivestire catalizzatori con una grande area di superficie con allumina in maniera uniforme, avvicinandosi a quella che può essere osservata in processi come l'ALD. Nello specifico, il metodo di chelazione è stato utilizzato per la sintesi di un catalizzatore a base di $\text{Al}_2\text{O}_3@\text{Cu}/\text{Al}_2\text{O}_3$ resistente alla sinterizzazione. Le nanoparticelle ottenute sono rimaste ben disperse dopo cinque cicli di idrogenazione di furfurale in fase liquida.

A confronto, l'applicazione del processo NHSG ha lo scopo di creare più siti acidi di Lewis su atomi di platino all'interfaccia nel catalizzatore $\text{Al}_2\text{O}_3@\text{Pt}/\text{SBA-15}$. Questo catalizzatore è in grado di convertire 4-propilguaiacolo, derivato da lignina, in propilcicloesano tramite idrogenazione con una selettività del 87%. Il controllo cinetico può altresì essere esteso nel rivestimento di altri metalli di transizione. Specificatamente, nel terzo capitolo di questa tesi è descritta la deposizione di Nb_2O_5 su SBA-15, che ha come risultato un catalizzatore acido mesoporoso in fase solida. Questo catalizzatore ha una struttura amorfa più stabile dal

punto di vista termico, la quale gli consente di prevenire la perdita di acidità durante la sua rigenerazione a 500°C. Questo ossido di niobio acido sorpassa nelle prestazioni i catalizzatori commerciali a base di ossido di niobio sia per quanto riguarda la disidratazione di xilosio che per l'alchilazione di Friedel-Craft. Questo è dovuto al suo rapporto ottimale di siti acidi di Bronsted e Lewis, alla sua nanostruttura che è favorevole a questo tipo di reazioni.

Infine, nella mia tesi descrivo la sintesi di un materiale atomicamente disperso utilizzando metalli di coordinazione. In questo materiale l'interfaccia metallo-ossido di metallo può essere ulteriormente ingegnerizzata utilizzando tecniche di rivestimento sol-gel. Contrariamente alla deposizione di nanoparticelle su catalizzatori, rivestire il materiale con atomi di palladio ben dispersi prima del trattamento riduttivo può limitare la crescita delle particelle durante il passaggio di attivazione termica. Questo porta alla formazione di aggregati di palladio aventi un diametro inferiore ai 2 nm, i quali sono altamente accessibili e resistenti alla sinterizzazione.

È importante anche notare come ingegnerizzando l'interfaccia di Pd-ZrO₂ nell'interfaccia inversa ZrO₂-Pd utilizzando un rivestimento di ZrO₂ porta a una selettività del 100% nei confronti di CO durante l'idrogenazione di CO₂. I risultati di questa tesi mostrano che la tecnica di rivestimento sol-gel è una strategia promettente e rapida per progettare catalizzatori eterogenei che siano robusti e selettivi per un'ampia gamma di applicazioni nella chimica sostenibile.

Parole chiave: catalizzatore nanostrutturato, deposizione di ossidi di metalli, reazioni sol-gel, conversione di biomassa, idrogenazione di CO₂

Table of Contents

Acknowledgements.....	i
Abstract.....	ii
Résumé.....	iv
Astratto.....	vi
Table of Contents.....	viii
List of Figures in Main Text.....	xi
List of Tables in Main Text.....	xiii
Chapter 1 Introduction.....	1
1.1 Heterogeneous catalysts in the past and future.....	1
1.2 Gas and liquid phase overcoating methods.....	4
1.2.1 Atomic layer deposition.....	4
1.2.2 Sol-gel chemistry-based deposition in liquid phase.....	6
1.3 Heterogeneous catalysts designed by overcoating techniques.....	10
1.3.1 Synthesis of robust mesoporous metal oxide using overcoating.....	10
1.3.2 Nanoparticle stabilization using overcoating.....	13
1.3.3 Engineering catalyst surface functionalities and active sites.....	18
1.4 Motivation and objectives.....	22
1.4.1 Unlocking the limitations of sol-gel based deposition method.....	22
1.4.2 Synthesizing overcoated catalysts with improved stability.....	22

1.4.3 Tailoring interfacial sites for selective conversion of renewable substrates	23
1.4.4 Minimizing the loss of active sites caused by metal oxide deposition.....	23
Chapter 2 Development of Kinetically Controlled Sol-gel Coating Methods.....	24
2.1 Design of Al ₂ O ₃ precursors with slower hydrolysis/condensation kinetics.....	24
2.2 Al ₂ O ₃ deposition by chelation chemistry	27
2.3 Al ₂ O ₃ deposition by non-hydrolytic sol-gel chemistry	30
2.4 Improving the stability of Cu/Al ₂ O ₃ for furfural hydrogenation.....	33
2.5 Improving the selectivity for 4-propylguaiacol hydrodeoxygenation.....	35
2.6 The effects of physical and chemical properties of overcoats on HDO.....	38
2.7 Summary of Chapter 2	41
2.8 Experimental section of Chapter 2	42
Chapter 3 Synthesis of mesoporous Nb ₂ O ₅ by sol-gel coating.....	50
3.1 Sol-gel based overcoating of Nb ₂ O ₅ on silica substrate.....	50
3.2 Structural and acid properties of Nb ₂ O ₅ @SBA-15 and bulk niobia	53
3.3 Catalytic behavior of mesoporous Nb ₂ O ₅ and bulk catalysts.....	56
3.4 Summary of Chapter 3	65
3.5 Experimental section of Chapter 3	66
Chapter 4 Sol-gel Overcoating on Atomically Dispersed Pre-catalysts	70
4.1 Design of atomically dispersed pre-catalyst compatible with sol-gel coating.....	70
4.2 CO ₂ hydrogenation study	79
4.3 <i>In-situ</i> characterization and reaction mechanism.....	85

4.4 Summary of Chapter 4	90
4.5 Experimental section of Chapter 4	91
Conclusions and Outlook.....	96
List of Figures in Appendix	99
List of Tables in Appendix	100
Appendix.....	101
A.1 Supplementary information of Chapter 2.....	101
A.1.1 Supporting figure and table	101
A.1.2 Mass transfer effects on reaction.....	108
A.2 Supplementary information of Chapter 3.....	113
A.2.1 Supporting figure and table	113
A.2.2 Mass transfer effects on reaction.....	119
A.3 Supplementary information of Chapter 4.....	123
A.3.1 Supporting figure and table	123
A.3.2 Mass transfer effects on reaction.....	128
References.....	131
Curriculum Vitae	146

List of Figures in Main Text

Figure 1.1.1 (a) Comparison of traditional catalytic reactions and biomass conversion (b) Schematic illustration of overcoated catalysts and their featured properties.....	3
Figure 1.2.1 (a) Steps of the ALD deposition cycle using trimethyl aluminum as precursor A and water as precursor B. (b) Schematic illustration of an ALD apparatus.	6
Figure 1.2.2 (a) Growth mechanism during silica coating using sol-gel chemistry. (b) Comparison the barriers of homogeneous and heterogeneous nucleation.	8
Figure 1.3.1 Synthesis of mesoporous transition metal oxides using a hard-templating method with overcoating.....	12
Figure 1.3.2 (a) Illustration of the two main mechanisms of particle sintering of supported metal catalysts. (b) The effect of silica overcoat on the stability of Pt/SiO ₂	15
Figure 1.3.3 Strategies for minimizing the blockage of nanoparticles using protective ligands during metal oxide deposition.....	17
Figure 1.3.4 Schematic illustration of the selectivity control during cinnamaldehyde hydrogenation by using ALD.....	20
Figure 2.1.1 (a) NHSG and chelation chemistry of Al(^s BuO) ₃ for controlled Al ₂ O ₃ deposition. (b) Schematic illustration of the continuous injection syringe pump setup. (c) Van Der Waals structure and volumes of the two chemically modified Al(^s BuO) ₃	26
Figure 2.2.1 TEM and STEM images of C-Al ₂ O ₃ @SiO ₂	28
Figure 2.3.1 TEM and STEM images of N-Al ₂ O ₃ @SiO ₂	32
Figure 2.4.1 Results of continuous furfural hydrogenation	34
Figure 2.5.1 (a) Selectivities and conversions of 4-propylguaiaicol HDO over Pt based catalysts. (b) Reaction pathways of 4-propylguaiaicol HDO.	36
Figure 2.6.1 (a) ²⁷ Al solid-state NMR spectra of C-Al ₂ O ₃ @2%Pt/SBA-15, N-Al ₂ O ₃ @2%Pt/SBA-15 and 1%Pt/SBA-15 (b) Schematic illustration of the effect of overcoat texture on the hydrodeoxygenation of 4-propylguaiaicol.	40

Figure 3.1.1 TEM and STEM images of (a) $12\text{Nb}_2\text{O}_5@\text{SiO}_2$ with EDX mapping (inset), (b) $12\text{Nb}_2\text{O}_5@\text{SiO}_2$ with higher magnification, (c) $1\text{Nb}_2\text{O}_5@\text{SBA-15}$ under HAADF mode and (d) $1\text{Nb}_2\text{O}_5@\text{SBA-15}$ under HAADF mode with EDX mapping.	51
Figure 3.1.2 (a) Small-angle XRD results of uncoated and overcoated SBA-15. (b) Pore size distributions of uncoated and overcoated SBA-15.	53
Figure 3.2.1 (a) O 1s XPS results for SBA-15, overcoated SBA-15 and HY-340 (b) Nb 3d results for $4\text{Nb}_2\text{O}_5@\text{SBA-15}$, m- Nb_2O_5 and HY-340.	54
Figure 3.3.1 Xylose dehydration using different niobia catalysts. Points and bars represent conversion and furfural selectivity, respectively.	57
Figure 3.3.2 (a) Yield and distribution of products in the Friedel-Crafts alkylation catalyzed by different forms of niobia. (b) Catalyst stability test of $4\text{Nb}_2\text{O}_5@\text{SBA-15}$ and HY-340 after regenerations.	60
Figure 3.3.3 Kinetic study of Friedel-Crafts alkylation. Initial rate determination and TOF calculation for (a) $4\text{Nb}_2\text{O}_5@\text{SBA-15}$, (b) HY-340 and (c) m- Nb_2O_5 . (d) DRIFTS-Pyridine results.	62
Figure 3.3.4 ^1H ssNMR spectra and associated proposed schematic structure of HY-340 and $4\text{Nb}_2\text{O}_5@\text{SBA-15}$	64
Figure 4.1.1 Synthesis of ultra-small Pd clusters with ZrO_2 interface using sol-gel overcoating and coordination chemistry of ethylenediamine and Pd.	72
Figure 4.1.2 TEM images and Pd particle size distributions of (a) g-Pd/ SiO_2 and (b) $\text{Al}_2\text{O}_3@\text{Pd}/\text{SiO}_2$ and EDX mappings of (c) $\text{Al}_2\text{O}_3@\text{Pd}/\text{SiO}_2$ and (d) $\text{ZrO}_2@\text{Pd}/\text{SiO}_2$	75
Figure 4.1.3 XPS results of (a) g-Pd/ SiO_2 , (b) $\text{Al}_2\text{O}_3@\text{Pd}/\text{SiO}_2$ and (c) Pd/ Al_2O_3	78
Figure 4.2.1 CO_2 hydrogenation of (a) $\text{ZrO}_2@\text{Pd}/\text{SiO}_2$ (b) Pd/ ZrO_2 and (c) $\text{ZrO}_2@\text{Pd}/\text{ZrO}_2$. (d) CO chemisorption analyses of spent catalysts.	81
Figure 4.3.1 Operando DRIFTS results of (a) g-Pd/ SiO_2 (b) $\text{ZrO}_2@\text{Pd}/\text{SiO}_2$ (c) Pd/ ZrO_2 and (d) $\text{ZrO}_2@\text{Pd}/\text{ZrO}_2$	88
Figure 4.3.2 Proposed reaction networks of (a) Pd/ ZrO_2 , (b) $\text{ZrO}_2@\text{Pd}/\text{ZrO}_2$ and $\text{ZrO}_2@\text{Pd}/\text{SiO}_2$. The yellow and grey balls denote ZrO_2 and Pd, respectively.	90

List of Tables in Main Text

Table 2.5-1 Summary of the characterization data of Pt catalysts.....	38
Table 3.3-1 Characterization data of overcoated and bulk niobia catalysts	58
Table 4.1-1 Characterization results of overcoated and reference catalysts	76

Chapter 1 Introduction

This chapter is adapted from a published article in *CHIMIA International Journal for Chemistry* 73 (9), 698-706, 2019 by **Yuan-Peng Du** and Jeremy S. Luterbacher, with the consent of all the authors and the permission from the publisher.

1.1 Heterogeneous catalysts in the past and future

The chemical industry could not have developed to its current scope with only non-catalytic, stoichiometric reactions. Catalysts can accelerate chemical reactions by orders of magnitude, enabling industrially relevant reactions to be run under practical and economically viable conditions.¹ Heterogeneous catalysis plays a particularly vital role in the chemical industry, where up to 90% of bulk chemicals are produced from the processes with heterogeneous catalysts.² Unlike homogeneous catalysts, heterogeneous catalysts are formed by a solid material with catalytically active sites on the surface. Solid catalysts are easier to separate from product streams and can be further recycled, which is highly advantageous in chemical processes. The development of important uses of heterogeneous catalysis dates back to ammonia synthesis (1900s) and it has undergone rapid progression ever since. Many essential catalytic reactions and processes were discovered in the 20th century, including the catalytic cracking of crude oil (1930s), alkylation (1940s), and three-way catalysts for emission control (1970s).³ Along with these new processes, a plethora of heterogeneous catalysts have also been discovered and synthesized. The research in catalyst synthesis during this period has mainly focused on screening suitable supports and metals to enhance catalytic activities. Although many successes have been achieved, the development of heterogeneous catalysis is

facing a new challenge in 21st century. With the increasing demand for sustainably sourced carbon molecules to replace petroleum-based bulk chemicals, heterogeneous catalysis is increasingly being tasked to transform renewable carbon feedstocks into platform molecules. Biomass and CO₂ are two major renewable carbon sources on earth. CO₂ can notably be catalytically reduced to C₁ chemicals including CO, CH₄ and CH₃OH. Despite the simple chemical structure of CO₂, the reaction network of CO₂ reduction is complicated, which impedes the development of highly selective catalysts. Similar challenges also exist for catalytic biomass conversion but with different reasons. Due to the presence of multiple functional groups, various products can be produced from one type of biomass-derived molecule in a single catalytic step. In contrast, the substrates in traditional fossil-based processes are structurally simpler and typically less reactive, thus lowering the chemical complexity of their transformation (**Figure 1.1.1a**). Moreover, the impurities in biomass-derived feedstocks and the frequently required hydrothermal processing conditions imposed by the substrate's low volatility necessitate high robustness of heterogeneous catalysts. In this context, searching for new synthetic approaches to design catalysts that can fulfill these stringent requirements for sustainable applications has become a major priority in catalysis research.

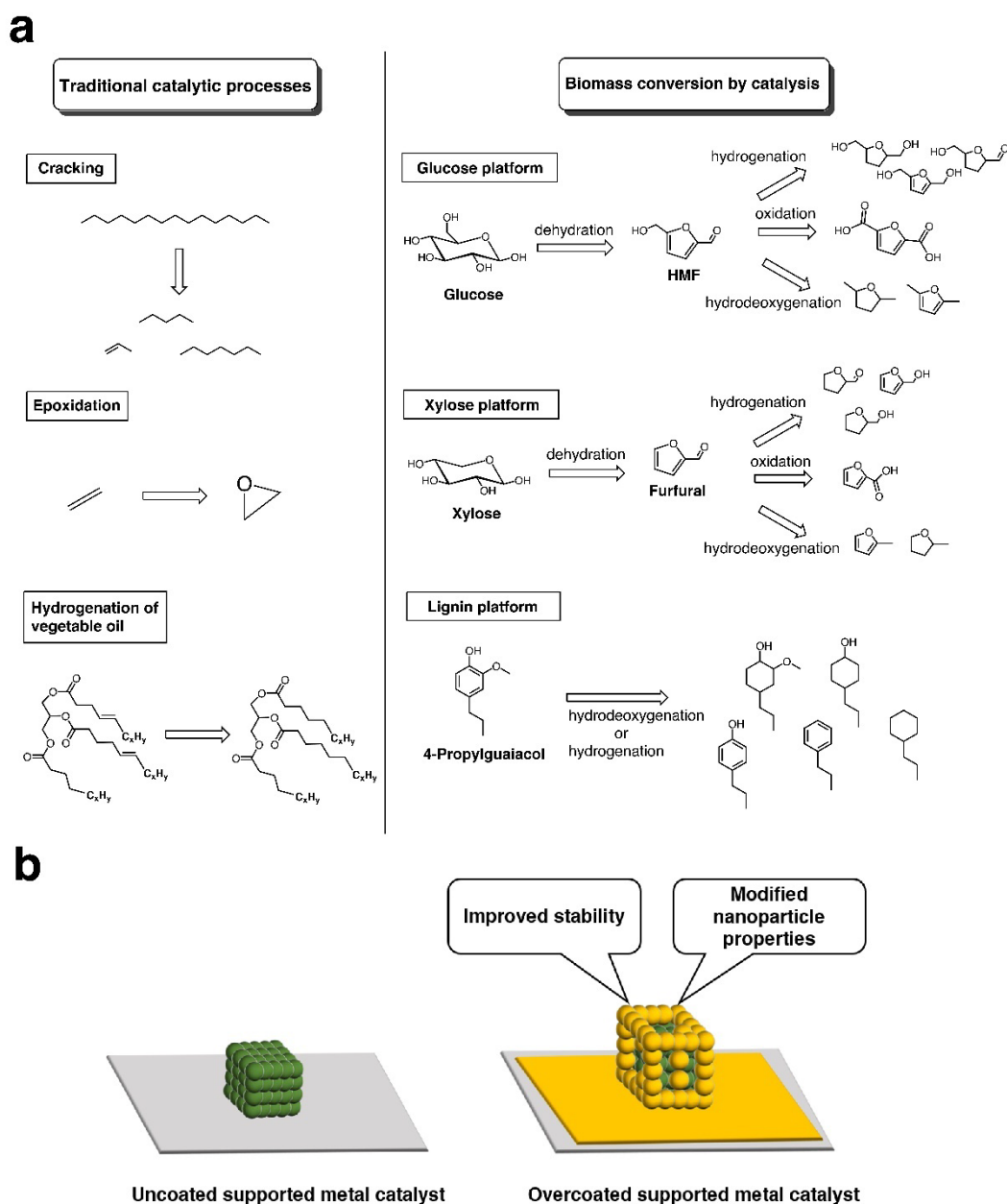


Figure 1.1.1 (a) Comparison of traditional catalytic reactions and catalytic biomass transformation, using three platform molecules derived from lignocellulosic biomass as an example. (b) Schematic illustration of overcoated catalysts and their featured properties.

In the last decade, the rapid development of nanoscale sciences had provided new synthetic techniques to tailor the structure of nanomaterials with controlled physical and chemical properties. Notable methods have featured the controlled deposition of thin oxide films with molecular precision using gas or liquid phase techniques.⁴⁻⁸ Leveraging these

techniques, a new class of heterogeneous catalysts, featuring a configuration with a layer of metal oxide deposited over supported metallic nanoparticles and a metal oxide support, has emerged. These methods have especially relied on the development of metal oxide deposition techniques that were extended beyond wafers to high surface area substrates. Specifically, these catalysts were “overcoated” by post metal oxide deposition, making them distinct from conventional supported metal catalysts (**Figure 1.1.1b**). Several interesting characteristics of overcoated catalysts were subsequently reported. One interesting application is imparting a greater sintering resistance or improved selectivities to certain heterogeneous catalysts because of the modification of nanoparticle’s environment. These new features could be beneficial for the renewable applications that are needed at present. In the following sections, several coating techniques for nanomaterials and their applications in catalyst design will be briefly reviewed.

1.2 Gas and liquid phase overcoating methods

Metal oxides are one of the most common materials used in catalysis. They can disperse metal nanoparticles and also frequently serve as catalytic species. In this section, two main categories of methods used for the deposition of metal oxides on heterogeneous catalysts will be introduced, namely atomic layer deposition and sol-gel chemistry.

1.2.1 Atomic layer deposition

Methods for depositing metal oxide overcoats on nanostructures can be categorized into two groups. The first method features processes based on chemical vapor deposition (CVD) where gaseous precursors react on a surface. Atomic layer deposition is the most frequently used technique within this family for the design of heterogeneous catalysts because its self-limiting reactions lead to a precise control over the thickness and the conformality of the overlayers.⁵ The simplest ALD process is a binary (AB) precursor system. In this process, the

first precursor (A) reacts with all the surface sites that are available on the substrates until the reaction is self-limited and a monolayer is formed. The remaining A is then pumped out of the reaction chamber with a purging gas. Subsequently, the second precursor B is fed to react with the monolayer of grafted A, also in a similar self-limited fashion, which completes one ALD cycle (**Figure 1.2.1a**). A common precursor A for metal oxide deposition is organometallic compounds with alkoxide or alkyl groups. Water is the most frequently used precursor B but other reagents can also be employed. For instance, NH_3 is used both as a precursor and catalyst for SiO_2 deposition because Si precursors such as silicon tetrachloride (SiCl_4) and tetraethoxysilane (TEOS) lead to low reaction rates within the temperature ranges that are achievable in most ALD apparatuses (30 °C to 250 °C).⁹ In contrast, trimethylaluminum (TMA) is hydrolyzed by water with a high reaction rate at room temperature, which makes TMA- H_2O a standard precursor pair for Al_2O_3 deposition.

The ALD instrument for coating powder and other high surface area substrates is similar to that used for coating planar and wafer substrates. The main difference lies in the design of the substrate chamber because the powder substrates usually entail longer deposition times and require additional features to improve particle dispersion and mass transfer. Because of the nature of high-surface-area substrates, mass transfer is usually significantly more limited compared to the case of wafers. A higher partial pressure of precursors can be used to accelerate mass transfer. However, nanoparticles can easily aggregate at the same time, which results in non-conformal coatings. In such case, mechanical dispersion of substrate particles becomes necessary. To address all of these issues, ALD can be performed on powder substrates in a fluidized bed reactor, where fluidization greatly increases dispersion and facilitates mass transfer of gaseous precursors that react with the fluidized particles (**Figure 1.2.1b**).⁴ The substrate beds can even be further agitated by vibration or using a mechanical stirrer to induce fluidization in order to further decrease aggregation and mass transfer limitations. A more in-

depth review of ALD reactor design is beyond the scope of this thesis but can be found elsewhere.¹⁰

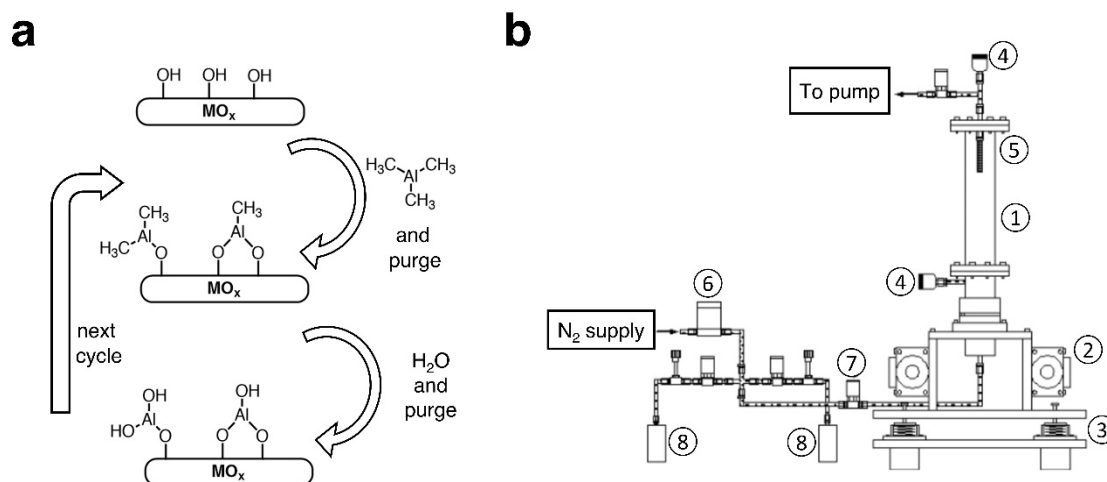


Figure 1.2.1 (a) Steps of the ALD deposition cycle using trimethyl aluminum as precursor A and water as precursor B. (b) Schematic illustration of an ALD apparatus which is composed of (1) a reaction column, (2) vibro-motors, (3) spring supports, (4) pressure transducers, (5) a sintered-metal filter, (6) a mass flow controller, (7) pneumatic valves and (8) precursor containers. Adapted with permission from ref 4. Copyright 2005, John Wiley and Sons.

1.2.2 Sol-gel chemistry-based deposition in liquid phase

In addition to ALD, metal oxide deposition on nanoparticles can also be performed in solution using sol-gel processes. Sol-gel is a chemical method to synthesize inorganic materials (e.g. metal oxides and ceramics) through the transformation of precursors from monomers to oligomeric “sols” and finally to a polymeric structure called “gel”.^{11,12} The most common sol-gel precursors for metal oxides are metal alkoxides. Sol-gel reactions, similar to ALD processes, are initiated by the hydrolysis of the precursor. However, the further hydrolysis and condensation of precursors do not typically proceed in a self-limiting manner. In solutions, partially condensed precursors first form colloidal sols, which further nucleate to form bigger nanoparticles by additional polycondensation and crosslinking.¹³ The Stöber method is a

typical example of well-defined SiO₂ nanoparticle synthesis using a sol-gel process.¹⁴ Typically, SiO₂ particles are prepared in an ethanol solution with ammonia being added to catalyze the hydrolysis and condensation of silica precursors. The resulting SiO₂ particles have a spherical shape and an extremely narrow particle size distribution could be achieved ($\pm 4\%$).¹⁵ The synthesis mechanism has two consecutive stages: nucleation–growth and then monomer addition, where the negatively charged siloxane clusters (seeds) first nucleated and then partially hydrolyzed silanol monomers fused into siloxane networks, which eventually resulted in spherical nanoparticles.^{16,17} Due to its simplicity and unique particle size control, this process has been extensively studied. Extension of the Stöber method showed that SiO₂ can grow on the surface of various particles (i.e. the core material) to form a so called “core-shell” structure (**Figure 1.2.2a**).¹⁸ This finding led to the rapid developments of sol-gel coatings and such techniques have sparked the research of new synthesis methods and applications for core-shell nanomaterials.

In contrast to ALD, sol-gel coating can be easily performed in any standard chemistry laboratory since specific ALD equipment is not required. Nevertheless, the deposition of other metal oxides other than SiO₂ usually needs further kinetic control because most metal oxides’ precursors hydrolyze and condense significantly faster than tetraethyl orthosilicate (TEOS, the most frequently used precursor for producing silica) does. According to classical nucleation theory, the nucleation barrier of homogeneous nucleation is higher than that of heterogeneous nucleation because homogeneous nucleation involves the formation of more interfaces between small nuclei and solvent molecules and thus leads to a significantly higher surface energy.¹⁹ In comparison, the surface energy of the seeds can be reduced when they nucleate on a substrate, which lowers the nucleation barrier of heterogeneous nucleation compared to homogeneous nucleation (**Figure 1.2.2b**). Consequently, heterogeneous nucleation, and thus overcoating, are favored when the precursors have slow condensation kinetics, which is indicative of a relatively

higher nucleation barrier. This phenomenon is observed in the case of the deposition method derived from Stöber process for tailoring core-shell structures. In contrast, faster precursor hydrolysis/condensation rates generally imply that the nucleation energy barrier is fairly low and thus homogeneous nucleation also occurs despite being less favored than heterogeneous growth. For instance, the high hydrolysis/condensation rates of aluminum sec-butoxide $[\text{Al}(\text{sBuO})_3]$ generally result in its rapid homogeneous nucleation and subsequent Al_2O_3 precipitation. Therefore, deposition of alumina using sol-gel chemistry is more difficult than using ALD since both homogeneous and heterogeneous nucleation can simultaneously occur and lead to non-uniform overcoats.

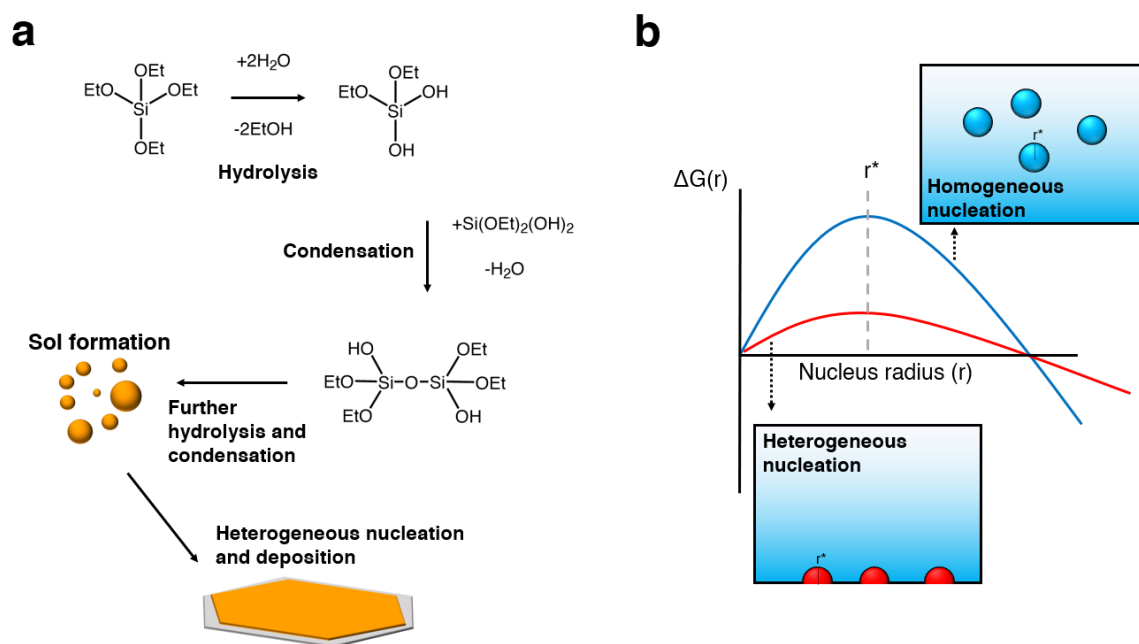


Figure 1.2.2 (a) Growth mechanism during silica coating using the sol-gel chemistry of TEOS as an example. According to both theoretical and experimental studies, metal alkoxide first forms nanoparticles (sols) by hydrolysis, which condense and then nucleate on the substrate.^{13,20} (b) Comparison of the energy barriers of homogeneous and heterogeneous nucleation. The r^* in the figure denotes critical nucleus radius. Nucleation becomes spontaneous when the nucleus exceeds this size.¹⁹

To ensure the preferential deposition of metal oxide on a substrate in sol-gel processes, there are two main strategies that have been reported in the literature. The first one is through the surface reaction between metal alkoxides and the hydroxyl groups on substrates in anhydrous conditions. After surface condensation, the unreacted precursor is removed and then the grafted metal alkoxide is hydrolyzed by water prior to the next grafting cycle.^{8,21,22} The disadvantage of this approach is that it uses excess amounts of solvents for rinsing and sometimes even involves full drying of the substrate. To improve this grafting method, our group previously developed a strategy where we injected a stoichiometrically limited quantity of precursor based on the estimated amount of precursor that could achieve a monolayer coverage on the substrate's surface by precursor volume projection.⁷ This stoichiometric control avoided the use of a purging solvent or any excess precursor. Similar to ALD process, the thickness of overcoat can be controlled by varying the repeating times of grafting cycle. Notably, after the coating process, the surface area of the substrate increased from 34 to 68 m²/g with 15 deposition cycles. In contrast, ALD deposition usually reduced the surface area.²³ Therefore, solution based method seems to form more porous overlayers compared to that deposited by ALD.

The second strategy is controlling the kinetics of metal alkoxides to avoid homogeneous nucleation, which can be done by performing the sol-gel reaction in the reaction media containing optimum amounts of ammonia and water.⁶ This method is less time-consuming and wastes less solvent compared to the repetitive surfacing grafting approach. However, it is so far only viable for overcoating titania. The deposition of other transition metal oxides still requires ALD or repetitive sol-gel grafting.

1.3 Heterogeneous catalysts designed by overcoating techniques

This section reviews three applications in catalyst design using metal oxide deposition. The overcoated catalysts usually display distinct structural and chemical features from their uncoated counterparts. They have begun to be increasingly used in renewable catalytic processes since several advantages resulting from these interesting features were observed in traditional catalysis applications.

1.3.1 Synthesis of robust mesoporous metal oxide using overcoating

Metal oxide deposition can be a powerful technique to synthesize metal oxide with high surface areas and controlled porous structures using template-assisted strategies. Ordered mesoporous silicas were first synthesized (MCM-41) using cetyltrimethylammonium bromide in the 1990s.²⁴ The potential of such materials as catalysts was quickly recognized because of their high surface area, ordered pore structure and thermal stability. Subsequently, the synthesis of mesoporous transition metal oxides has attracted more attention in catalysis field. The unique catalytic properties of these metal oxides (e.g. redox activities, photo activity and acidity) has led to many applications of mesoporous metal oxides in catalysis science. Typically, templates are used to tailor to mesoporous structures. In such methods, the templating materials can be either a soft (e.g. surfactants or polymers) or a hard (e.g. pre-synthesized mesoporous silica) template. During the synthesis, soft templates can be easily removed by thermal treatments whereas a hard template is usually used as a permanent substrate. Therefore, it is crucial to have a highly uniform overcoat to completely modify the surface functionality when a hard template is used. Although the experimental procedures of methods using soft templates are generally simpler than those using hard templates, the surface areas of mesoporous transition metal oxides prepared using soft templates are usually not as high as that of mesoporous silica.²⁵ To target a higher surface area, overcoating can be used in

a specific hard templating approach, where the metal oxide of interest is deposited on mesoporous silica using either ALD or liquid phase techniques (**Figure 1.3.1**).

TiO₂ is well-known for its photo activity and has many photocatalytic applications. Mahurin et al. first reported that titania could be deposited on SBA-15 using ALD with titanium tetrachloride and water as precursors and they determined that TiO₂ grew at the rate of 0.09 nm per ALD cycle.²⁶ Instead of titanium tetrachloride, other authors also explored the use of titanium isopropoxide (TTIP) for TiO₂ ALD.²⁷ High surface area TiO₂ was synthesized by depositing titania on different ordered mesoporous silica templates (MCM-41, SBA-15, and KCC-1) and their activities of photocatalytic dye degradation were tested. The ALD cycle conditions were found to have significant effects on the grain size of TiO₂, which governed the photoactivity of these overcoated materials. TiO₂ particles with a grain size at around 10 nm, which were prepared by performing 60 ALD cycles on KCC-1, showed the highest rate for degrading Rhodamine B dye.²⁷ Attempts to use sol-gel methods to deposit TiO₂ have also been made. As mentioned in section 1.2.2, the kinetics of metal alkoxide have to be controlled in order to avoid homogeneous nucleation. Perathoner et al. grafted TTIP in anhydrous conditions, which prevented any nucleation off the surface, leading to a uniform TiO₂ overlayer in the pore structure of SBA-15 after thermal treatment (the resulting material was denoted as TiO₂@SBA-15).²⁸ This TiO₂@SBA-15 had high surface area (above 500 m²/g) and an ordered hexagonal pore structure according to x-ray diffraction.

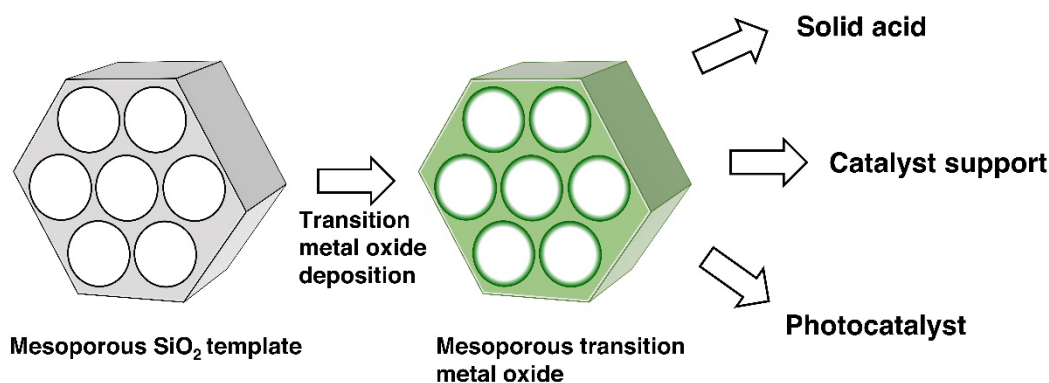


Figure 1.3.1 Synthesis of mesoporous transition metal oxides using a hard-templating method with overcoating.

The metal oxides with acidity are promising solid acids for catalyzing depolymerization and dehydration reactions, which are two important processes for valorizing lignocellulosic biomass. Specifically, Nb_2O_5 (niobia) shows interesting acid properties because it is one of the few metal oxides that possesses both Lewis and Brønsted acid sites. Pagán-Torres et al. reported the synthesis of mesoporous niobic acid using niobia ALD and SBA-15 as a template.²⁹ The overcoated SBA-15 showed not only an improved hydrothermal stability but also higher activities during the dehydration of secondary alcohols compared to a commercial bulk niobia catalyst. The improved hydrothermal stability and activities were attributed to the delayed phase transformation due to the formation of Si-O-Nb linkage and its higher surface area, respectively. Moreover, supporting Pd on this overcoated SBA-15 led to a bifunctional catalyst with high surface area and stability. The novel $\text{Pd/Nb}_2\text{O}_5@\text{SBA-15}$ can be used to convert biomass-derived γ -valerolactone into pentenoic acid for longer time-on-stream with less deactivation. This work exemplified the beneficial effects of the improved stability of overcoated catalyst for biomass conversion. Besides Nb_2O_5 , sulfonated ZrO_2 is another attractive solid acid catalyst for sugar dehydration. Osatiashtiani et al. synthesized a mesoporous zirconia by repeatedly grafting zirconium propoxide on SBA-15.²² Between each

cycle, the grafted SBA-15 was thoroughly washed with hexane to remove the unreacted precursor and re-hydrolyzed using water. The as-synthesized ZrO_2 was subsequently treated with sulfuric acid to produce sulfonated ZrO_2 . The authors suggested that the SBA-15 with 2 grafting cycles and subsequent treatment with 0.02 M H_2SO_4 had an optimal Brönsted/Lewis acid site ratio, thus leading to a three-fold increase in 5-HMF yield from glucose dehydration comparing to that obtained from bulk zirconia.

1.3.2 Nanoparticle stabilization using overcoating

Sintering of nanoparticles is a common deactivation pathway of supported metal catalysts. Sintering refers to the increase in nanoparticle size by particle migration and coalescence or/and Ostwald (atomic) ripening (**Figure 1.3.2a**).^{30,31} It causes irreversible loss of accessible metal sites because as nanoparticles grow, the ratio of surface atoms, which are the active sites to total atoms, irreversibly drops. Importantly, nanoparticle migration usually takes place at high temperatures, which are often used for catalyst regenerations. Therefore, even if the catalytic transformation occurs at low temperature, the regenerations may take place at higher temperatures, which could cause sintering and deactivation. Because the nanoparticles, especially those composed of noble metals, are often the costliest part of a catalyst, preventing nanoparticles from sintering and lowering their active surface area is of high interest to industry. Metal oxide deposition has recently emerged as a new strategy for designing sintering-resistant catalyst. The protective overcoats can either serve as a physical barrier³², anchor nanoparticles by strong metal-metal oxide interaction³³ or cap the undercoordinated atoms to prevent atomic ripening.²³

Depositing silica on supported metal catalysts to mitigate particle sintering using sol-gel technique was the earliest reported strategy because of its simpler experimental procedures. Lee et al. overcoated a Pt/SiO_2 catalyst with a 20 nm silica shell using a standard Stöber

procedure and the resulting catalyst remained well-dispersed even after being calcined at 802 °C (**Figure 1.3.2b**).³⁴ In another study, a monolayer of silica was grafted onto a Au/TiO₂ catalyst that was used for CO oxidation and this modified catalyst showed a similar improved stability and reduced sintering.³⁵ The recent advances in ALD technology and sol-gel synthesis techniques also enabled the design of catalysts with overcoats consisting of different transition metal oxides. Targeting other metal oxides besides silica for overcoating is worthwhile because silica is sometimes not hydrothermally stable and many renewable streams tend to contain water. Lu et al. synthesized a coking and sintering resistant Pd/Al₂O₃ catalyst by overcoating with Al₂O₃ ALD. The mean Pd particle size did not change after 28 h of time-on-stream, where the material catalyzed the oxidative dehydrogenation of ethane at 675 °C. In comparison, significant sintering was observed for the uncoated sample.³⁶ Using a similar strategy to improve catalyst stability for liquid phase biomass valorization applications was reported by O'Neill et al. where the authors synthesized an overcoated Al₂O₃@Cu/Al₂O₃ catalyst using ALD.²³ This work demonstrated that overcoats could be used to stabilize base metals during liquid phase furfural hydrogenation. The uncoated Cu/Al₂O₃ continuously and irreversibly deactivated as particle sintering took place during both the reaction and regeneration steps. In contrast, the overcoated catalyst showed the same activity after four regeneration cycles.

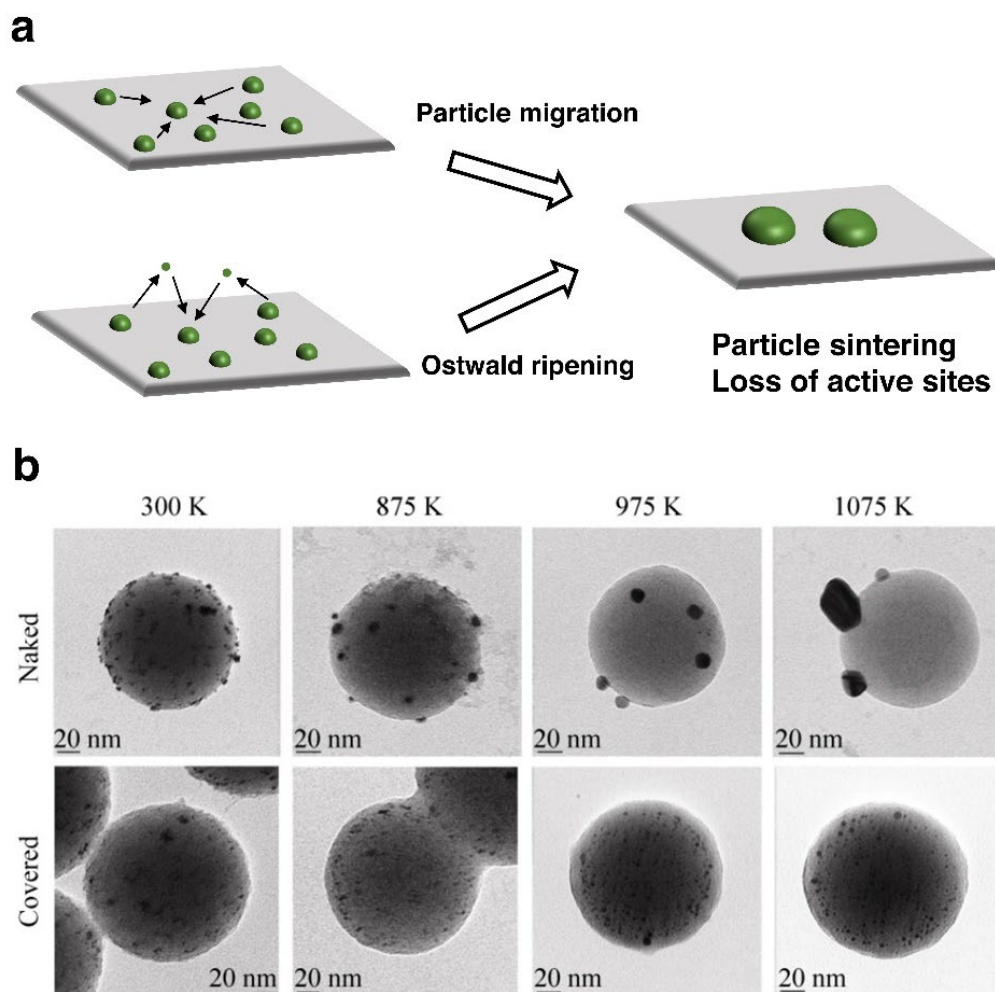


Figure 1.3.2 (a) Illustration of the two main mechanisms of particle sintering of supported metal catalysts. (b) The effect of silica overcoat on the stability of Pt/SiO₂. Sintering of Pt was observed when the uncoated catalyst was thermally treated above 602 °C whereas the overcoated Pt/SiO₂ still remained well-dispersed at 802 °C. Reprinted with permission from ref 34. Copyright 2011, Springer Nature.

Although the overcoat is a powerful tool for stabilizing nanoparticle, it may interact with the metal particles and can even completely deactivate the catalyst. Lee et al. observed that Co reacted with the alumina precursor during ALD to form an irreducible cobalt aluminate phase after calcination.³⁷ Consequently, the overcoated Co catalyst showed no hydrogenation activity. To avoid the formation of cobalt aluminate, the author overcoated the cobalt catalyst with TiO₂. Intriguingly, they found that the TiO₂ overcoat suppressed not only sintering but

also leaching during the hydrogenation of furfuryl alcohol in aqueous phase. This stability enhancement was ascribed to the capping of undercoordinated Co atoms. The capping of metal atoms can also lead to negative effects as the second common issue of metal oxide deposition, where the accessibility of nanoparticles may be limited when they are masked by the overcoat. Possible solutions include increasing the porosity by either thermal treatment or surface etching. Thermal treatment is the most common way to reactivate an overcoated catalyst and is usually necessary to get reasonable activities when using ALD. The increase in surface area of overcoated catalysts after calcination suggested that the overcoat was “cracked”, presumably by structural reorganization at high temperature, which led metal sites to be re-exposed.^{23,36,37} NaOH was also used to etch SiO₂ overcoats to increase the accessibility of active sites, which was shown with a SiO₂@Pt/SiO₂ catalyst used for the hydrogenation of 2-butenes.³⁸

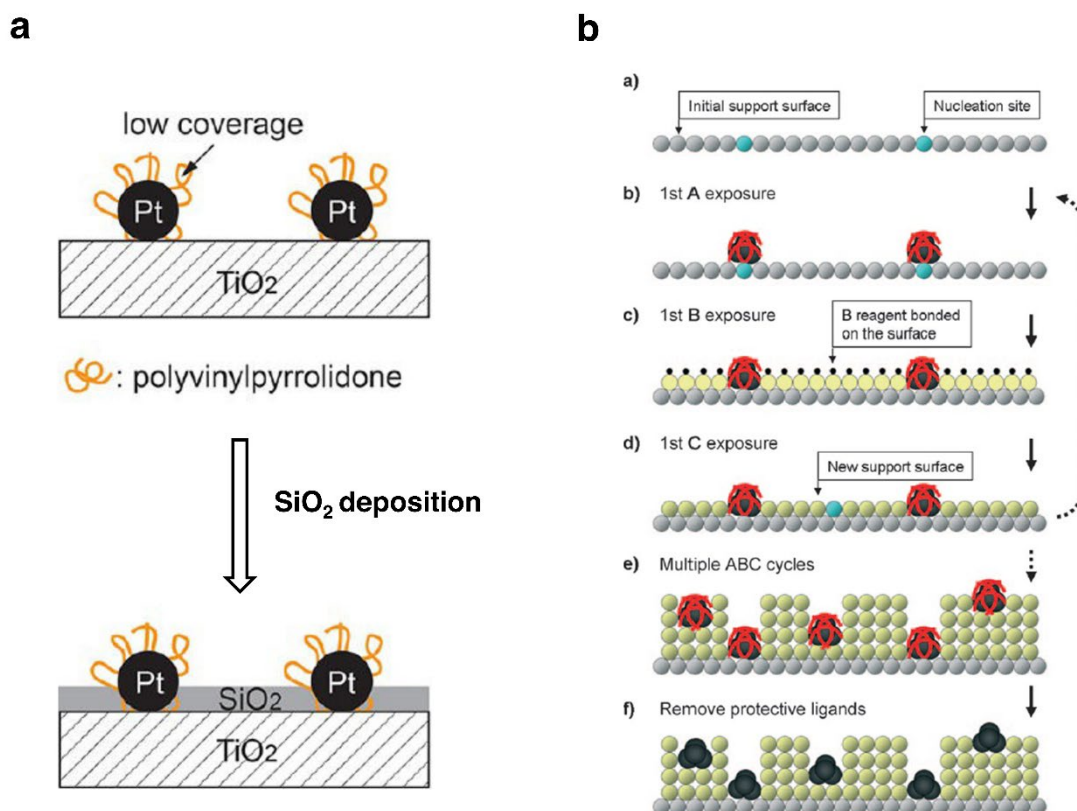


Figure 1.3.3 Strategies for minimizing the blockage of nanoparticles using protective ligands during metal oxide deposition (a) in a sol-gel process, using polyvinylpyrrolidone and (b) in an ALD process using an unhydrolyzable hexafluoroacetylacetonate ligand. Adapted with permission from ref 39, copyright 2013, American Chemical Society and ref 40, copyright 2010, John Wiley and Sons, respectively.

Protecting nanoparticles with organic ligands or polymers during coating procedures is another strategy to increase their accessibility. Lu et al. demonstrated that polyvinylpyrrolidone (PVP) can serve as a protective ligand when coating Pt/TiO₂ with SiO₂ using sol-gel chemistry.³⁹ This method relied on controlling the PVP density on the Pt surface, which played a pivotal role during the nucleation of the silica overcoat. Specifically, silica growth was inhibited when Pt particles had a relatively low PVP coverage, whereas high PVP coverage favored silica nucleation. This effect favored the growth of silica on the TiO₂ support, thus creating an “island” structure and leaving more nanoparticles accessible (**Figure 1.3.3a**). As a result, the catalyst

with a 2.8 nm silica overcoat still featured similar reaction rates to the uncoated sample when catalyzing the reduction of p-nitrophenol. Similar strategies have also been reported for ALD processes. A low-temperature ABC-type ALD technique was developed in 2010 to synthesize a highly dispersed $\text{TiO}_2@\text{Pd}/\text{TiO}_2$ catalyst.⁴⁰ Up to now we have discussed AB-type ALD (i.e. one precursor, A, and one counter-reactant, B), which is the most common method for coating heterogeneous catalysts. In this strategy, palladium (II) hexafluoroacetylacetonate, $[\text{Pd}(\text{hfac})_2]$, TTIP, and water were used as precursors A, B and C, respectively. The substrate was a pure TiO_2 support without nanoparticles and each cycle featured an extra step, where the Pd precursor was introduced and Pd nanoparticles formed from the nucleation of $\text{Pd}(\text{hfac})_2$ on the support. Pd complexes aggregate during this nucleation step, presumably through the ligand dissociation and formation of Pd—Pd bonds. Then, because the hfac ligand on Pd did not react with water below 200 °C, the overcoat could selectively grow on the support (with subsequent exposures of precursors B and C) without blocking the Pd particles (**Figure 1.3.3b**). Finally, the ligand could be removed using a mild thermal treatment (200 °C), which resulted in a catalyst with a very small mean particle size (~1 nm). CO chemisorption was used to quantify the Pd sites and the result was proportional to the number of Pd ALD cycles, indicating that the strategy led to a high Pd accessibility.

1.3.3 Engineering catalyst surface functionalities and active sites

The progress of more advanced characterization and computational tools have provided increasing theoretical and experimental insight into the active sites on catalyst surfaces.^{41,42} Notably, the interaction between metal nanoparticle and support has increasingly been recognized for its key role in catalysis.⁴³ Indeed, in some cases, the metal oxides do not merely serve as a carrier of metal nanoparticles but also contribute in catalysis. When this occurs, the catalytic properties of nanoparticles on different metal oxide supports can vary significantly. Recent findings also suggested that some reactions are actually only catalyzed by the metal-

support interfaces instead of the nanoparticles alone.^{44–46} In this context, metal oxide deposition has been proposed as a strategy to rationally design supported metal catalysts by either modulating the properties of nanoparticles or increasing the number of interfacial sites.^{44,47} One illustrative example of modifying the nanoparticle functionality is the use of $\text{ZrO}_2@\text{Pd}/\text{Al}_2\text{O}_3$ for methane oxidation. The as-synthesis catalyst with a 1 nm zirconia overcoat prepared using ALD showed a limited activity for methane oxidation. However, the overcoated catalyst could be reactivated after being heated to 800 °C (due to the cracking phenomenon described in the previous section) and showed a higher rate compared to fresh $\text{Pd}/\text{Al}_2\text{O}_3$ for methane conversion. The authors attributed the improved activity to the interaction between the ZrO_2 and nanoparticles. The overcoat could have stabilized PdO , which was hypothesized to be one of the active sites for methane oxidation.⁴⁸ In addition to altering the properties of nanoparticles, metal oxide overcoats can also physically engineer the microenvironment where the nanoparticles are located thereby directing the reaction towards a more favorable pathway. Yi et al. used ALD to synthesize an $\text{Al}_2\text{O}_3@\text{Pd}/\text{Al}_2\text{O}_3$ catalyst for the selective hydrogenation of 1,3-butadiene.⁴⁹ Unlike when using the uncoated Pd catalyst, where the selectivity towards butene significantly dropped at above 20% conversion, $\text{Al}_2\text{O}_3@\text{Pd}/\text{Al}_2\text{O}_3$ could still selectively produce butene at 100% conversion without over-hydrogenation. This significant selectivity improvement was attributed to the microporous structure of the alumina overcoat. The authors suggested that the adsorption of butene was limited by the physical structures around the Pd sites within the micropores of overcoat, which prevented butene from adsorbing and being further hydrogenated.

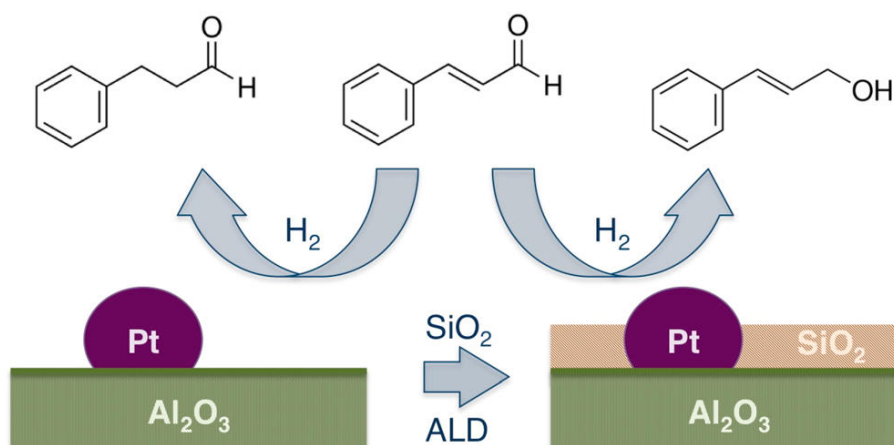


Figure 1.3.4 Schematic illustration of the selectivity control during cinnamaldehyde hydrogenation by using ALD to create interfacial Brønsted acid-metal sites. The Figure was adapted with the permission from ref 52, copyright 2018, American Chemical Society,

Overcoating is also a powerful approach to engineer the functionality of a catalyst surface. In particular, depositing a new metal oxide overcoat that is different from the pristine support can form a mixed oxide interface that possesses distinct chemical properties. Silica-alumina is a well-known mixed oxide material with unique acid properties and is used as a Brønsted acid catalyst in the petroleum industry. The Brønsted acidity has been attributed to the presence of aluminum atoms in the silica network, which stabilizes the conjugated base of deprotonated silanols.⁵⁰ Therefore, overcoating silica on an alumina surface or the reverse can form Brønsted acid sites at the interface between the overcoat and the support. Ardagh et al. overcoated silica on a commercial alumina with varying thickness using a standard Stöber method.⁵¹ They found that the thickness of the overcoat significantly affected the acid properties. Brønsted acid sites were observed after overcoating 2 nm of silica on the surface whereas the surface became inert when the overcoat was thicker than 5 nm. The optimized $\text{SiO}_2@\text{Al}_2\text{O}_3$ catalyst showed a similar activity for the dealkylation of 1,3,5 triisopropylbenzene to commercial $\text{SiO}_2\text{-Al}_2\text{O}_3$ and zeolites. Moreover, applying the same

strategy to a supported metal catalyst can create Brønsted acid sites that have a more intimate contact with nanoparticles. Such interfacial Brønsted acid-metal sites can modulate the selectivity during the hydrogenation of cinnamaldehyde, which was demonstrated in a recent work published by Weng et al (**Figure 1.3.4**).⁵² Similar to the aforementioned $\text{SiO}_2@\text{Al}_2\text{O}_3$ catalyst, Brønsted acid sites formed after overcoating SiO_2 on $\text{Pt}/\text{Al}_2\text{O}_3$ with 3 ALD cycles, which grew approximately a half a monolayer of silica. Importantly, the selectivity towards cinnamyl alcohol was considerably improved after overcoating. The catalyst with 4 ALD cycles showed the highest selectivity (85%) whereas the uncoated $\text{Pt}/\text{Al}_2\text{O}_3$ led to only 25% selectivity, which suggested that the synergy between Brønsted acid sites and Pt particles played an important role in the selective hydrogenation of unsaturated aldehyde.

1.4 Motivation and objectives

In light of the potential of metal oxide deposition for catalyst design, this thesis aims to explore and improve this strategy to synthesize more stable, active and selective heterogeneous catalyst for converting renewable carbon feedstocks, especially lignocellulosic biomass and CO₂, into platform molecules. This thesis will focus on addressing four challenges in this field, which are described below.

1.4.1 Unlocking the limitations of sol-gel based deposition method

In section 1.2, the advantages and disadvantages of sol-gel coating and ALD were discussed. Although sol-gel processes are simpler to perform and use less expensive equipment compared to ALD, the thickness control and the choice of metal oxide are still limited. Current solutions mostly include time consuming and prohibitively expensive methods that involve multiple grafting and washing cycles. The core challenge that has led to these issues is the fast kinetics of the sol-gel precursors of some metal oxides. Theoretically, when the precursors' kinetics are controlled, sol-gel deposition based on the Stöber method could be extended to other metal oxides beyond silica and titania. Accordingly, the first goal of this thesis is to develop a chemical method to achieve this kinetic control in order to establish a more generalized sol-gel technique for metal oxide deposition.

1.4.2 Synthesizing overcoated catalysts with improved stability

Previous studies have shown that overcoated catalysts are generally more resistant to sintering and/or hydrothermally stable. However, most of these materials were synthesized using ALD. After a more generalized sol-gel coating method is established, we can use this new method to synthesize more robust heterogeneous catalysts comprising metal oxide overcoats that previously could not be synthesized using traditional sol-gel chemistry. The

improved stability could increase the life time of overcoated catalysts in harsher reaction conditions, which are frequently required in renewable catalysis applications.

1.4.3 Tailoring interfacial sites for selective conversion of renewable substrates

The selectivity of heterogeneous catalyst is sometimes more important than activity in industrial processes because extensive product separation requires additional unit operations that can quickly increase costs. In particular, the multiple functional groups that exist in biomass-derived substrates can lead to the formation of many different products in a single stage (e.g. hydrogenation). Recent studies have shown that the nanostructure of heterogeneous catalysts can play a crucial role in product selectivity.⁴⁷ In particular, some reactions exclusively occur at metal-metal oxide interfaces.^{53,54} With a judicious choice of overcoat, specific metal-metal oxide interfaces could be designed to improve product selectivity during the valorization of CO₂ and biomass-derived platform molecules.

1.4.4 Minimizing the loss of active sites caused by metal oxide deposition

As previously discussed in 1.3.2, a fundamental issue for metal oxide deposition is that its benefits frequently occur at the cost of losing active sites during overcoating. This loss is mostly due to the covering of the active material by the overcoat. Up to now, only a few ligand-based strategies for minimizing the loss of active sites have been reported. Because they usually have to work in very specific conditions (e.g. using a special Pd precursor in an ALD process), the applicability in industry is significantly limited. The final objective of this thesis is to search for a new strategy to prevent nanoparticles from being blocked during catalyst coating. This complementary strategy would enable the synthesis of overcoated catalysts with maximal atom efficiency, which would improve their potential in industrial applications.

Chapter 2 Development of Kinetically Controlled Sol-gel Coating Methods

This chapter is adapted from a published article in *Small*, 14 (34), 1801733, 2018 by **Yuan-Peng Du**, Florent Héroguel and Jeremy S. Luterbacher, with the consent of all the authors and the permission from John Wiley & Sons.

2.1 Design of Al₂O₃ precursors with slower hydrolysis/condensation kinetics

The deposition of a metal oxide overcoat in liquid phase relies on controlled heterogenous nucleation during the sol-gel reaction. The current challenge of sol-gel coating is the precursors' high hydrolysis and condensation rates that lead to both homogeneous and heterogeneous nucleation. In fact, a high-surface-area substrate favors heterogenous nucleation because more nucleation sites are present in the reaction suspension. Therefore, we proposed that the controlled sol-gel coating of metal oxides besides SiO₂ and TiO₂ on high-surface-area materials could be made possible by slowing down the sol-gel kinetics. As a proof of concept, we tried to develop a method to overcoat alumina using Al(ⁿBuO)₃, which is a precursor with fast hydrolysis and condensation kinetics when water is present. Our first strategy for kinetic control is chemically modifying Al(ⁿBuO)₃ using non-hydrolytic sol-gel (NHSG) chemistry, which was first reported by Acosta et al.⁵⁵ Typically, the precursor of the NHSG reaction can be prepared by mixing metal halides and metal alkoxides. Ligand exchange occurs between the metal halide and metal alkoxide at room temperature while condensation only takes place at higher temperatures (above 100 °C). The gelation is likely initiated by the ligand exchanged precursors, which was shown in a previous study on TiCl₄-Ti(ⁱPrO)₄ NHSG chemistry.⁵⁶ The

actual precursors involved in those gelation processes have been identified as $\text{Ti}(\text{iPrO})_3\text{Cl}$ and $\text{Al}(\text{iPrO})_2\text{Cl}$ for $\text{Ti}(\text{iPrO})_4\text{-TiCl}_4$ and $\text{Al}(\text{iPrO})_3\text{-AlCl}_3$ pairs, respectively.⁵⁷ Mixing metal alkoxides and metal halides with non-optimal ratios has been shown to cause long gelation time.⁵⁶ Instead of AlCl_3 , AlBr_3 was used in our study because it enables the use of CH_2Br_2 as a solvent instead of the more toxic CCl_4 .⁵⁵ The ratio of $\text{Al}(\text{sBuO})_3$ and AlBr_3 here was kept to 2 by hypothesizing that $\text{Al}(\text{sBuO})_3\text{-AlBr}_3$ pair follows the same chemistry reported in the literature of analogous Ti and Al systems (**Figure 2.1.1a**).⁵⁷ The second strategy for kinetic control is adding ethyl acetoacetate (EAA) to chelate $\text{Al}(\text{sBuO})_3$ by ligand substitution.^{58–60} The sol-gel kinetics of the resulting chelated alumina precursor is dependent on the ratio between EAA and $\text{Al}(\text{sBuO})_3$. In this work, we prepared the precursor by reacting 0.75 equivalent EAA with $\text{Al}(\text{sBuO})_3$ (**Figure 2.1.1a**).

After preparing the chemically modified precursors, the substrates were either dispersed in a Stöber solution (for chelated precursor) or a heated anhydrous CH_2Br_2 (for NHSg precursors). Alumina deposition was systematically initiated by injecting the precursors into these respective suspensions and then the mixture was refluxed. A syringe pump (**Figure 2.1.1b**) was used to inject the precursors and avoid any undesirable homogeneous condensation due to a high precursor concentration within the catalyst suspension. In order to approximately estimate the amount of precursor needed to form a single atomic monolayer on the surface of the catalyst, we calculated the surface projection of the Van Der Waals volumes of the precursor molecules by MarvinSketch software (**Figure 2.1.1c**), which were estimated to be 0.48 nm^2 and 1.0 nm^2 for $\text{Al}(\text{sBuO})\text{Br}_2$ and $\text{Al}(\text{sBuO})_2(\text{EAA})$, respectively. Our past work with alumina has shown that steric hindrances between precursors is the determining factor for calculating maximum precursor coverage on the surface instead of the surface hydroxyl density.⁷ The necessary amount of precursor for achieving monolayer coverage on a specific material was then calculated by dividing the specific surface area of the catalyst by this

projected precursor area. Knowing the amount of precursor needed to form a monolayer allows us to achieve a targeted number of deposited monolayers by controlling the total amount of injected precursor, leading to a sub-nanometer control over the overcoat thickness.

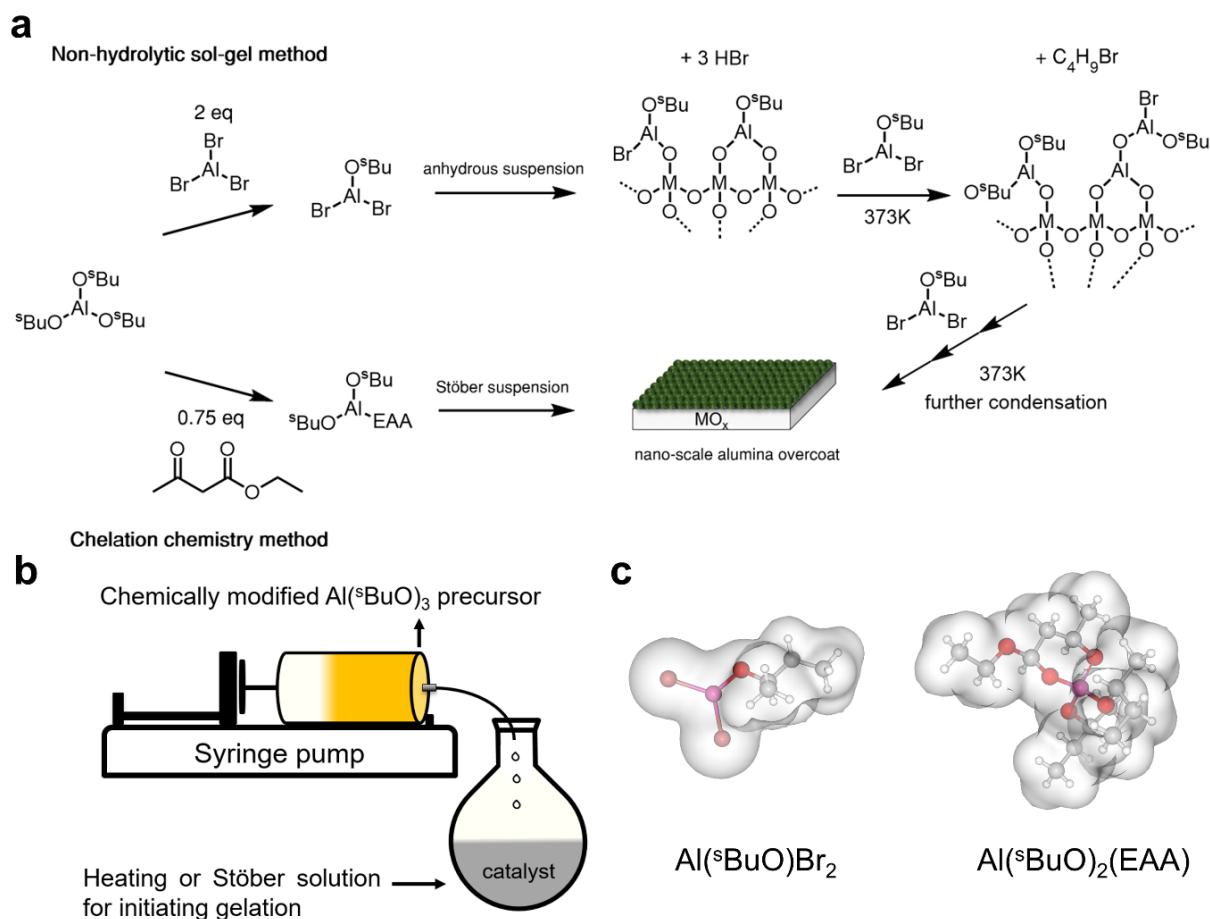


Figure 2.1.1 (a) NHSG and chelation chemistry of $\text{Al}(\text{sBuO})_3$ for controlled Al_2O_3 deposition. (b) Schematic illustration of the continuous injection syringe pump setup. (c) Van Der Waals structures and volumes of the two chemically modified $\text{Al}(\text{sBuO})_3$.

2.2 Al₂O₃ deposition by chelation chemistry

Al₂O₃ overcoating using the chelating method was first performed on SiO₂ spheres with relatively low specific surface area (as determined by the Brunauer-Emmett-Teller method as 15 m²/g, S_{BET}) in order to easily image the overcoat. This material is referred to as C-Al₂O₃@SiO₂, where C denotes materials prepared using the chelating method. Though high-angle annular dark field scanning transmission electron microscopy (HAADF STEM) provides low contrast between the SiO₂ core and the Al₂O₃ shell (**Figure 2.2.1a**), energy dispersive X-ray (EDX) spectroscopy mapping clearly showed that a conformal alumina overcoat was formed on the silica spheres (**Figure 2.2.1b**). We subsequently investigated Al₂O₃ deposition on a Pt catalyst supported on high-surface-area SBA-15, which was more representative of a material used for catalytic applications. The final injected amount of Al per unit weight of SBA-15 was 1.73 mmol/g_{catalyst}, which corresponds to approximately 3 monolayers of Al(^sBuO)₂(EAA). **Figure 2.2.1c** and **Figure 2.2.1d** show no modification of SBA-15 morphology after alumina deposition (for comparison, a TEM image of the uncoated material is available in **Figure A.1.1**). EDX mapping (**Figure 2.2.1e**) showed a uniform distribution of Si and Al, which implied that Al₂O₃ growth occurred within the pore structure. Formation of the Al₂O₃ layer inside the pores was also supported by the measurement of a reduced average pore size (from 6.8 to 6.3 nm) determined by nitrogen physisorption (**Figure A.1.2a**). Notably, the periodic structure of SBA-15 was fully preserved after overcoating as evidenced by powder x-ray diffraction (XRD) (**Figure A.1.2b**). In agreement with a previous work studying the surface alumina grafting of SBA-15, the S_{BET} of C-Al₂O₃@2%Pt/SBA-15 was drastically decreased, from 722.6 m²/g to 392.2 m²/g, which has been determined as being linked to the filling of micro-pores.⁶¹ Importantly, this method is not merely restricted to overcoating silica-based substrates. We successfully overcoated other metal oxides like Fe₂O₃ ellipsoid nanoparticles and even hydrophobic substrates such as carbon spheres (**Figure A.1.3**).

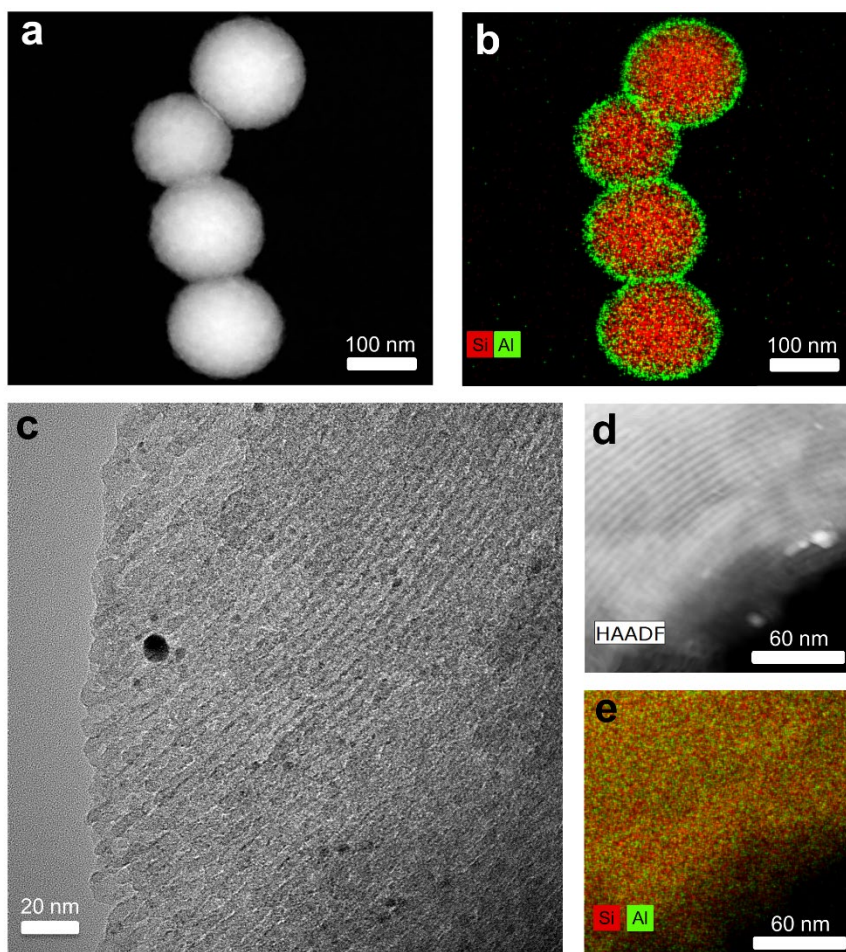


Figure 2.2.1 TEM and STEM images of C-Al₂O₃@SiO₂ (a) under HAADF mode and (b) with EXD mapping, or (c) C-Al₂O₃@2%Pt/SBA-15 (d) under HAADF mode and (e) with EDX mapping.

Previous attempts to overcoat Al₂O₃ on powder substrates by sol-gel based methods had been made by repeatedly grafting aluminum alkoxides with surface hydroxyl groups in anhydrous solutions.^{61–63} Nonetheless, the grafted oxide in these studies did not grow uniformly over the surfaces or within the pore structure. In contrast, the overcoat of C-Al₂O₃@SiO₂ and C-Al₂O₃@2%Pt/SBA-15 was comparable in appearance to the alumina overcoat produced by ALD.⁶⁴ Another disadvantage of those published methods was that they required time-consuming multi-step procedures to achieve thicker overcoats. However, our new approach can be performed in a single step with an automated injection. Furthermore, it still produced uniform overcoats when the amount of alumina loading was increased five times (14 monolayer

equivalents of precursor, sample was denoted as C-5Al₂O₃@SBA-15, **Figure A.1.1a**). In this case, the average pore size of C-5Al₂O₃@SBA-15 was reduced to 4.1 nm while narrow pore size distributions as well as the characteristic diffraction peak of SBA-15 were still observed (**Figure A.1.2**). According to the pore size distribution determined by physisorption, the thickness of the alumina overcoat in the pores (1.35 nm) was close to the predicted thickness based on the presumed thickness of 1 monolayer of alumina (1.25 nm for 14 monolayers, or 0.09 nm per monolayer estimated from the physisorption results of C-Al₂O₃@2%Pt/SBA-15).

Several important parameters govern our chelation method. First, the quantity of added H₂O is crucial for controlling the hydrolysis kinetics. The ratio of water and ethanol used in this work was much lower (0.04) than that of the Stöber solution used for preparing spherical silica (0.15) because we observed that Al(^sBuO)₂(EAA) still reacts with H₂O faster than tetraethoxysilane does. Nevertheless, an insufficient concentration of water hindered the gelation of precursor and so an appropriate balance was required. Second, the concentration of NH₃, which is used as a catalyst to initiate the hydrolysis and condensation of metal alkoxide, was decreased when overcoating high-surface-area supports with porous structures such as SBA-15. A high NH₃ concentration led to uncontrolled condensation on the external surface of SBA-15 particles before the precursor could diffuse into the pore structure. **Figure A.1.1b** shows overcoated SBA-15 prepared with an excess NH_{3(aq)} (0.04 mL instead of 0.02 mL). The formation of fibrous structure around the particles is indicative of alumina growth outside of the SBA-15 pellet. Third, higher EAA/Al(^sBuO)₃ ratios are known to decrease gelation times.⁶⁵ Therefore, NH₃ and/or H₂O concentration had to be adjusted to obtain suitable gelation times when a higher EAA/Al(^sBuO)₃ ratio was used, which shows how the interplay of EAA chelation, water, and ammonia can be used to control the sol-gel kinetics of Al(^sBuO)₃.

2.3 Al₂O₃ deposition by non-hydrolytic sol-gel chemistry

After depositing an amount of NHSG precursor corresponding to 40 monolayers of Al₂O₃ on SiO₂ spheres, the formation of a rough surface was observed by STEM (**Figure 2.3.1a**). EDX mapping revealed a conformal alumina overcoat with an average thickness 12±4 nm, which corresponded to a monolayer thickness of about 0.3 nm. The coating of 2%Pt/SBA-15 was also performed and 1.73 mmol/g_{catalyst} of Al was injected (corresponding to a coverage of 1.3 monolayer for Al(^sBuO)Br₂), which was the same molar amount as the aforementioned C-Al₂O₃@2%Pt/SBA-15 material (though corresponding to fewer monolayers due to the smaller volume projected surface of the NHSG precursor). Similar to the materials obtained using our chelating method, deposition with NHSG chemistry did not alter the SBA-15 morphology (**Figure 2.3.1c and d**) or the characteristic XRD peaks of SBA-15 (**Figure A.1.2b**). The uniform mixture of SiO₂ and Al₂O₃ observed by EDX (**Figure 2.3.1e**) again suggested that alumina was deposited inside the pores, which was further supported by the reduced average pore diameter from 6.8 to 6.6 nm (**Figure A.1.2a**). The reduction of pore diameter implied that the alumina thickness formed by 1 monolayer equivalent of Al(^sBuO)Br₂ was roughly 0.075 nm, which is comparable but slightly denser than what was obtained from C-Al₂O₃@2%Pt/SBA-15. Therefore, NHSG method might produce a denser overcoat. It is worth noticing that this monolayer thickness was at a similar order of magnitude albeit below that of N-Al₂O₃@SiO₂. This difference could either be due to the discrepancies between two distinct analytical methods (microscopy and physisorption) or the initial filling of micropores in SBA-15, which does not contribute to reduction of pore diameter in the mesoporous range.

Compared to the chelation method, the overall concentration of the precursor loaded in the syringe was particularly important for controlling the Al₂O₃ growth during NHSG-based overcoating. Since the condensation was initiated by the higher temperature in the reaction flask (100 °C, **Figure 2.1.1a**), we found that the hot vapor generated during reflux could cause

the undesired gelation of precursor droplets before they dripped into the substrate suspension. This early gelation did not occur when the total aluminum concentration in the syringe was set below 0.1 M. With this adjustment, we were able to avoid any uncontrolled growth of Al_2O_3 outside the pore structure of SBA-15 (**Figure A.1.4**). It is also worth mentioning that the thickness of Al_2O_3 overcoats on 2%Pt/SBA-15 produced with the NHSG method were thinner when the same molar amount of Al was injected. We speculated that less bulky NHSG precursor (**Figure 2.1.1c**) could have resulted in a denser monolayer. Accordingly, we investigated the physical properties of these overcoats by analyzing the overcoated silica spheres whose simpler morphology enabled greater measurement sensitivities. Because the overcoat on C- $\text{Al}_2\text{O}_3@\text{SiO}_2$ was thinner than that of N- $\text{Al}_2\text{O}_3@\text{SiO}_2$, silica spheres with thicker alumina overlayer was prepared (C9nm- $\text{Al}_2\text{O}_3@\text{SiO}_2$) for analysis. Physisorption results (**Figure A.1.5**) suggested that the pore volume of C9nm- $\text{Al}_2\text{O}_3@\text{SiO}_2$ was three times higher than that of N- $\text{Al}_2\text{O}_3@\text{SiO}_2$ (0.11 cm^3/g and 0.03 cm^3/g , respectively), which confirmed that two overcoating routes lead to distinct textural properties. We suggested that is not only due to the different steric hindrances of precursors but also the differences in sol-gel chemistry and deposition mechanisms. We hypothesized that the rapid initial grafting reaction between $\text{Al}(\text{sBuO})\text{Br}_2$ and surface hydroxyl groups could ensure consecutive monomer-based surface condensation, leading to a denser alumina network. On the other hand, $\text{Al}(\text{sBuO})_2(\text{EAA})$ may proceed through an oligomer deposition mechanism. Specifically, the precursors start polymerizing into sub-nanometer oligomers (sols) when injected into catalyst suspension. These sols gradually crosslink and heterogeneous nucleation may only happen when supersaturation is reached by progressive injection. Our previous coarse grain modeling studies also showed that the preferred mechanism of Al_2O_3 deposition in liquid phase using $\text{Al}(\text{sBuO})_3$ occurs via an oligomer deposition mechanism, where the alumina overcoat formed by the polymerization of alumina oligomers instead of single precursors.¹³ If the formation of alumina

by the chelation method did indeed proceed through this oligomer-deposition mechanism, this would likely lead to a much more porous framework.

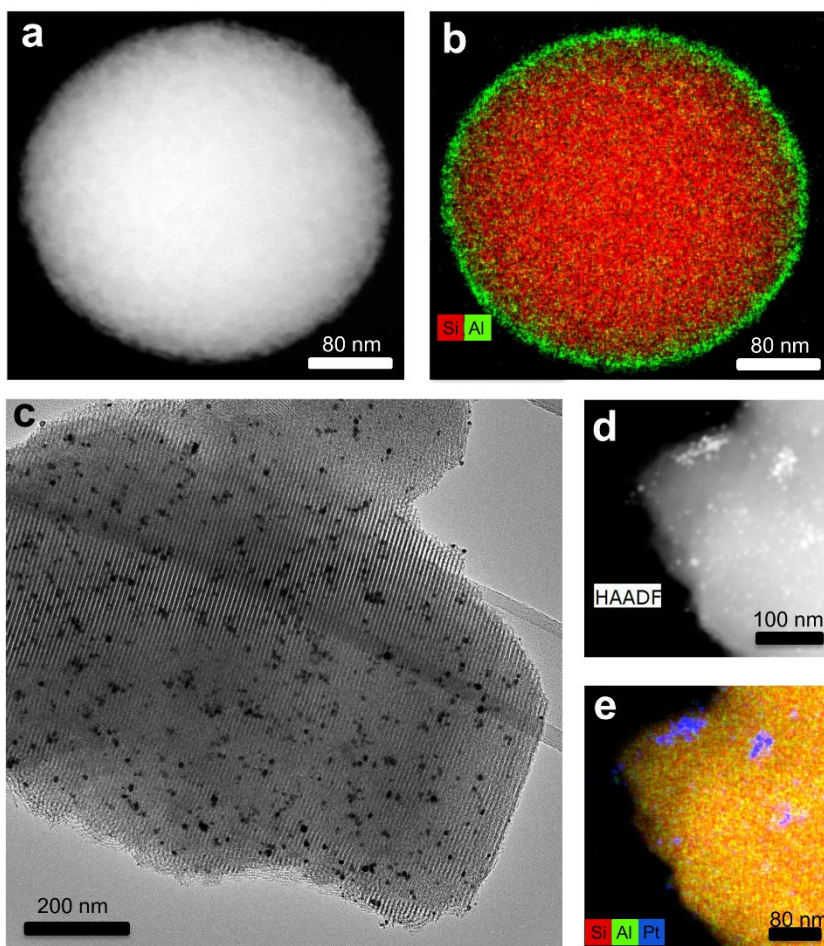


Figure 2.3.1 TEM and STEM images of N-Al₂O₃@SiO₂ (a) under HAADF mode and (b) with EXD mapping, or (c) N-Al₂O₃@2%Pt/SBA-15 (d) under HAADF mode and (e) with EDX mapping.

2.4 Improving the stability of Cu/Al₂O₃ for furfural hydrogenation

Deposition of a metal oxide overcoat onto a supported heterogeneous catalyst was known to stabilize the metal nanoparticles against sintering.^{23,31,33,36,37} However, stabilization is only successful if the overcoat is uniform and successfully covers all of the metal nanoparticles. Herein, we use furfural hydrogenation, which is a copper-based industrially relevant reaction for producing furfuryl alcohol (FFA), to investigate the stability of an overcoated copper catalyst and, indirectly, verify the uniformity of the overcoat. Our group previously developed a layer-by-layer alumina overcoating method achieved by alternately reacting substrate with stoichiometric amounts of Al(^sBuO)₃ and H₂O and applied it to the same reaction.⁷ Although that method can stabilize Cu/Al₂O₃ having surface area below 60 m²/g, it cannot form an equally good overcoat on Cu supported on high-surface-area Al₂O₃ since no discernible stabilization was observed (**Figure A.1.6**), which limits the applicability of our prior method to less industrially relevant supports. Our first attempts to deposit Al₂O₃ on high-surface-area Cu/Al₂O₃ using NHSG method leached all the copper out during the coating procedure, presumably due to the presence of the corrosive HBr byproduct. Therefore, we used the chelated Al(^sBuO)₃ precursor to overcoat Cu/Al₂O₃ (C-Al₂O₃@Cu/Al₂O₃) and demonstrate the benefit of having several available methods to control sol-gel kinetics. Although in initial tests, we had found that EAA interacted with metallic copper and again caused leaching (the color of reaction media turned blue after overcoating) during the coating process, this issue was easily resolved by oxidizing the copper with a mild thermal treatment before overcoating. With this pretreatment, the color change was not observed anymore. The S_{BET} of the resulting C-Al₂O₃@Cu/Al₂O₃ slightly decreased to 144 m²/g from 154 m²/g. The loading of Cu was determined by inductively coupled plasma optical emission spectroscopy (ICP-OES) and it was reduced from 5.0 wt% to 2.4 wt%, as a result of the additional weight of Al₂O₃ in the overcoat. Based on N₂O chemisorption, the original number of Cu surface sites on Cu/Al₂O₃ was 53.6

$\mu\text{mol/g}$ whereas no surface Cu sites were detected in the as-synthesized $\text{C-Al}_2\text{O}_3@\text{Cu}/\text{Al}_2\text{O}_3$. However, Cu sites could be re-exposed by calcination and $9.9 \mu\text{mol/g}$ of Cu surface sites were subsequently measured. This re-exposure of Cu could be attributed to either pore formation by the structural rearrangement of overcoat or the removal of residual precursor ligands strongly bound on the metal particles.^{23,35} If all the active sites were re-exposed, the number of Cu surface sites should be roughly $25.7 \mu\text{mol/g}$ because of the reduced Cu loading. Therefore, approximately 38% of active sites were recoverable after overcoating.

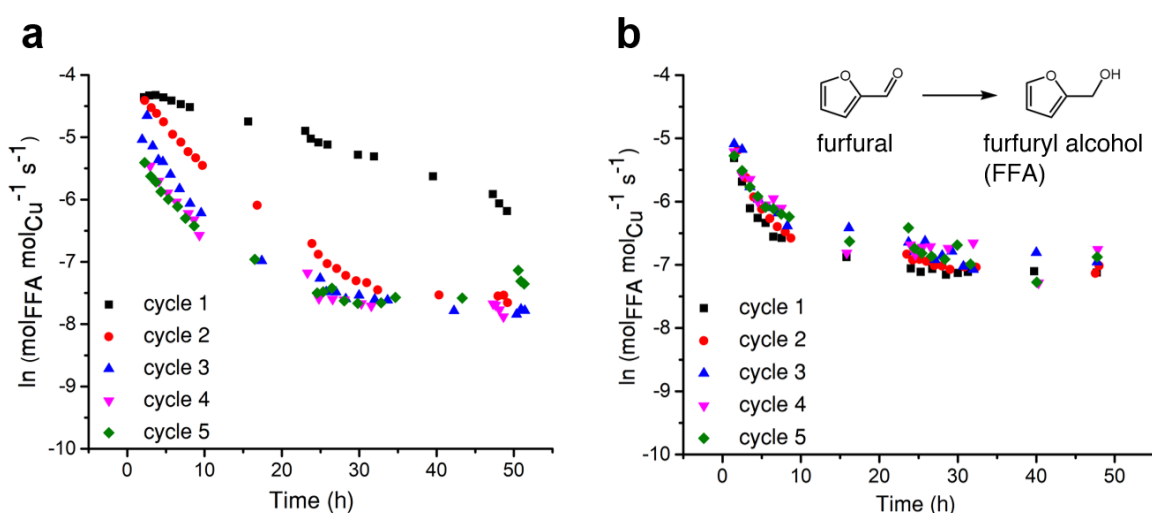


Figure 2.4.1 Results of continuous furfural hydrogenation over (a) $\text{Cu}/\text{Al}_2\text{O}_3$ and (b) $\text{C-Al}_2\text{O}_3@\text{Cu}/\text{Al}_2\text{O}_3$.

The stability of uncoated and overcoated catalysts were then tested using furfural hydrogenation as a probe reaction. In both cases, coke formation leads to rapid deactivation of the catalyst, which could be partially reversed. However, the sintering of Cu particles during calcination and the liquid phase reaction causes irreversible deactivation. The activity of $\text{Cu}/\text{Al}_2\text{O}_3$ was not fully recovered after calcination (**Figure 2.4.1a**), whereas the deactivation of $\text{C-Al}_2\text{O}_3@\text{Cu}/\text{Al}_2\text{O}_3$ could be completely reversed (**Figure 2.4.1b**). The spent catalysts were analyzed by TEM (**Figure A.1.7**) and pronounced particle sintering was observed on $\text{Cu}/\text{Al}_2\text{O}_3$.

In contrast, most of the Cu particles in C-Al₂O₃@Cu/Al₂O₃ were still well-dispersed after five catalytic cycles, which can be ascribed to protective effect from Al₂O₃ overcoat. O'Neill et al. had observed that tri-methylaluminum (ALD precursor) preferentially interacted with the step and defect sites of copper.²³ The sintering resistance likely resulted from the capping of these under-coordinated Cu atom. We suggest that aluminum sec-butoxide similarly decorated these labile Cu sites, thus reducing Cu mobility and inhibiting particle sintering. The furfural hydrogenation results indicated that the chelation chemistry-based approach can improve the stability of Cu supported on higher-surface-area support, which highlights the higher applicability of kinetically controlled strategy compared to previous grafting method. Accordingly, we consider chelation-based overcoating to be an easily performed but powerful method for overcoating a larger array of supported metal catalysts, including those containing less leaching-resistant base metals.

2.5 Improving the selectivity for 4-propylguaiacol hydrodeoxygenation

To test the potential of our overcoats for improving catalyst activity, we tested our materials for the hydrodeoxygenation (HDO) of lignin-derived propylguaiacol. Lignin is a plant fraction that is a polymer of phenylpropanoid subunits. Because of its aromatic-rich and energy dense structure, lignin is one of the most promising potential sources of chemicals and drop-in fuels that are derived from biomass.^{66,67} However, the lignin monomers that can be directly produced from lignin contain too much oxygen to be used directly as a fuel.⁶⁸ A typical example of such a molecule is propylguaiacol, which has been shown as the major and second most abundant product from the depolymerization of softwood and hardwood lignin, respectively.^{69–72} HDO of this molecule (and structurally similar ones) is a typical route for obtaining high quality fuels from lignin. In these reactions, the synergistic effects between

metal and acid sites play an important role and a variety of bi-functional catalysts for catalytic upgrading of oxygenated phenolic molecules have been reported.^{73–77} Although zeolites are an industrially relevant support that has abundant acid sites and high surface area, their hydrothermal stability is an issue for widespread use in biomass upgrading due to the amount of water that is generally present in such streams. Furthermore, their small pore size limits the diffusion of several molecules including lignin-derived oligomers and even some monomers.⁷⁵ Hence, creating acid sites on mesoporous SBA-15 supported metal catalysts would be an interesting application of Al₂O₃ overcoating method for synthesizing a stable bi-functional catalyst with a larger pore size for valorizing lignin-derived monomers.

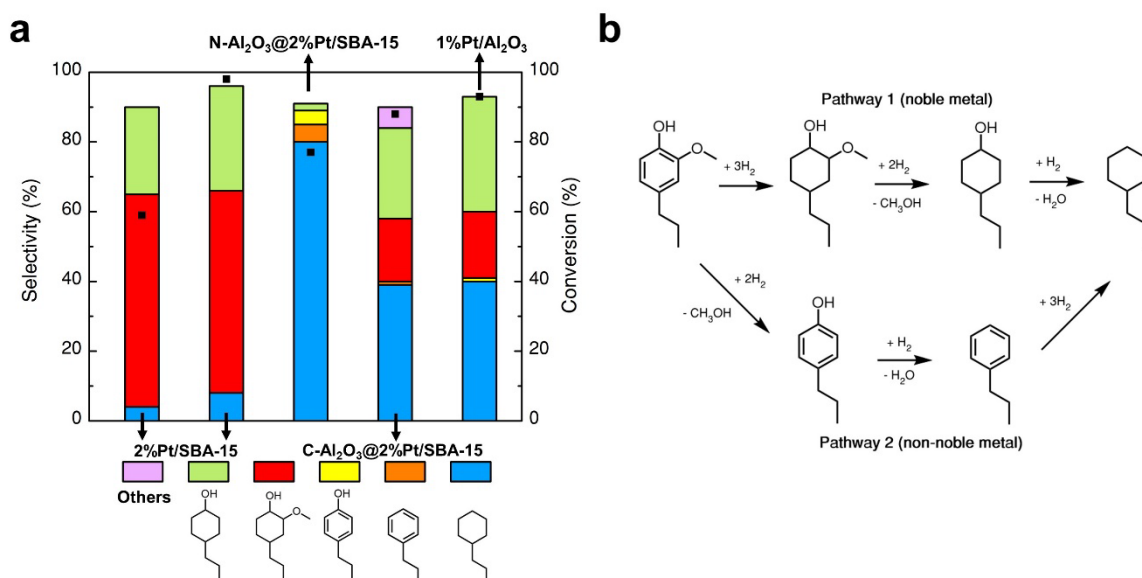


Figure 2.5.1 (a) Selectivities and conversions of 4-propylguaiacol HDO over Pt based catalysts. The reaction time was 3 h and the amounts of catalysts were all 20 mg except for 1%Pt/Al₂O₃ (40 mg, due to its metal loading being only half of 2%Pt/SBA-15). The first bar on the left represents the low conversion result for 2%Pt/SBA-15. The conditions for this data were a reaction time of 1.5 h and a 5-fold loading of 4-propylguaiacol. Products listed as *Others* included 1-propylcyclohexene and 4-propylcyclohexanone. (b) Reaction pathways of HDO of 4-propylguaiacol.

The HDO of 4-propylguaiacol was studied over a series of overcoated and uncoated Pt-based catalysts. Among all catalysts we synthesized, uncoated 2%Pt/SBA-15 had the highest rate in converting 4-propylguaiacol (**Figure 2.5.1a**), likely because of its greater number of accessible Pt sites (**Table 2.5-1**). Full conversion was reached after 3 h of reaction. Nevertheless, it had the lowest selectivity to fully deoxygenated products and the main product was 2-methoxy-4-propylcyclohexanol, which resulted from only ring hydrogenation. The selectivity of this product was 61% at the conversion of 59% and decreased with increasing conversion. However, increasing conversion yielded more 4-propylcyclohexanol and very small amount of fully deoxygenated C₉ alkane (propylcyclohexane), which indicated its limited HDO activity. Replacing the SBA-15 support with Al₂O₃ only slightly improved the selectivity to propylcyclohexane (approximately 40%) because the Lewis acidity of Al₂O₃ facilitated HDO. Interestingly, our two overcoated catalysts displayed very different selectivities. C-Al₂O₃@2%Pt/SBA-15 led to a similar propylcyclohexane selectivity to Pt/Al₂O₃ and other products like 1-propylcyclohexene and 4-propylcyclohexanone were also detected, suggesting that the overcoat prepared using the chelation method did not significantly improve deoxygenation selectivity. In contrast, N-Al₂O₃@2%Pt/SBA-15 showed an exceptional propylcyclohexane selectivity (80%). N-Al₂O₃@2%Pt/SBA-15 did display a slightly lower conversion (77%) at the same reaction time compared to C-Al₂O₃@2%Pt/SBA-15, which was attributed to its reduced number of accessible Pt sites as determined by CO chemisorption (**Table 2.5-1**). More interestingly, using N-Al₂O₃@2%Pt/SBA-15 led to a yield of about 10% aromatic products (4-propylphenol and propylbenzene). The selectivities toward these aromatic products were decreased when full conversion was reached, where the selectivity toward propylcyclohexane was close to 90% (**Figure A.1.8**). The production of aromatics suggests that the reaction proceeds through aromatic intermediates when N-Al₂O₃ overcoat is present. In comparison, selectivities to aromatic products were always less than 2.5% at the

same reaction time when the other three catalysts were used. As has been previously reported, when using noble metal based catalyst, the benzene ring of 4-propylguaiacol is rapidly hydrogenated as the first step and subsequent deoxygenation occurs (**Figure 2.5.1b**, pathway 1), which is in agreement to our observations.^{77,78} On the other hand, transition metal catalysts typically catalyze the hydrogenolysis of C-O bonds first and then the hydrogenation of aromatic ring. However, even when this occurs, this pathway is still much less favored than the alternate.⁷⁹ The majority of aromatic intermediates that were produced in the case of N-Al₂O₃@2%Pt/SBA-15 indicates that the C-O cleavage mechanism might be the primary one over this particular catalyst.

Table 2.5-1 Summary of the characterization data of Pt catalysts.

Catalyst	Al/Si ratio ^a	S _{BET} (m ² /g)	V _{micropore} (cm ³ /g) ^b	Lewis acid sites (μmol/m ²) ^c	Pt _{surface} (μmol/g)	d _{Pt} (nm) ^d
2%Pt/SBA-15	N/A	723	0.03	ca. 0	58.5	3.5±2.4
N-Al ₂ O ₃ @2%Pt/SBA-15	0.50	449	0	1.3	9.4	3.8±1.5
C-Al ₂ O ₃ @2%Pt/SBA-15	0.47	392	0.01	0.9	30.2	4.3±2.6
1%Pt/Al ₂ O ₃	N/A	164	0	1.5	35.2	5.0±1.9

^a) Determined by X-ray photoelectron spectroscopy (XPS), using the signals of Si 2s and Al 2s.

^b) Estimated using the t-plot method.

^c) Determined by NH₃ temperature programmed desorption and the value of S_{BET}.

^d) Determined by TEM analysis.

2.6 The effects of physical and chemical properties of overcoats on HDO

Pt particles and surface acid sites have previously been reported to have a synergistic effect during hydrodeoxygenation.^{75,77,80} The catalysts with the largest to the fewest numbers

of acid site per unit surface area were $1\%Pt/Al_2O_3 > N-Al_2O_3@2\%Pt/SBA-15 > C-Al_2O_3@2\%Pt/SBA-15$ (**Table 2.5-1**). However, the deoxygenation activity did not follow the same trend as $N-Al_2O_3@2\%Pt/SBA-15$ showed the highest selectivity towards fully deoxygenated alkanes compared to other catalysts. Powder XRD analyses confirmed the amorphous nature of alumina overcoats produced from both NHSG and chelation methods (**Figure A.1.9**). According to the decrease of the wavenumber of Si-OH band from 3745 cm^{-1} to 3739 cm^{-1} in the fourier-transform infrared (FTIR) spectra and the shifts as well as the broadenings of the proton signals in the 1H magic angle spinning solid-state nuclear magnetic resonance (MAS ssNMR) spectra (**Figure A.1.10 and A.1.11**), we concluded that nearly the whole surfaces of both $N-Al_2O_3@2\%Pt/SBA-15$ and $C-Al_2O_3@2\%Pt/SBA-15$ were covered by Al_2O_3 .⁸¹ Additionally, diffuse reflectance infrared fourier transform spectroscopy with pyridine probe (pyridine-DRIFTS) suggested that both overcoated catalysts had stronger Lewis acid sites compared to $1\%Pt/Al_2O_3$ (**Figure A.1.12**). Therefore, the different selectivities of $C-Al_2O_3@2\%Pt/SBA-15$ and $N-Al_2O_3@2\%Pt/SBA-15$ seem to be unrelated to the crystal structure of alumina, degree of overcoat coverage and the strength of acidity. We performed ^{27}Al MAS ssNMR to further elucidate the chemical compositions of two Al_2O_3 overcoats (**Figure 2.6.1a**). The octahedrally coordinated Al sites predominated in $1\%Pt/Al_2O_3$, which corresponds to the characteristic structure of $\gamma-Al_2O_3$. In contrast, both overcoated catalysts possessed a large proportion of under-coordinated Al(V) and Al(IV) sites, indicating their amorphous nature.^{23,55} Al(V) site is considered electron-deficient that leads to a strong Lewis acidity,⁸² which confirmed the pyridine-DRIFTS results. The alumina prepared from chelated precursor contained a higher proportion of Al(V) site. Such phenomena presumably resulted from the unreleased EAA ligand in the metal oxide framework. The Al center complexed by EAA could have converted into these Al(V) after removing the ligand by calcination. Although the ratio of Al(V) and Al(IV) may differ in the two overcoated catalysts, we assumed and

results confirmed that the alumina overcoats synthesized from $\text{Al}(\text{sBuO})_3\text{-AlBr}_3$ and $\text{Al}(\text{sBuO})_3\text{-EAA}$ were chemically similar.

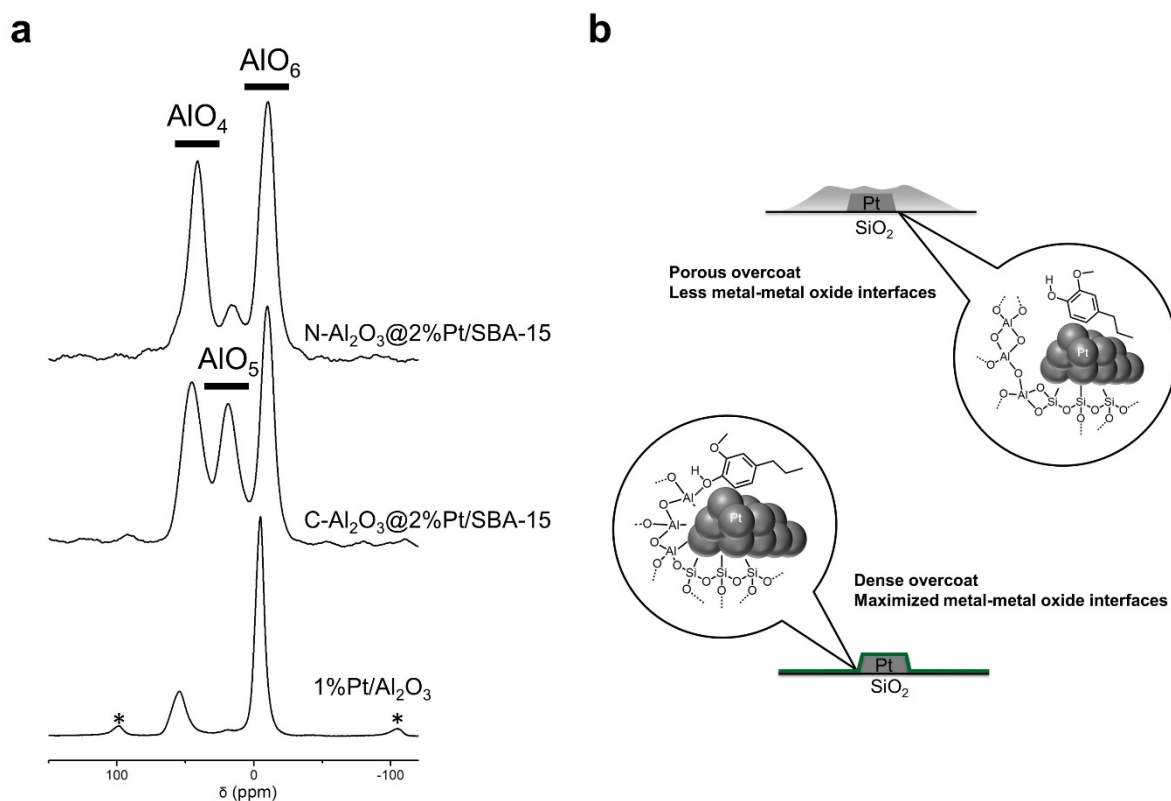


Figure 2.6.1 (a) ^{27}Al solid-state NMR spectra of $\text{C-Al}_2\text{O}_3@2\%\text{Pt/SBA-15}$, $\text{N-Al}_2\text{O}_3@2\%\text{Pt/SBA-15}$ and $1\%\text{Pt/SBA-15}$. Spinning sidebands were labeled by asterisks. (b) Schematic illustration of the effect of overcoat texture on the HDO of 4-propylguaiacol.

Many studies have suggested that the metal-support interface plays a crucial role in HDO.^{73,74} A recent investigation on phenol HDO revealed a mechanism showing that direct deoxygenation can proceed by the first interaction between the phenol tautomer and an surface oxophilic site, followed by the hydrogenation of the carbonyl group and a final dehydration step to form benzene.⁷⁸ The presence of electron-deficient Al(V) sites in the alumina overcoat and aromatic products suggests that 4-propylguaiacol was converted in a similar direct deoxygenation pathway over $\text{N-Al}_2\text{O}_3@2\%\text{Pt/SBA-15}$. Because Al(V) sites were present in

both overcoated Pt/SBA-15, we attributed the different selectivities to the distinct structural (rather than chemical) properties of two overcoats. As discussed in 2.3, the Al₂O₃ overcoat prepared from chelation chemistry method is more porous. Such physical differences of overlayers can also explain the fact that the accessible Pt sites of C-Al₂O₃@2%Pt/SBA-15 outnumbered those of N-Al₂O₃@2%Pt/SBA-15 by a factor of 3 after overcoating (**Table 2.5-1**) despite their similar metal loadings (as determined by ICP-OES: 1.7 and 1.9wt%). Compared to C-Al₂O₃@2%Pt/SBA-15, the denser overlayer on N-Al₂O₃@2%Pt/SBA-15 led to an increased intimate contact between Pt particles and Al₂O₃, which creates more interfacial metal-support active sites. In summary, with the overcoat displaying desired nanostructure, 4-propyluaiacol might mainly anchor on the abundant Pt-Al(V) sites of N-Al₂O₃@2%Pt/SBA-15, which promoted initial deoxygenation/hydrogenolysis and subsequent ring hydrogenation to form cyclohexane. In contrast, on the C-Al₂O₃@2%Pt/SBA-15, such interfacial site might be less abundant due to the higher porosity of the overcoat. Therefore, the reaction proceeded mostly through molecules bound directly to the metal (**Figure 2.6.1b**). In this case, the dominant reaction is known to be ring hydrogenation. These HDO results exemplify the critical effects that overcoat nanostructures can have on the selectivities of the reactions catalyzed by metal-metal oxide interface.

2.7 Summary of Chapter 2

We studied the formation of alumina overcoats over high-surface-area supported metal catalysts by slowing down the sol-gel kinetics of Al(^sBuO)₃ as a model precursor and developed two distinct approaches to achieve this kinetic control. In one case, we used non-hydrolytic sol-gel chemistry and in the other we used a chelation agent to manipulate the hydrolysis and condensation rates of Al(^sBuO)₃. Both methods were easy to conduct, yet highly versatile,

allowing us to deposit conformal alumina overcoats onto various high-surface-area substrates with sub-nanometer precision. Intriguingly, both methods offered distinct features that were advantageous in different cases. The non-hydrolytic route produced a denser Al_2O_3 overcoat and could remarkably improve the catalyst's selectivity during lignin hydrodeoxygenation—a reaction where the metal-metal oxide interface plays a crucial role. However, the non-hydrolytic sol-gel method could not be used with a supported base metal catalyst like Cu because it leads to metal leaching during the coating procedure. In this case, the milder chelation chemistry approach was the only route that could produce a uniform overcoat and protect the metal nanoparticles against sintering during liquid phase hydrogenation. These two chemical routes are considered as a less instrumentally demanding approach for alumina deposition compared to ALD processes. The control over overcoats' texture by varying the coating precursors also opens new possibility to synthesize heterogeneous catalysts with targeted nanostructures.

2.8 Experimental section of Chapter 2

Chemical and materials

All chemicals were analytical grade and obtained from commercial suppliers. They were used without further purification unless stated otherwise. Air and moisture-sensitive reagents were handled using a nitrogen filled glove box and a standard Schlenk line apparatus. Tetraethyl orthosilicate (TEOS), tetramethyl orthosilicate (TMOS), AlBr_3 , CaH_2 , $\text{H}_2\text{PtCl}_6 \cdot 6\text{H}_2\text{O}$, furfural and 1-butanol were obtained from Acros. Benzophenone, magnesium, sodium, Pluronic 123 (P123), 4-propylguaiacol, 2,2,4-trimethylpentane (isooctane), CH_2Br_2 , ethyl acetoacetate (EAA), 2-butanol and $\text{HNO}_{3(\text{aq})}$ (ca. 68%) were purchased from Sigma Aldrich. Molecular sieve (4Å), $\text{Al}(\text{sBuO})_3$, and $\text{HCl}_{(\text{aq})}$ (ca. 37%) were obtained from Merck.

Ethanol and diethyl ether were obtained from Fisher Scientific. Silicon carbide (100 mesh) was obtained from Strem. $\text{Cu}(\text{NO}_3)_2 \cdot 3\text{H}_2\text{O}$ was obtained from ABCR. $\text{NH}_3(\text{aq})$ (ca. 25%) was purchased from VWR Chemicals. $\gamma\text{-Al}_2\text{O}_3$ (Pural SB) was obtained from Sasol. Diethyl ether was dried over Na-benzophenone, distilled and stored over molecular sieves. 2-butanol was dried over Mg, distilled, stored over molecular sieves. CH_2Br_2 was dried over CaH_2 , distilled and stored over molecular sieves. Furfural and EAA were purified by distillation under reduced pressure. The water used in this study was purified by a Millipore Milli-Q Advantage A10 water purification system until its resistivity was higher than $18 \text{ M}\Omega \cdot \text{cm}$. All gases were purchased from Carbagas.

Preparation of supports and catalysts

The silica spheres were synthesized by Stöber method.¹⁴ Typically, 3.8 mL of TEOS, 7.7 mL NH_3 (ca. 25%) and 18 mL of deionized water were mixed with 120 mL ethanol. The mixture was stirred and reacted at room temperature (RT) for 24 h. The product was centrifuged and washed three times first with ethanol then water. SBA-15 was synthesized based on a previously published method that was slightly modified.⁸³ Briefly, 2.8 g of Pluronic P-123 was dissolved in 104 g of 1.6 M $\text{HCl}(\text{aq})$ by vigorous stirring. Then, 4 mL of TMOS was slowly added and the resulting mixture was stirred for 24 h. The suspension was transferred into a Teflon lined stainless steel autoclave and heated at 110°C for 24 h. After the hydrothermal treatment, the remaining surfactant was removed using a standard Soxhlet apparatus for 24 h using ethanol as the solvent. All synthesized supports were calcined at 500°C for 5 h under flow of synthetic air (ramping rate: $2^\circ\text{C}/\text{min}$) and dried under reduced pressure (below 10^{-2} bar) at 120°C prior to impregnation.

$\text{Cu}/\text{Al}_2\text{O}_3$ (5%) was prepared by incipient wetness impregnation using $\text{Cu}(\text{NO}_3)_2 \cdot 3\text{H}_2\text{O}$ dissolved in 0.1 M $\text{HNO}_3(\text{aq})$ as a precursor and calcined $\gamma\text{-Al}_2\text{O}_3$ support. The impregnated

powder was subsequently dried in an oven at 105 °C overnight and reduced at 300 °C for 5 h by flowing H₂ (ramping rate: 1 °C/min). 2%Pt/SBA-15 was prepared by incipient wetness impregnation using H₂PtCl₆·6H₂O dissolved in 1 M HCl_(aq) as a precursor. Both impregnated samples were dried overnight at 105 °C, calcined at 500 °C for 3 h and then reduced at 300 °C for 3 h.

Catalyst overcoating using non-hydrolytic sol-gel chemistry

All catalysts (0.5 g) were dried overnight under reduced pressure prior to overcoating. The NHSG precursor was prepared by dissolving AlBr₃ and Al(^sBuO)₃ in 20 mL CH₂Br₂. The precursor solution was loaded into a glass syringe (Hamilton US) with a PTFE plunger. The syringe needle was positioned into the reaction flask containing catalyst suspension refluxing at 100 °C and an automatic syringe pump (KDS 100 legacy syringe pump) was used to control the injection rate. SiO₂ spheres were dispersed in 10 mL CH₂Br₂ and then overcoated by injecting a precursor solution comprising 0.08 mL Al(^sBuO)₃ and 0.17 g AlBr₃. The injection rate was adjusted to 0.5 mL/h, which corresponds to one monolayer equivalent of precursor per hour. The solution was left to react for 24 h after the injection was completed. 2%Pt/SBA-15 was coated by injecting a precursor solution containing 0.14 mL Al(^sBuO)₃ and 0.3 g AlBr₃ at a rate of 1 mL/h. The solution was left to react for 6 h after the injection was completed. In both cases the following two subsequent post-synthesis treatments followed: first, 20 mL of diethyl ether were added into the suspension to quench the residual reactive Al–Br groups. The solution was then kept stirring at 80 °C overnight. The crude products were centrifuged and sequentially washed twice with diethyl ether, ethanol and water. After washing, the coated samples were stirred in 0.1 M NH_{3(aq)} at 60 °C overnight to further remove the remaining bromide. The ammonia treated products were washed with water and dried in a vacuum oven at 60 °C. The dried powder was calcined at 500 °C in order to completely remove any impurities and byproducts. Finally, the overcoated 2%Pt/SBA-15 were reduced at 300 °C for

3 h prior to the catalytic reactions. The resulting materials are referred to as N- $\text{Al}_2\text{O}_3@2\%\text{Pt/SBA-15}$ and N- $\text{Al}_2\text{O}_3@\text{SiO}_2$ in the main text.

Catalyst overcoating using chelation chemistry

C- $\text{Al}_2\text{O}_3@\text{SiO}_2$ was prepared by dispersing SiO_2 spheres (0.2 g) in a mixture containing 25 mL ethanol, 0.04 mL of 25 wt% $\text{NH}_{3(\text{aq})}$ and 1 mL H_2O . The precursor solution was prepared by stirring 0.6 mL $\text{Al}(\text{sBuO})_3$ and 0.22 mL EAA in 9 mL of 2-butanol for 1 h. This precursor solution was then injected into the mixture containing silica spheres using the aforementioned syringe setup at a rate of 1 mL/h. The suspension was heated to 40 °C and stirred for 6 h after the injection was completed.

C- $\text{Al}_2\text{O}_3@\text{Cu/Al}_2\text{O}_3$ was prepared by dispersing 0.5 g of $\text{CuO/Al}_2\text{O}_3$ (prepared by pre-oxidizing $\text{Cu/Al}_2\text{O}_3$ at 250 °C for 2 h using a flow of synthetic air) in the same solution as described above. The precursor solution was prepared by stirring 2 mL $\text{Al}(\text{sBuO})_3$ and 0.8 mL EAA in 27.2 mL 2-butanol for 1 h. This precursor solution was then injected into the $\text{CuO/Al}_2\text{O}_3$ suspension at a rate of 1 mL/h. The mixture was heated at 40 °C and stirred for 6 h after the injection was completed.

C- $\text{Al}_2\text{O}_3@2\%\text{Pt/SBA-15}$ was prepared by dispersing the uncoated catalyst (0.5 g of 2%Pt/SBA-15) in a mixture containing 25 mL ethanol, 0.02 mL 25 wt% NH_3 and 1 mL H_2O . The precursor solution was prepared by stirring 0.44 mL $\text{Al}(\text{sBuO})_3$ and 0.165 mL EAA in 9.4 mL 2-butanol for 1 h. The precursor was then injected into the 2%Pt/SBA-15 suspension at a rate of 1 mL/h. The mixture was left to react at RT and stirred for 8 h after the injection was completed. All the overcoated samples were washed three times with ethanol followed by water and then dried in a vacuum oven at 60 °C. C- $\text{Al}_2\text{O}_3@\text{Cu/Al}_2\text{O}_3$ and C- $\text{Al}_2\text{O}_3@2\%\text{Pt/SBA-15}$ were calcined at 400 °C and 500 °C, respectively for 3 h and then reduced at 300 °C for 5 h.

Supplementary overcoating samples using chelation chemistry

C-Al₂O₃@C was prepared by coating alumina on carbon sphere. To produce carbon spheres, 3.5 g glucose were dissolved in 3.5 mL of water in a Teflon-lined stainless-steel autoclave. The autoclave was heated at 180 °C for 3 h. After cooling down, the product was washed with water and dried in a vacuum oven. The resulting carbon spheres (0.1 g) were then overcoated by repeating the same steps as described for C-Al₂O₃@SiO₂. The synthesis of C-Al₂O₃@Fe₂O₃ was shown as followed: 0.02 M FeCl_{3(aq)} was mixed with 0.45mM KH₂PO_{4(aq)} in a Teflon-lined stainless-steel autoclave and heated to 105 °C for 48 h. After cooling down, the product was washed with water and dried in a vacuum oven. The resulting α -Fe₂O₃ ellipsoids (0.1 g) were then dispersed in a mixture of 25 mL ethanol, 1 mL H₂O and 0.04 mL 25 wt% NH_{3(aq)}. The precursor was prepared by mixing 0.5 mL Al(^sBuO)₃ as well as 0.2 mL EAA in 19.3 mL dry 2-butanol and then injected into the Fe₂O₃ suspension at a rate of 1 mL/h. The overcoated SBA-15 with thicker overcoat was synthesized using the same procedure described in the last section with an increased amount of the injected precursor solution. The precursor was prepared by stirring 2.2 mL Al(^sBuO)₃ and 0.82 mL EAA in 17 mL 2-butanol for 1 h.

Catalytic activity tests

Hydrodeoxygenation of lignin model monomer was performed by mixing catalyst with 10.5 mL isooctane and 0.1 mL 4-propylguaiacol in a 25 mL stainless-steel reactor (Parr). The reactions were run under 15 bar H₂ at 200 °C. The reaction time and the amounts of reactants were varied to reach different conversions. The temperature was ramped up with a heating plate and heating tape controlled by an Omega PID controller. The product was analyzed by an Agilent Technologies 7890 A gas chromatography apparatus equipped with a flame ionization

detector (GC-FID) and a HP-5 column (50 m, 0.32 mm). The internal diffusion limitation was negligible based on Weisz-Prater criterion (Section A.1.2).

Furfural hydrogenation was performed using a stainless steel fixed-bed down flow tubular reactor with an inner diameter 4.5 mm, which we previously described.⁷ The catalytic bed was prepared by mixing the catalysts with SiC and immobilized in the stainless steel tube between two quartz wool plugs. The remaining space of tube was filled with SiC and both ends were plugged with quartz wool. The heated zone corresponding to the area containing the catalytic bed was delimited by two external conductive stainless-steel blocks enclosed in a furnace. Before the first run, the catalyst was reduced under H₂ flow (100 mL/min) for 5 h at 300 °C. After cooling down to the reaction temperature (130 °C), hydrogen flow was adjusted to 35 mL/min using a Brooks mass flow controller and pressure was set to 23 bars using a back-pressure regulator (Tescom). A furfural solution (70 g/kg in 1-butanol) was fed into the reactor using SSI Series II HPLC pump at a rate of 0.10 mL/min. Liquid samples were collected using a Jerguson gage connected to a needle valve and then analyzed by GC-FID. Periodically, furfural flow was stopped and the catalyst was regenerated by calcination at 400 °C for 1 h, (under a flow of synthetic air at 100 mL/min) and subsequent reduction at 300 °C for 5 h (under a flow of H₂ at 100 mL/min). Catalytic activities were evaluated by the yield of furfuryl alcohol per unit time and mol of total Cu determined by ICP. The internal diffusion limitation was assumed to be negligible based on Weisz-Prater criterion (see section A.1.2).

Material characterizations

Physisorption and static Pt chemisorption analyses were performed on a Micromeritics 3 Flex instrument. The samples were dried under reduced pressure at 150 °C prior to N₂ adsorption. The surface area and pore size distribution were determined using Brunauer–Emmett–Teller (BET) theory and the Barrett–Joyner–Halenda (BJH) model, respectively.

The quantities of $\text{Pt}_{\text{surface}}$ were measured using CO as a probe molecule. The sample was dried *in situ* under vacuum and reduced at 300 °C for 1 h. The double isotherm method was performed, where the catalyst surface was first saturated by physisorbed and chemisorbed CO and then second adsorption was conducted after removing the physisorbed CO by reduced pressure. The amount of chemisorbed CO was calculated by the subtraction method using two adsorption isotherms. The stoichiometric ratio between Pt and CO was assumed to be 1.⁸⁴ Quantifications of $\text{Cu}_{\text{surface}}$ were performed on a Micromeritics Autochem II 2920 using N_2O as a probe molecule.⁸⁵ The samples were calcined *in situ* at 400 °C for 1 h and then reduced at 300 °C for 3 h. Subsequently, 0.5 mL $\text{N}_2\text{O}/\text{He}$ (1/99 vol./vol.) pulses were injected into the sample cell using a sampling loop carried by a flow of helium at 90 °C. The N_2 evolution and N_2O consumption were quantified by monitoring masses 28 and 44 using an MKS Cirrus 2 mass spectrometer.

NH_3 -TPD experiments were conducted on a Micromeritics Autochem 2920 instrument. The sample was dried under He Flow (50 mL/min) at 500 °C for 1 hours. After cooling to 120 °C, NH_3 (g) was flowed to saturate the sample. The sample then was ramped to 500 °C (10 °C/min) while the desorption of ammonia was recorded by a thermal conductivity detector and a calibrated mass spectrometer.

Pyridine DRIFTS was performed on a PerkinElmer Frontier IR instrument. The surface water was removed *in situ* by heating the samples to 250 °C under reduced pressure for 3 h. After cooling down to 50 °C, a He stream was bubbled into a cold pyridine (~50 mL/min) and the He-pyridine mixture was flowed into the cell to saturate the sample. The DRIFTS spectra were then recorded at different temperatures under a continuous flow of pure He (~50 mL/min).

Small angle XRD measurements were performed in a PANalytical Empyrean system (Theta-Theta, 240 mm) equipped with parallel beam mirror optics with Cu K- α as a radiation source.

TEM images were obtained on a FEI Talos instrument with a 200kV acceleration voltage. The samples were loaded on Lacey carbon grids. High-angle annular dark field scanning transmission electron microscopy (HAADF-STEM) was then performed in a mode resulting in atomic number contrast (Z contrast). Energy-Dispersive X-ray spectroscopy (EDX) was performed in HAADF-STEM mode and analyzed using Bruker Esprit software.

^{27}Al solid-state NMR spectra were recorded on a 900 MHz Bruker Avance spectrometer equipped with a conventional double resonance CP-MAS probe. Samples were packed in 3.2 mm zirconia rotors and spun at 24 kHz. A spin echo sequence with 0.5 s of D1 and 2 μs of P1 was used during measurements. ^1H spectra were recorded using Hahn-Echo sequence with 2 s recycle delay. The spectrum of adamantane was used as a reference for determining the chemical shifts.

X-Ray Photoelectron Spectroscopy measurements were carried out using a PHI VersaProbe II scanning XPS microprobe (Physical Instruments AG, Germany). Analysis was performed using a monochromatic Al K α X-ray source of 24.8 W power with a beam size of 100 μm . The spherical capacitor analyzer was set at a 45° take-off angle with respect to the sample surface. The pass energy was 46.95 eV yielding a full width at half maximum of 0.91 eV for the Ag 3d 5/2 peak.

Chapter 3 Synthesis of mesoporous Nb₂O₅ by sol-gel coating

This chapter is adapted from a published article in *Journal of Materials Chemistry A*, 7, 23803-23811, 2019 by **Yuan-Peng Du**, Florent Héroguel, Xuan Trung Nguyen and Jeremy S. Luterbacher, with the consent of all the authors and the permission from The Royal Society of Chemistry.

3.1 Sol-gel based overcoating of Nb₂O₅ on silica substrate

In Chapter 2, we presented two strategies to slow the condensation kinetics of sol-gel precursors and enable high quality coating. In this chapter the chelation method was extended to other transition metal oxide system. Specifically, Nb₂O₅ was chosen because of its powerful acid properties that can be used in numerous reactions including those involved in biomass conversion. Starting from the a model silica sphere substrate, an amount of chelated Nb(OEt)₅ that was sufficient to produce 12 monolayers of the niobia overcoat was prepared and injected into the a Stöber mixture containing SiO₂ and controlled amount of ammonia and water. A uniform Nb₂O₅ shell with a thickness of ~2 nm was formed on the sphere (**Figure 3.1.1a and b**). The S_{BET} of SiO₂ slightly increased after coating (from 12 to 15 m²/g), implying that the Nb₂O₅ shell has certain porosity. The image with higher magnification (**Figure 3.1.1b**) shows that some nano-sized Nb₂O₅ clusters sporadically formed on the silica surface. The porous overcoat structure was similar to the alumina overcoat described in the last chapter, which supported that the formation of metal oxide overcoats via chelation chemistry route proceed with an oligomer-deposition mechanism.¹³ Such a mechanism could result in some porosity

when niobia nanoparticles with different sizes aggregate and cover the surface. The larger niobia clusters might evolve from the larger sol particles.

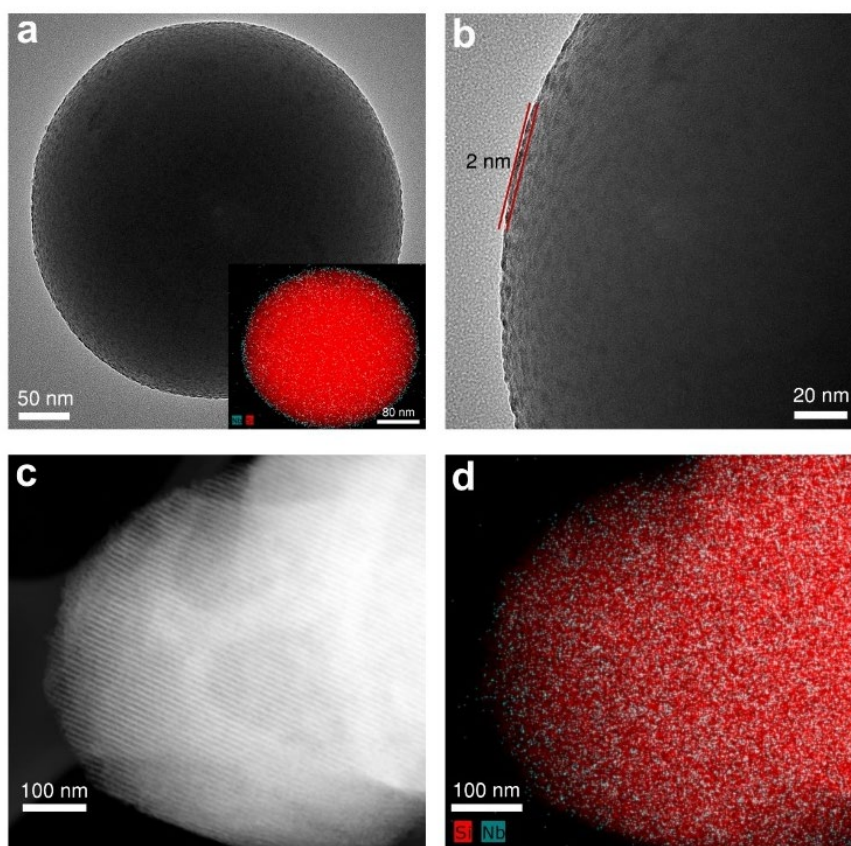


Figure 3.1.1 TEM and STEM images of (a) $12\text{Nb}_2\text{O}_5@\text{SiO}_2$ with EDX mapping (inset), (b) $12\text{Nb}_2\text{O}_5@\text{SiO}_2$ with higher magnification, (c) $1\text{Nb}_2\text{O}_5@\text{SBA-15}$ under HAADF mode and (d) $1\text{Nb}_2\text{O}_5@\text{SBA-15}$ under HAADF mode with EDX mapping.

We further tried to overcoat SBA-15 as a post-modification strategy to synthesize mesoporous niobia with high surface area and an ordered pore structure. Due to the slower condensation kinetics of the chelated $\text{Nb}(\text{OEt})_5$, a niobia overcoat could uniformly grow inside the mesopores of SBA-15, as confirmed by STEM microscopy and EDX mapping (**Figure 3.1.1c and d**). The morphology of SBA-15 did not significantly change with the increasing number of deposited Nb_2O_5 layers (**Figure A.2.1 to A.2.3**). Small-angle XRD was then used to characterize the porous structures of overcoated SBA-15. Pristine SBA-15 displays three

typical diffraction peaks that are the characteristics of $P6mm$ hexagonal symmetry. The intensity of the diffraction peaks was reduced after overcoating but still fully present after 1 layer (**Figure 3.1.2a**). The largest diffraction peak was maintained regardless of the number of layers, indicating that a periodic pore structure was conserved. The disappearance of the smaller diffraction peaks with increasing layers could be attributed to the scattering of X-ray by the overcoat rather than pore degradation,⁸⁶ which was further supported by physisorption (**Figure 3.1.2b**) using the Barrett—Joyner—Halenda (BJH) model. The overcoated samples still had a narrow pore size distributions and the pore volumes consistently decreased with increasing niobia loading. More importantly, the mean pore diameter reduced linearly with the number of Nb_2O_5 layers, implying a precise thickness control could be achieved (approximately 0.8 nm per layer, inset in **Figure 3.1.2b**). Overcoating Nb_2O_5 onto SBA-15 was previously reported by either using ALD or sequential sol-gel grafting.^{29,87} Comparing to these reported methods, The approach presented here has the advantages over both the ALD and grafting method. Sol-gel based coating procedure can be more easily performed without a complicated ALD equipment or multiple grafting steps, yet is capable of achieving a reasonable degree of thickness control with nanoscale precision that is similar to ALD.

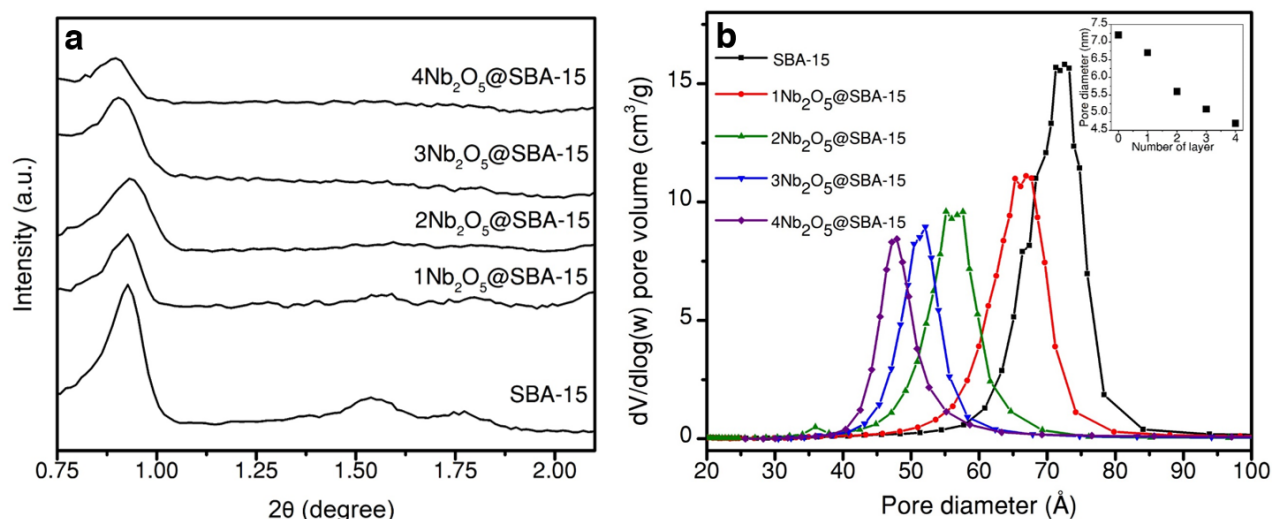


Figure 3.1.2 (a) Small-angle XRD results of uncoated and overcoated SBA-15. The peaks in SBA-15 from small to large angle represent the 100, 110 and 200 diffractions (2D $P6mm$ hexagonal symmetry).⁸⁸ (b) Pore size distributions of uncoated and overcoated SBA-15. The inset is the plot of the mean pore diameter versus the number of deposited niobia layers.

3.2 Structural and acid properties of $\text{Nb}_2\text{O}_5@\text{SBA-15}$ and bulk niobia

The overcoated SBA-15 samples were further characterized and compared with a commercial as well as a lab-synthesized bulk niobia (HY-340 and m- Nb_2O_5 , respectively). Because of the porous nature of our niobia overcoat, the silica functionality (e.g. silanol group) might remain accessible on the surface. Therefore, x-ray photoelectron spectroscopy was performed to investigate the surface compositions of $\text{Nb}_2\text{O}_5@\text{SBA-15}$ (**Figure 3.2.1**). The O 1s XPS results of SBA-15 and four overcoated samples showed a clear transition from a pure Si-O signal to a Nb-O signal. Although a very weak Si signal could still be detected ($\text{Nb/Si} = 9.4$, **Table 3.3-1**), we concluded that $4\text{Nb}_2\text{O}_5@\text{SBA-15}$ had nearly full Nb_2O_5 coverage on the surface according to the O 1s data. The signal of Nb 3d, on the other hand, provides information of the niobium environment. Both bulk niobia and the overcoated samples showed typical doublet peaks, which are known to be due to the spin-orbit coupling of the Nb 3d orbitals. The

binding energy of the doublet increases with a higher oxidation state of the niobium.^{89,90} The Nb 3d signals of the 4Nb₂O₅@SBA-15 and HY-340 almost overlap while the signals of m-Nb₂O₅ had lower binding energies, indicating there was an increasing Nb⁴⁺ character in m-Nb₂O₅. According to the model proposed by Kreissl et. al, Nb⁴⁺ exists as an oxygen-deficient five-coordinated center in the Nb₂O₅ network, which is structurally distinct from the typical octahedral NbO₆ unit. Accordingly, the Nb₂O₅ overcoat and HY-340 were likely comprised of mainly NbO₆ units but m-Nb₂O₅ had more pyramidal NbO₅ units on the surface.

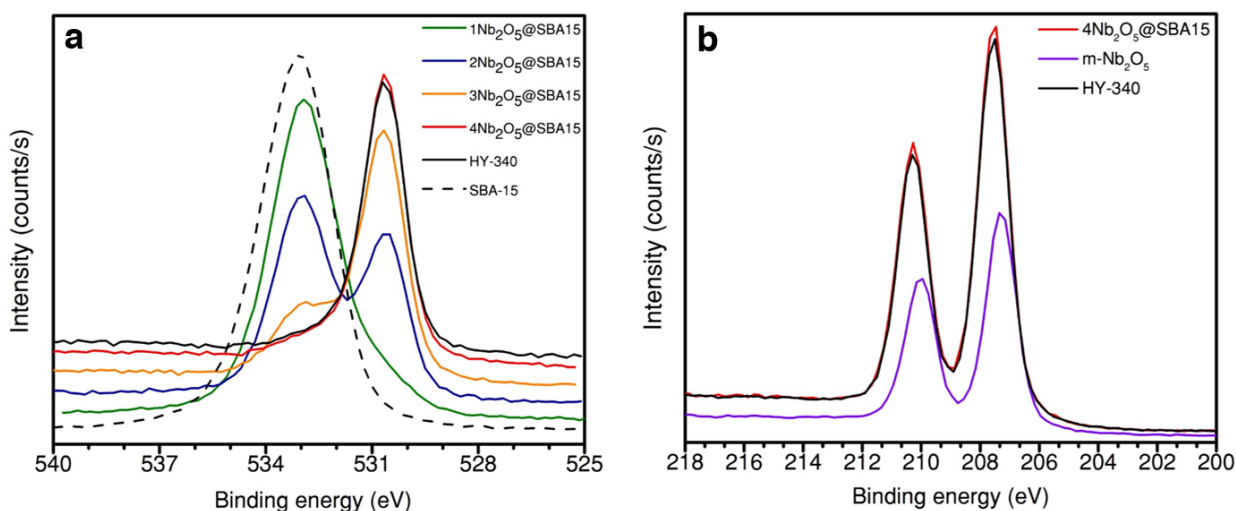


Figure 3.2.1 (a) O 1s XPS results for SBA-15, overcoated SBA-15 and HY-340 (b) Nb 3d results for 4Nb₂O₅@SBA-15, m-Nb₂O₅ and HY-340.

Acid catalysis is an important application for niobia. To evaluate this aspect of the overcoated material, the total acid sites of Nb₂O₅@SBA-15 and bulk niobia catalysts were quantified by ammonia temperature programmed desorption (NH₃-TPD) (**Table 3.3-1**). 4Nb₂O₅@SBA-15 had the largest number of total acid sites per weight among all samples since its S_{BET} outnumbered all bulk niobia samples. On the other hand, HY-340 had the largest

number of total acid sites per surface area among all materials but the number of acid sites were drastically reduced when being calcined at 500 °C (HY-340T). In this case, HY-340 underwent structural transformation from amorphous to pseudo-hexagonal phase during the thermal treatment (**Figure A.2.4**), which caused the loss of acid sites as previously reported.^{91,92} The as-synthesized m-Nb₂O₅ had an intrinsic pseudo-hexagonal structure and a similarly low number of acid sites as the thermally treated HY-340T. Interestingly, Nb₂O₅@SBA-15 retained their amorphous phase and large number of acid sites even after the pre-treatment at high temperature (500 °C), which was required to effectively remove the remaining precursor impurities during the synthesis. We attributed such resistance against crystallization to the formation of Si-O-Nb linkage between the overcoat and the support. The crystallization of niobia could be suppressed because of the stabilizing effect of this interfacial linkage. A similar observation was also previously reported when overcoating ZrO₂ on SBA-15.⁸⁶

It can be noticed that the total acid sites per surface area of Nb₂O₅@SBA-15 was considerably lower than both types of bulk niobia (**Table 3.3-1**), which could be explained by incomplete Nb₂O₅ coverage in the micropores of SBA-15. Indeed, silanol groups could still be observed by XPS, DRIFTS (**Figure A.2.5a**) and ¹H ssNMR (**Figure A.2.6**) for 4Nb₂O₅@SBA-15. We hypothesized that Nb(OEt)₅ is probably too bulky to effectively diffuse into the micropores of SBA-15 and react, thus leaving the presence of some unreacted Si-OH. Such phenomenon was also observed when ALD was used to overcoat Nb₂O₅ onto SBA-15.²⁹ Since the micropores were not completely filled by Nb₂O₅, they contributed to the surface area without contributing to the acid sites, thus lowering the acid site density for overcoated SBA-15. Furthermore, we quantified the Brønsted acid sites of bulk and overcoated niobia catalysts using DRIFTS-pyridine data (**Figure A.2.7**) and a reported ratio of extinction coefficients.⁹³ The ratio of two acid types were estimated using the integrated band area at 1445 cm⁻¹ and 1535 cm⁻¹, which contributed by the pyridine adsorbed on Lewis and Brønsted acid sites,

respectively. The catalysts with the highest Brønsted/Lewis acid site (B/L) ratio were HY-340 > m-Nb₂O₅ > 4Nb₂O₅@SBA-15. Lewis acid sites have been hypothesized to originate from niobium centers with lower coordination numbers and Brønsted acid sites are contributed by the Nb-OH groups associated to NbO₆ units.⁹⁴ Therefore, the acid characterization results of HY-340 and m-Nb₂O₅ were in a good agreement with the structural features indicated by XPS analyses, where the niobium in HY-340 had a higher coordination number than the niobium in m-Nb₂O₅. However, 4Nb₂O₅@SBA-15 and HY-340 should have a similar B/L ratio because XPS analyses suggested that their surfaces were mainly composed of NbO₆ units. We suggested that the much smaller B/L ratio (1/3) of 4Nb₂O₅@SBA-15 resulted from the self-condensation between Nb-OH groups during the calcination at 500 °C, which proceeded with a similar mechanism that occurs on amorphous silica surface.^{95,96}

3.3 Catalytic behavior of mesoporous Nb₂O₅ and bulk catalysts

To investigate the catalytic activity of overcoated SBA-15 as a solid acid, we used two typical acid-catalyzed reactions as probes: xylose dehydration and Friedel-Crafts alkylation. Dehydrating xylose to form furfural catalyzed by Nb₂O₅ has been widely investigated.^{97–99} Xylose is believed to first isomerize into xylulose over a Lewis acid site and further dehydrate to furfural, which is catalyzed by Brønsted acid sites.^{100,101} Accordingly, the selectivity of furfural is highly dependent on the ratio of Brønsted/Lewis acid sites in the catalyst.^{98,102} We performed xylose dehydration in a standard biphasic system (water/toluene) in order to continuously extract furfural from aqueous phase for avoiding its degradation by further rehydration and condensation reactions (e.g. levulinic acid and humin formation). 4Nb₂O₅@SBA-15 showed the highest conversion (91%) among all overcoated samples (**Figure 3.3.1**). However, the conversion of HY-340 was higher (96%) than that of 4Nb₂O₅@SBA-15 (91%), even though it had slightly fewer acid sites (**Table 3.3-1**). Despite

the high conversion, the furfural selectivity of HY-340 was much lower (44%) than that of overcoated catalyst, which was likely due to the condensation side reactions that occurred at nearly full conversion.¹⁰³ A higher selectivity could be obtained (50%) with a shorter reaction time (3 h), but HY-340 was still less selective towards furfural than other catalysts. Moreover, HY-340 calcined at 500 °C (HY-340T) also showed low selectivity towards furfural. We therefore suggested that the predominant Brønsted acidity (B/L ratio > 5) in HY-340 could have facilitated the aforementioned rehydration and condensation side reactions, thus lowering the selectivity towards furfural.

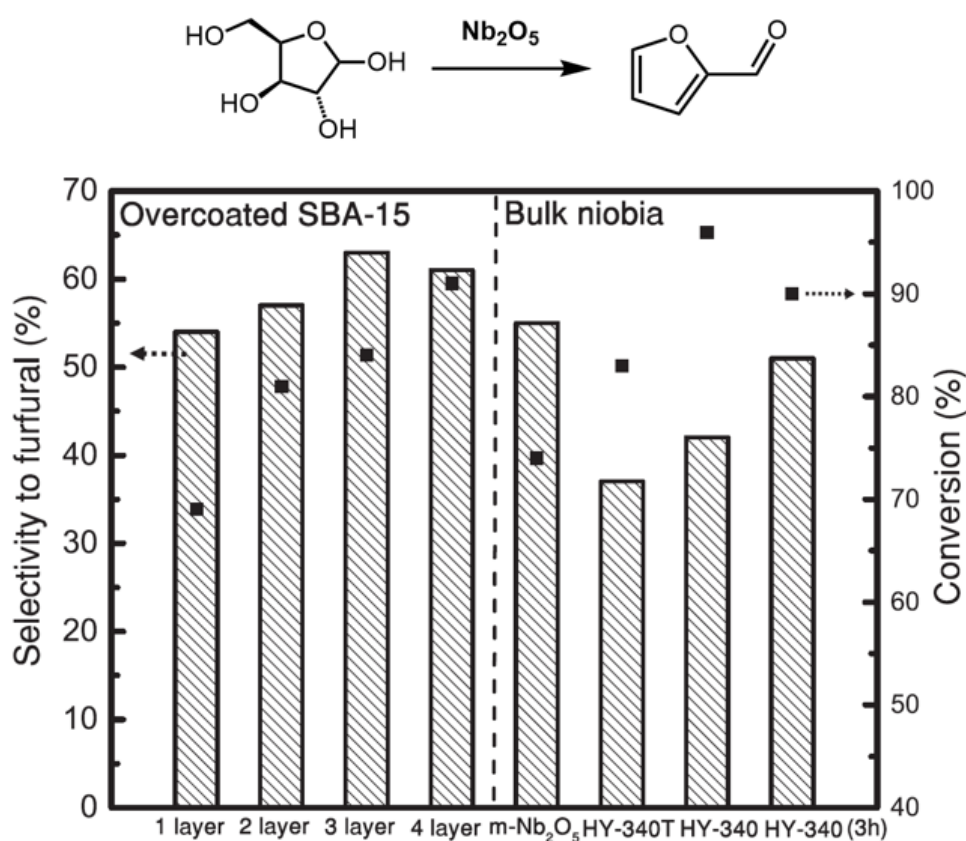


Figure 3.3.1 Results of xylose dehydration using different niobia catalysts. Points and bars represent conversion and furfural selectivity, respectively.

Table 3.3-1 Characterization data of overcoated and bulk niobia catalysts

Catalysts	S_{BET} (m^2/g)	Nb/Si ratio ^a	Total acid site ^b		Brønsted acid site ^c	Lewis acid sites ^d	Structure ^e
			$\mu\text{mol/g}$	$\mu\text{mol/m}^2$	$\mu\text{mol/g}$	$\mu\text{mol/g}$	
SBA-15	750	-	-	-	-	-	amorphous
1Nb ₂ O ₅ @SBA15	558	0.12	228	0.41	-	-	amorphous
2Nb ₂ O ₅ @SBA15	521	0.63	210	0.40	-	-	amorphous
3Nb ₂ O ₅ @SBA15	419	2.3	237	0.56	-	-	amorphous
4Nb ₂ O ₅ @SBA15	471	9.4	296	0.63	76	220	amorphous
m-Nb ₂ O ₅	91	-	139	1.53	79	60	TT-phase
HY-340	72	-	278	3.86	238	40	amorphous
HY-340T	67	-	97	1.45	-	-	TT-phase

^a Determined by XPS.

^b Determined by NH₃-TPD.

^{c,d} Determined by pyridine-DRIFTS and reported extinction coefficients.

^e Determined by XRD.

For overcoated SBA-15, the increasing conversion with each deposition cycle could be explained by the increasing extent of niobia coverage on the surface, which led to an increasing number of acid sites (especially Brønsted acid sites). At the same time, selectivity likely depends more on the ratio of Brønsted acid and Lewis acid sites. We think that the ratio remained fairly constant with the increasing coverage, so the selectivities did not vary as much as the conversions. Interestingly, slightly increased selectivities of 3Nb₂O₅@SBA-15 and 4Nb₂O₅@SBA-15 were observed. This result might be associated with some side reactions of xylose that occur in the solution. Increasing the conversion of xylose might lower the extents of those side reactions and hence slightly increase the selectivity. More importantly, the highest yield of furfural (56% at 3h) was obtained with 4Nb₂O₅@SBA-15. We attributed this high yield to its balanced B/L ratio, which maximized conversion while limiting the byproduct formation.

We further studied the activities of 4Nb₂O₅@SBA-15 and other bulk niobia materials during Friedel-Crafts alkylation (**Figure 3.3.2a**), which is an important reaction for arene substitution. Friedel-Crafts alkylation is typically catalyzed by Lewis acid sites but requires Brønsted acid sites when the alkylating reagent is an alcohol.^{104–106} The use of a solid acid and an alcohol alkylation agent is considered more environmentally friendly than traditional homogeneous Lewis acids (e.g. AlCl₃). We studied the benzylation of anisole using benzyl alcohol because such benzyl benzene derived molecules are considered industrially valuable.^{107,108} Specifically, two structural isomers (para- and ortho-benzyl anisole) and benzyl ether (side product) were obtained in this reaction. The four tested catalysts showed identical product distributions and similar selectivity towards benzylated products (**Figure 3.3.2b**). However, the differences in activity were distinct from that of xylose dehydration. Using 4Nb₂O₅@SBA-15 led to the highest conversion (84%) and yield of benzyl anisole (63%, including two isomers) at 3 h. In contrast, HY-340, the catalyst with the largest number of Brønsted acid sites, led to only 57% conversion. The lowest conversion was again obtained

over $m\text{-Nb}_2\text{O}_5$. HY-340T showed a reduced activity (37% of conversion) compared to HY-340, which was due to the loss of its acid sites after crystallization. We also noticed that the color of catalysts changed when the conversion reached nearly 100% (**Figure A.2.8**). We repeated the reaction using spent $4\text{Nb}_2\text{O}_5@\text{SBA-15}$ and a lower conversion was obtained (45%), which can be ascribed to the formation of some condensed byproducts that blocked acid sites. Therefore, the spent $4\text{Nb}_2\text{O}_5@\text{SBA-15}$ and HY-340 were regenerated by calcination at 500 °C for 1 h to remove carbonaceous deposits and the activities of regenerated catalysts were studied (**Figure 3.3.2c**). The conversion of $4\text{Nb}_2\text{O}_5@\text{SBA-15}$ at 3 h slightly decreased after first regeneration but it remained stable in the second and third catalytic runs. In contrast, the activity of HY-340 dropped after the second regeneration. Further XRD analyses showed that the structure of the regenerated HY-340 transformed into pseudo-hexagonal phase while $4\text{Nb}_2\text{O}_5@\text{SBA-15}$ remained amorphous (**Figure A.2.4b**). These results further suggested that the acid sites of $4\text{Nb}_2\text{O}_5@\text{SBA-15}$ had an exceptional resistance against thermal treatment, which could be advantageous in industrial processes where catalyst regenerations are required.

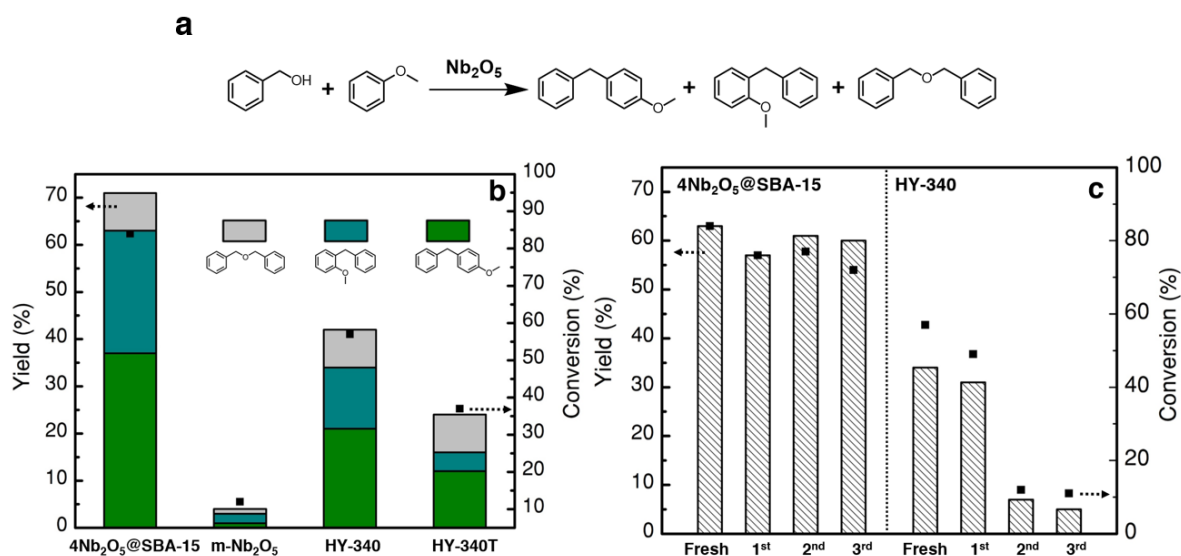


Figure 3.3.2 (a) Products that yield in the Friedel-Crafts alkylation using anisole and benzyl alcohol (b) Yield and distribution of products in the Friedel-Crafts alkylation catalyzed by different forms of niobia. (c) Catalyst stability tests of $4\text{Nb}_2\text{O}_5@\text{SBA-15}$ and HY-340 after regenerations. The yield is the sum of the two benzylated products.

As previously mentioned, the Brønsted acid sites are considered to be the active site in this Friedel-Crafts alkylation. Therefore, we determined the turnover frequency (TOF) of 4Nb₂O₅@SBA-15, HY-340 and m-Nb₂O₅ by dividing their extrapolated initial reaction rates by the numbers of Brønsted acid sites (**Figure 3.3.3a to c**). Interestingly, the TOF of 4Nb₂O₅@SBA-15 (0.06 s⁻¹) was 6 times higher than the TOF of HY-340 (0.009 s⁻¹) while m-Nb₂O₅ displayed a TOF that was one order of magnitude lower than that of 4Nb₂O₅@SBA-15 (TOF = 0.001 s⁻¹). We hypothesized that the variation in activity may result from the difference in acidity strength between these catalysts. DRIFTS-pyridine was then conducted and the spectra were collected at 300 °C (**Figure 3.3.3d**) to study the presence of strongly chemisorbed pyridine. The adsorbed pyridine species and their corresponding acid types were assigned according to previous reports in the literature.^{109,110} We observed only two peaks corresponding to Lewis acid sites on m-Nb₂O₅, whereas pyridines adsorbing on Brønsted acid sites were found on both 4Nb₂O₅@SBA-15 and HY-340. This result substantiated that the acidity of m-Nb₂O₅ was weaker, thus leading to a significantly lower TOF for Friedel-Crafts alkylation. On the other hand, both HY-340 and 4Nb₂O₅@SBA-15 had strong Brønsted acidity because of the presence of the peak at 1520 cm⁻¹, which is exclusively contributed by Brønsted acid sites. We further examined NH₃-TPD data (**Figure A.2.9**) and found that HY-340 had an extra desorption band at 380 °C, which cannot be found for 4Nb₂O₅@SBA-15. This result implied that HY-340 was more acidic, which led us to conclude that the acid strength cannot account for the higher activity of 4Nb₂O₅@SBA-15.

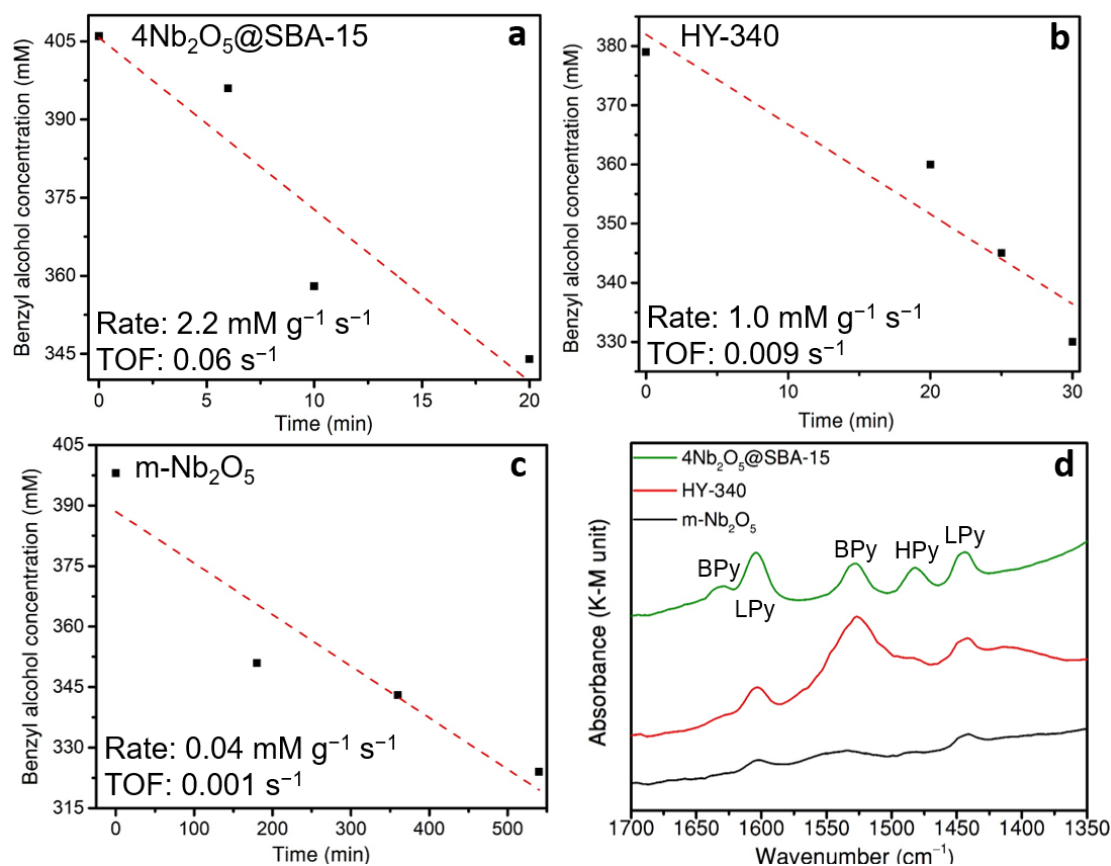


Figure 3.3.3 Kinetic study of Friedel-Crafts alkylation. Initial rate determination and TOF calculation for (a) $4\text{Nb}_2\text{O}_5@\text{SBA-15}$, (b) HY-340 and (c) $\text{m-Nb}_2\text{O}_5$. The initial reaction rates were determined by the extrapolation to time zero of the least squares fit of reactant concentration versus reaction time at conversions below 20%. The reaction conditions were the same as what is shown in the experimental section except the amount of catalyst added for $4\text{Nb}_2\text{O}_5@\text{SBA-15}$ and HY-340, which were reduced to 25 mg to maintain low conversion. (d) DRIFTS-Pyridine results. BPy, LPy and HPy denote pyridine adsorbing on Brønsted acid sites, pyridine adsorbing on Lewis acid site and H-bonded pyridine, respectively. The presented data were smoothed using the adjacent-averaging method with a 15-point window.

In order to elucidate the discrepancy in acid strength and catalytic activity between HY-340 and $4\text{Nb}_2\text{O}_5@\text{SBA-15}$, ^1H ssNMR measurements were conducted to characterize the surface hydroxyl groups at the atomic level (**Figure 3.3.4**). HY-340 showed a broad peak centered at 5.7 ppm and another narrower peak with much lower intensity at 2.7 ppm. In comparison, $4\text{Nb}_2\text{O}_5@\text{SBA-15}$ showed a broad peak centered at 4.9 ppm and two partially

overlapping peaks at 2.4 ppm and 2.2 ppm. The peak at 2.4 ppm was assigned to Nb–OH and the peak 2.2 ppm was assigned to the remaining silanol groups from the micropores of SBA-15 support (^1H ssNMR spectra of pure SBA-15 is shown in **Figure A.2.6**, confirming the silanol group assignment). Consequently, both niobia catalysts showed two Nb–OH species but the ratio of these two hydroxyl groups seemed to be different. Takagaki et al.^{106,111,112} have performed detailed studies on niobia and have assigned the broader peak to a hydrogen bonded proton and the narrower peak to a terminal Nb–OH. Takagaki et al. also suggested that the Nb–OH groups with hydrogen bonding, which contributed to the broad peak at higher ppms, had a stronger acidity. The high proportion of hydrogen bonded Nb–OH on HY-340 could have led to its stronger acidity, which is in a good agreement with our NH_3 -TPD analyses. Compared to HY-340, $4\text{Nb}_2\text{O}_5@\text{SBA-15}$ has more isolated Nb–OH groups that are less acidic than the hydrogen bonded ones. We attributed this result to the structural difference between $4\text{Nb}_2\text{O}_5@\text{SBA-15}$ and HY-340 and the hypothesized models are schematized (**Figure 3.3.4**). HY-340 is known to be a mixture of nanosized particulates and hydrogen bonds can form within their interlayers. Furthermore, acid quantification results also indicated that HY-340 had the highest density of Brønsted acid sites, which originated from the Nb–OH groups on the surface. This high density of the surface Nb–OH groups likely further promoted the hydrogen bond formation. In contrast, the niobia on $4\text{Nb}_2\text{O}_5@\text{SBA-15}$ has a two-dimensional structure because it was deposited as a thin film in the pores of SBA-15. This nanostructure likely led the niobia to have a longer distance between Nb_2O_5 surfaces, which disfavored hydrogen bond formation and increases the number of exposed isolated Nb–OH groups. We propose that the high activity of $4\text{Nb}_2\text{O}_5@\text{SBA-15}$ in Friedel-Crafts alkylation was due to its unique nanostructure and surface characteristics, which involves these isolated Nb–OH groups. The relatively sparse Nb–OH groups in the absence of hydrogen bonds could have lead anisole and benzyl alcohol to adsorb and react more easily compared to the case where a hydrophilic

hydrogen bond network is formed, which could be unfavorable to the adsorption of such hydrophobic substrates. Our findings reveal that strong acidity does not guarantee activity during acid catalysis. An acid catalyst with a desirable nanostructure could result in a higher catalytic performance even though it had slightly fewer and weaker acid sites.

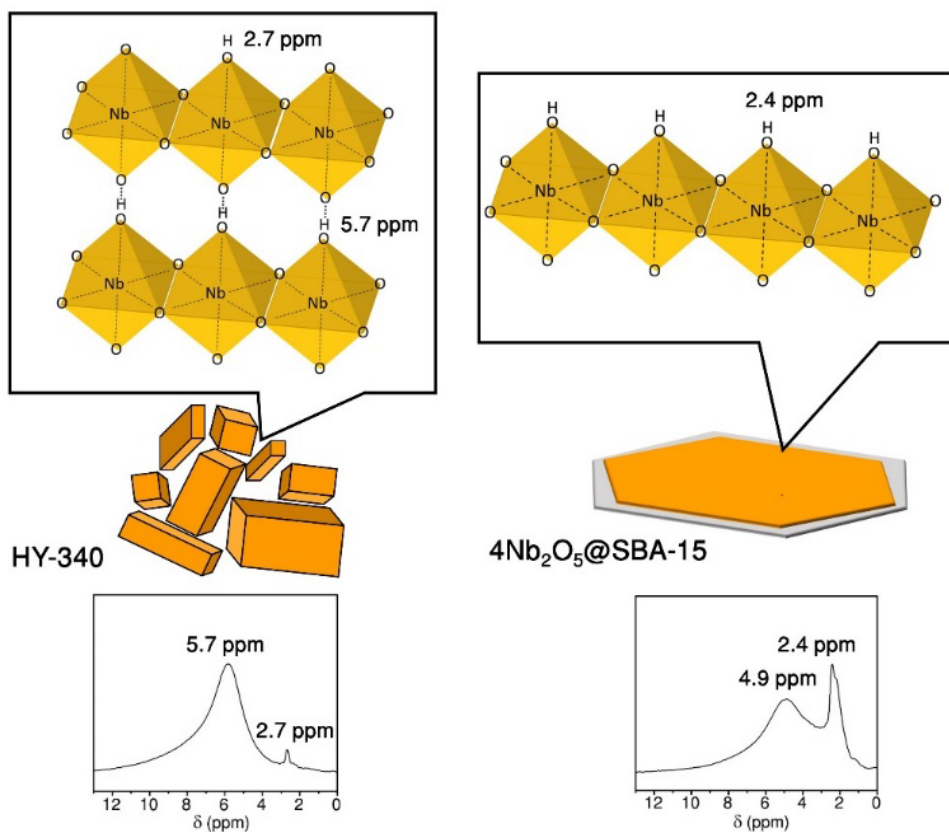


Figure 3.3.4 ^1H ssNMR spectra and associated proposed schematic structure of HY-340 and $4\text{Nb}_2\text{O}_5@\text{SBA-15}$.

3.4 Summary of Chapter 3

We used the chelation chemistry described in Chapter 2 to control the sol-gel kinetics of $\text{Nb}(\text{OEt})_5$ and develop a post-synthetic strategy to prepare a SBA-15 type mesoporous niobia with high surface area and narrow pore size distribution. This niobic acid exhibits superior catalytic activity in two probe reactions, namely xylose dehydration and Friedel-Crafts alkylation. The balanced ratio of Brønsted and Lewis acid sites on $\text{Nb}_2\text{O}_5@\text{SBA-15}$ resulted in a 10% higher selectivity towards furfural at the same conversion level compared to bulk HY-340 niobia. On the other hand, the nanostructure of overcoated catalyst restrained the formation of interlayer hydrogen bonds and the Brønsted acid sites that did not form hydrogen bonds appeared to be highly favorable for Friedel-Crafts alkylation with hydrophobic reactants. This structural advantage led to a 6 times higher TOF than that of HY-340 despite its weaker acidity. Importantly, the overcoat created Nb-O-Si linkage that inhibited the crystallization of Nb_2O_5 . The more stable amorphous structure of overcoated SBA-15 allowed the acid sites to endure high temperature thermal treatments (500 °C) which ensures that the activity can be fully recovered after catalyst regenerations. In contrast, this high temperature crystallized HY-340 and the mesoporous niobia synthesized using traditional template assisted methods, which irreversibly reduced the number of acid sites. Overall, not only did kinetically controlled overcoating provide an easy method for producing high-surface-area niobia catalysts with controlled mesopores, but it also led to unique structural stability and properties. Both phenomena, which were observed during different catalytic reactions, emphasize the importance of localized material structure in catalysis and could provide new insights and routes for the rational design of solid acid catalysts.

3.5 Experimental section of Chapter 3

Chemicals and Materials

All chemicals used in this study were analytical grade and obtained from commercial suppliers. They were used without further purification unless stated otherwise. Air and moisture-sensitive reagents were handled using a nitrogen filled glove box or a standard Schlenk line apparatus. Xylose, anisole, and benzyl alcohol, Pluronic 123 (P123), ethyl acetoacetate and decane were purchased from Sigma Aldrich. Tetraethyl orthosilicate (TEOS), 2-furaldehyde (furfural) and tetramethyl orthosilicate (TMOS) were purchased from Acros. $\text{HCl}_{(\text{aq})}$ (ca. 37%) was purchased from Merck. Ethanol was purchased from Fisher Scientific. Niobium (V) ethoxide ($\text{Nb}(\text{OEt})_5$) was purchased from ABCR. $\text{NH}_{3(\text{aq})}$ (ca. 25%) and toluene were purchased from VWR Chemicals. Dioxane was purchased from Roth. Hydrated niobium oxide ($\text{Nb}_2\text{O}_5 \cdot n\text{H}_2\text{O}$, HY-340) was provided free of charge by Companhia Brasileira de Metalurgia e Mineração (CBMM). Furfural and EAA were purified by distillation under reduced pressure prior to being used. The water used in this study was purified by a Millipore Milli-Q Advantage A10 water purification system until its resistivity was higher than 18 $\text{M}\Omega \cdot \text{cm}$. All gases were purchased from Carbogas.

Material synthesis

HY-340 was pretreated by calcination at two different temperatures for 3 h. HY-340 calcined at 300 °C is simply denoted as HY-340 whereas HY-340 calcined at 500 °C is denoted as HY-340T. Silica spheres and SBA-15 were synthesized using the same procedures described in A.1.1. Mesoporous niobia (m- Nb_2O_5) was synthesized following a reported method.²⁵ Briefly, 1 g P-123 was mixed with 10 g of ethanol. This solution was then mixed with 2 g of NbCl_5 while vigorous stirring was applied. The solvent of the resulting mixture was then slowly

evaporated and the resulting solid was aged in air at 40 °C for 2 days. After aging, the gel was calcined in a muffle furnace at 400 °C for 5 h.

To synthesize overcoated samples, we applied a methodology similar to our previous work where we first calculated the quantity of Nb(OEt)₅ that was necessary to achieve single atomic monolayer coverage by dividing the S_{BET} of substrate by the Van Der Waals projection area of Nb(OEt)₅ (0.765 nm², estimated by MarvinSketch).¹¹³ For 0.5 g SBA-15 (S_{BET} = 750 m²/g), the monolayer amount of Nb(OEt)₅ (i.e. for synthesizing 1Nb₂O₅@SBA-15) was 0.8 mmol. As shown in Chapter 2, we used EAA to chelate aluminum sec-butoxide in order to slow down the gelation rate of alumina for sol-gel overcoating. Similarly, the precursor in Chapter 3 was prepared by mixing Nb(OEt)₅ with 3 equivalent amount EAA under N₂ atmosphere. This led to a slower condensation rate and prevented uncontrolled Nb₂O₅ precipitation during sol-gel coating.¹¹⁴ Subsequently, the mixture was diluted with ethanol and the final volume of the precursor was fixed to 10 mL. The resulting precursor solution was stirred at ambient temperature for 18 h. The general synthesis method for xNb₂O₅@SBA-15 was as follows: 0.5 g SBA-15 was dispersed in a mixture containing ethanol, water and NH_{3(aq)}. The quantities of water and ethanol in the suspension were proportional to the number of moles of injected Nb(OEt)₅. Specifically, the molar ratio of Nb(OEt)₅, water and ethanol was kept to 1:5:535. The volume of 25 wt% NH_{3(aq)} in the suspension was fixed at 0.02 mL. The coating was initiated by injecting the aforementioned precursor solution into the suspension using a KDS 100 legacy syringe pump and the injection rate was set to 1.5 mL/min. The suspension was vigorously stirred, soaked in an ice bath during the injection process and then kept at room temperature for 18 h after the injection was completed.

12Nb₂O₅@SiO₂ was synthesized using a similar protocol: 5 g Stöber silica was dispersed in a solution containing 50 mL ethanol, 0.04 mL NH₃ and 0.75 mL H₂O. A mixture of 1.6 mmol Nb(OEt)₅, 4.8 mmol EAA and 9 mL ethanol was then injected into the suspension

at the rate of 1.5 mL/min. The subsequent experimental conditions are the same as the procedure for $x\text{Nb}_2\text{O}_5@\text{SBA-15}$. All the overcoated samples were thoroughly washed with ethanol and water and calcined at 500 °C for 3 h to remove the remaining organic impurities.

Catalyst characterization

Physisorption, NH_3 -TPD, Pyridine-DRIFTS, XRD, TEM and STEM were all performed using the same instruments and procedures described in section 2.8. ^1H magic-angle spinning solid-state nuclear magnetic resonance experiments were performed on a Bruker 400MHz spectrometer equipped with a 2.5 mm probe. A regular spin echo program with a spinning rate of 35 kHz was used to acquire the spectra. Prior to the NMR measurements, the physisorbed water of samples was removed at 120 °C under reduced pressure for 3 h. The samples were packed in NMR rotors in a glove box under inert atmosphere.

Catalytic test

Xylose dehydration was performed in an Alltech 10 mL thick-walled glass reactor. Typically, 75 mg xylose was dissolved in 2 mL H_2O and mixed with 3 mL toluene. 100 mg of catalyst was then loaded into the reactor and mechanically stirred (550 rpm) at 120 °C for 5 h. The organic phase was analyzed by an Agilent Technologies 7890 A gas chromatography equipped with a flame ionization detector and a HP-5 column (50 m, 0.32 mm). The aqueous phase was analyzed by an Agilent Technologies 1260 infinity high performance liquid chromatography equipped with a refractive index detector, a UV-Vis detector and a Bio-Rad Aminex HPX-87H column. The chromatography was carried out with a flow rate of 0.6 mL/min at 60 °C using 5 mM $\text{H}_2\text{SO}_{4(\text{aq})}$ as the mobile phase. The products were quantified using calibration curves produced by diluting analytical grade standards.

Friedel-Crafts alkylation was performed in an Alltech 10 mL thick-walled glass reactor. Typically, 50 mg catalyst was mixed with 1 mmol benzyl alcohol and 20 mmol anisole. The

reaction proceeded by stirring the mixture (550 rpm) at 130 °C for 3 h. The products were diluted with dioxane and analyzed by GC-FID. Benzyl alcohol was quantified using a calibration curve obtained produced by diluting a commercial standard while the three other products were quantified by using the effective carbon number method with decane as an internal standard.^{69,115} The absence of significant mass transfer limitations for both reactions was confirmed by using the experiments with different stirring rates and by applying the Weisz–Prater criterion, which is shown in section A.2.2.

Chapter 4 Sol-gel Overcoating on Atomically Dispersed Pre-catalysts

This chapter is adapted with the consent of all the authors from an unpublished manuscript entitled “Engineering ZrO₂-Pd interface for selective CO₂ hydrogenation by overcoating atomically dispersed Pd pre-catalyst” by **Yuan-Peng Du**, Florent Héroguel, Ali M. Bahmanpour, Luka Milošević, Florent Héroguel, Oliver Kröcher and Jeremy S. Luterbacher.

4.1 Design of atomically dispersed pre-catalyst compatible with sol-gel coating

In Chapter 2, I have described Al₂O₃ deposition on supported metal that can be used to mitigate thermal sintering and create interfacial site comprising metal oxide and metal nanoparticles. However, overcoated catalysts systematically had fewer active sites (i.e. a decreased dispersion value after coating). For instance, after overcoating Al₂O₃ on Cu/Al₂O₃, only 38% of original Cu sites remained accessible. Since the nanoparticles are usually the costliest part of supported metal catalysts, especially when noble metals are used, developing a complementary strategy for maintaining high metal dispersion after overcoating would be beneficial for increasing the attractiveness of overcoating for practical applications. Both experimental and computational observation have shown that the atoms on particular facets in nanoparticles can react with metal oxide precursors.^{23,116} The loss of metal sites supposedly results from these overcoat-nanoparticle interaction. Since overcoat can resist particle sintering, I attempted to develop a synthetic strategy to prepare an atomically dispersed “pre-catalyst” (i.e. a material prior to being overcoated and reduced) comprising coordinated metal complex. The metal complex supposedly can mitigate the loss of active site by avoiding the direct

interactions between nanoparticles and metal oxide precursors. Moreover, overcoating this pre-catalyst would allow us to limit particle sintering during thermal activation step, leading to smaller nanoparticles with greater number of active sites.

Ethylenediamine (en) is a known bidentate ligand that can form complexes with noble metals. Alkoxysilane containing this chelating functionality {[3-(2-Aminoethylamino)propyl]trimethoxysilane} have been used to prepare SiO₂ supported metal catalysts through sol-gel processing.^{117,118} Our synthesis approach here relies on the same chemistry, where the chelated Pd was grafted on SiO₂ surface through the condensation of Si-(OCH₃)₃ with silica's surface hydroxyl groups (step 1, **Figure 4.1.1**), which produced an atomically dispersed Pd/SiO₂ (Pd(en)₂/SiO₂). The completion of grafting can be visibly seen from the color change of silica and the reaction medium. The colors of the chelated Pd solution and silica were light yellow and white, respectively. After heating the mixture at 80 °C overnight, the supernatant turned colorless and the silica support turned yellow (**Figure A.3.1**). Fourier-transform infrared spectroscopy also showed the presence of two bands at 2937 and 2883 cm⁻¹ that could be assigned to C-H stretching, which confirmed the presence of the Pd complex on silica surface (**Figure A.3.2**).¹¹⁹ Pd(en)₂/SiO₂ was then overcoated with ZrO₂ using a kinetically controlled sol-gel method that is similar to what we had presented for alumina and niobia in the previous chapters.^{113,120} We slowed down the hydrolysis and condensation rates of Zr(t-BuO)₄ by adding EAA to form a chelated ZrO₂ precursor.¹²¹ The kinetically controlled precursor was injected into a Stöber solution with the dispersed Pd(en)₂/SiO₂ particles to grow the ZrO₂ overcoat (step 2, **Figure 4.1.1**). Importantly, the Pd(en)₂ complex remained unreactive because of the strong interaction between ethylenediamine and Pd. Therefore, the surface Pd did not leach when performing liquid phase coating during which another chelating agent (EAA) is also present in the solution. Although Pd can also be complexed by the amine group of arginine, the resulting complex is anchored on the silica surface via the carboxylic acid group.¹²² In the absence of

acid or high temperature, carboxylic acid groups may interact with silica by electrostatic interaction rather than surface condensation. In comparison, we grafted the $\text{Pd}(\text{en})_2$ complex by forming a covalent siloxane linkage, which was likely more stable than electrostatic forces. We had also overcoated an impregnated silica containing strongly electrostatically adsorbed Pd and most of the Pd leached during the coating procedure.¹²³ Accordingly, we suggested that using organo-functionalized silane resulted in the most stable atomically dispersed Pd material that is compatible with kinetically controlled sol-gel coating. After overcoating, this pre-catalyst is activated to form the final Pd catalyst by calcining and reducing the $\text{ZrO}_2@\text{Pd}(\text{en})_2/\text{SiO}_2$ at 400 °C. The same thermal treatments were also performed on uncoated $\text{Pd}(\text{en})_2/\text{SiO}_2$ to form g-Pd/SiO₂ in order to compare the effect of the overcoat on the nanoparticle size distribution.

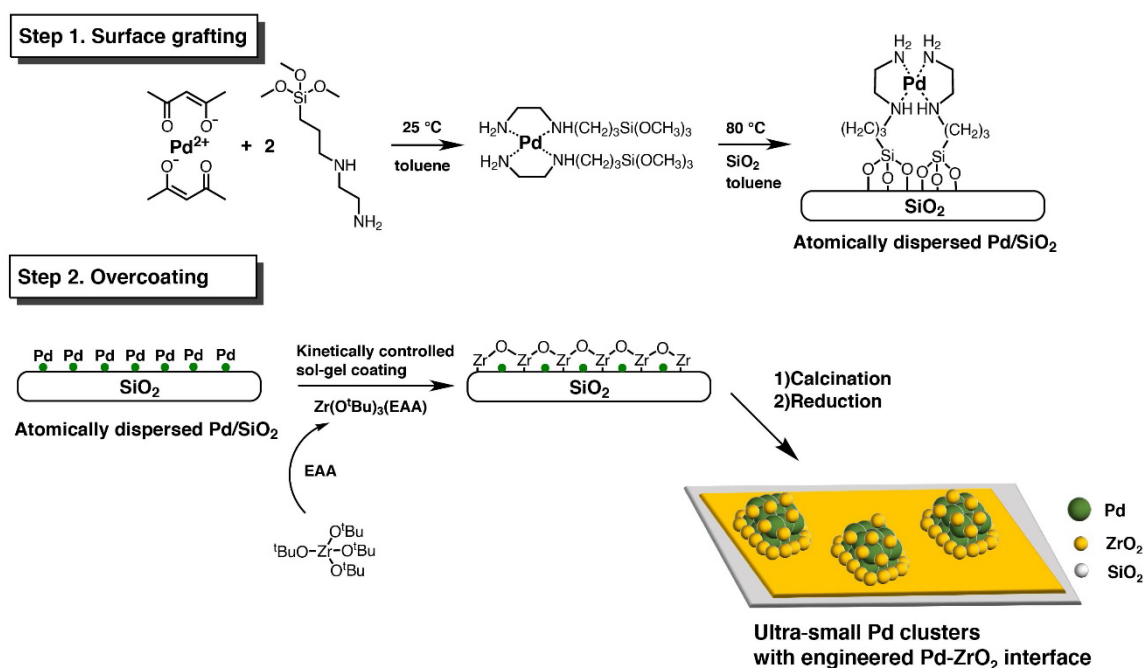


Figure 4.1.1 Synthesis of ultra-small Pd clusters with a ZrO₂ interface using sol-gel overcoating and the coordination chemistry of ethylenediamine and Pd.

We first determined the dispersions of $\text{ZrO}_2@\text{Pd}/\text{SiO}_2$ and $\text{g-Pd}/\text{SiO}_2$ using CO chemisorption and inductively coupled plasma optical emission spectrometry. Pd dispersion was twice as higher on $\text{ZrO}_2@\text{Pd}/\text{SiO}_2$ compared to $\text{g-Pd}/\text{SiO}_2$ (**Table 4.1-1**). STEM further showed that the particle size and the average Pd size was 3.4 nm on $\text{g-Pd}/\text{SiO}_2$ (**Figure 4.1.2a**). Unfortunately, we were unable to observe Pd particles and measure particle size distribution on $\text{ZrO}_2@\text{Pd}/\text{SiO}_2$ because of the poor contrast between Pd and ZrO_2 (**Figure A.3.3**). Therefore, we prepared $\text{Al}_2\text{O}_3@\text{Pd}/\text{SiO}_2$ using a similar method as that described in Chapter 2 as we expected that the higher contrast between Al_2O_3 and Pd would enable us to analyze Pd particles using STEM. Indeed, a much better contrast was obtained and we observed many sub-nanometer Pd clusters when analyzing $\text{Al}_2\text{O}_3@\text{Pd}/\text{SiO}_2$. The average particle size was significantly smaller (1.4 nm) than that of $\text{g-Pd}/\text{SiO}_2$, confirming the dispersion results analyzed using chemisorption (**Figure 4.1.2b**). Because the dispersion of $\text{Al}_2\text{O}_3@\text{Pd}/\text{SiO}_2$ was very close to that of $\text{ZrO}_2@\text{Pd}/\text{SiO}_2$ (**Table 4.1-1**), we inferred that $\text{ZrO}_2@\text{Pd}/\text{SiO}_2$ also has similarly small Pd clusters. These results strongly suggested that the overcoat can inhibit the growth of Pd particles during thermal activation and further highlight how overcoating techniques can be used to synthesize sintering resistant catalyst.^{23,36,124,125} From the EDX mapping (**Figure 4.1.2c and d**), we found that both ZrO_2 and Al_2O_3 can also be uniformly coated on an industrially-relevant SiO_2 support (Aerosil 200) using kinetically controlled sol-gel methods. More importantly, by growing a uniform overcoat on atomically dispersed $\text{Pd}(\text{en})_2/\text{SiO}_2$, we could limit the growth of Pd particles during the thermal activation step, thus forming sub-nanometer Pd clusters. Unlike a recently reported analogous approach, our procedure here does not require expensive organometallic complex or an atomic layer deposition instrument.¹²⁶ Although organometallic complexes are known precursors for preparing single site catalysts, they are usually moisture sensitive, which is not compatible with less expensive sol-gel processes where water is present in the reaction media. $\text{Pd}(\text{en})_2/\text{SiO}_2$ is

fairly inert and can be stored in an ambient environment. The stable characteristic makes Pd(en)₂/SiO₂ an ideal pre-catalyst for synthesizing catalysts with inverted metal oxide-metal interfaces, which might possess different catalytic properties from that of regular metal-metal oxide interfaces found in supported metal catalysts. Here, we took advantage of the stabilization effects of overcoat and exemplified the use of Pd(en)₂/SiO₂ for synthesizing ultra-small Pd clusters with Al₂O₃-Pd or ZrO₂-Pd interfaces. The characterization of g-Pd/SiO₂ suggested that preparing well-dispersed Pd/SiO₂ is challenging even at low loading because the interaction between Pd and SiO₂ is not particularly strong.¹²⁷ Therefore, introducing this pre-catalyst to coating procedure can significantly minimize the loss of the external Pd surface compared to the case where larger sized Pd particles had been formed on SiO₂ prior to metal oxide deposition. Moreover, this method can be applied to other metal oxide supports apart from SiO₂. We also prepared Pd(en)₂/ZrO₂ and overcoated it with ZrO₂ to form ZrO₂@Pd/ZrO₂. This catalyst displayed a higher dispersion (70%, **Table 4.1-1**) than that of ZrO₂@Pd/SiO₂, which could be explained by the stronger interaction between Pd and the ZrO₂ support.¹²⁸ We prepared a reference Pd/ZrO₂ using a standard impregnation method with the same Pd precursor and found that Pd was also highly dispersed (89%, **Table 4.1-1**). Importantly, there was not a large difference between ZrO₂@Pd/ZrO₂ and Pd/ZrO₂ with respect to Pd dispersion. Similar to previous studies, the lower dispersion in the overcoated catalyst might be caused by the capping effects of the overcoat. Loss of active sites during overcoating is an issue that is challenging to solve.^{52,129,130} It occurs during ALD processes because, according to density functional theory (DFT) simulation, metal oxide precursors can interact with specific facets of nanoparticles.¹¹⁶ The non-hydrolytic sol-gel coating method discussed in Chapter 2 similarly blocked a high proportion of Pt sites.⁷⁴ The small difference in dispersion between ZrO₂@Pd/ZrO₂ and Pd/ZrO₂ emphasizes the advantage of using atomically dispersed material for catalyst design. We hypothesized that the complexation of Pd can avoid the direct

interaction between precursor and Pd, thus maintaining a fairly high accessibility to the metal after overcoating.

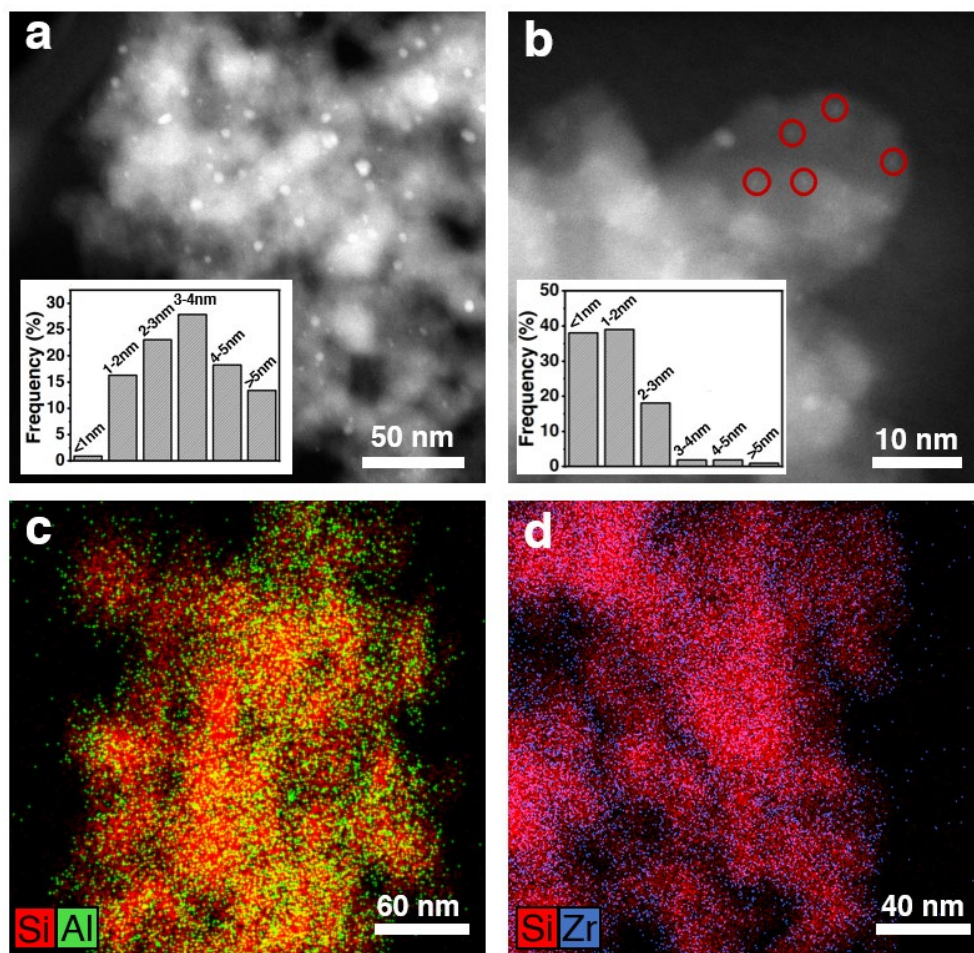


Figure 4.1.2 TEM images and Pd particle size distributions of (a) g-Pd/SiO₂ and (b) Al₂O₃@Pd/SiO₂ and EDX mappings of (c) Al₂O₃@Pd/SiO₂ and (d) ZrO₂@Pd/SiO₂. The sub-nanometer Pd particles detected in panel b are highlighted by red circles.

The physical and chemical properties of the overcoated and reference catalysts were further characterized. The N₂ physisorption isotherms showed that Al₂O₃@Pd/SiO₂ and ZrO₂@Pd/SiO₂ have nearly the same hysteresis loops as that of g-Pd/SiO₂ (**Figure A.3.4a**). These three catalysts also had similar BET surface areas (with less than a 10% reduction after overcoating and sometimes a slight increase). These results were distinct from precious

observations in ZrO₂-ALD processes where the overcoated catalysts showed reduced S_{BET} (from 100 to 66 m²/g).⁴⁸ We analyzed ZrO₂@Pd/SiO₂ and found that the thickness of ZrO₂ overlayer was roughly 1.5 nm after injecting 20 monolayer equivalents (defined by molecular projection of the precursor on the BET surface area of the catalyst) of precursor (**Figure A.3.3b**). The thickness of a ZrO₂ monolayer (0.075 nm) was greater than that of ZrO₂ prepared using ALD (0.02 nm/cycle).⁴⁸ Furthermore, ZrO₂@Pd/ZrO₂ even showed a surface area that was approximately 20% larger and its hysteresis loop slightly modified compared to the uncoated Pd/ZrO₂ (**Figure A.3.4b**). These results indicated that this sol-gel method could produce a more porous ZrO₂ overcoat, which was in a good agreement with the observations in Chapters 2 and 3.

Table 4.1-1 Characterization results of overcoated and reference catalysts

Catalyst	Loading ^a (wt%)	S _{BET} (m ² /g)	Pd _{surface} ^b (μmol/g)	d _{Pt} ^c (nm)	Dispersion ^d (%)	Rate ^e (mmol CO ₂ /Pt·s)
g-Pd/SiO ₂	0.39	170.1	6.9	3.4	19	0.16
ZrO ₂ @Pd/SiO ₂	0.28	162.1	9.9	N/A	38	4.7
Al ₂ O ₃ @Pd/SiO ₂	0.32	170.9	12.0	1.4	40	1.0
ZrO ₂ @Pd/ZrO ₂	0.34	76.8	22.1	N/A	70	3.6
Pd/Al ₂ O ₃	0.4	164.1	13.4	2.6	36	2.3
Pd/ZrO ₂	0.57	64.3	47.3	N/A	89	4.5

^a Determined by ICP-OES.

^b Determined by CO chemisorption.

^c Determined by STEM, Pd supported on ZrO₂ or with ZrO₂ overcoat cannot be observed due to the insufficient contrast.

^d Pd dispersion, calculated by Pd_{surface}/total Pd.

^e Calculated using the initial conversion value we obtained. Since the active site (metal-metal oxide interface) for CO₂ hydrogenation is hard to quantified, the rate was normalized by total amount of Pd.

The catalytic properties of Pd could be altered depending on the type and the nanostructure of its support, which have important effects on some reaction.^{48,131} In this context, overcoating could create additional surface functionality on uncoated catalyst even though a relatively inert support (e.g. SiO₂) was used initially. XPS was performed to characterize the overcoated and reference catalysts. The deconvoluted spectra showed that 95% of Pd was in metallic form (**Figure 4.1.3a**) when being supported on SiO₂. In comparison, Al₂O₃@Pd/SiO₂ had an increased proportion of PdO with the new Pd/PdO ratio (5.6) being nearly the same as that of Pd/Al₂O₃ (**Figure 4.1.3b and c**), indicating that the Al₂O₃ overcoat could modulate the chemical state of the Pd nanoparticles. Deconvoluting XPS data of the catalysts containing ZrO₂ was more challenging due to the presence of two intense Zr 3p peaks in the same binding energy region (**Figure A.3.5**). However, more intense PdO signals were still on both ZrO₂@Pd/SiO₂ and ZrO₂@Pd/ZrO₂, compared to Pd/ZrO₂ where the metallic Pd was still the most dominant. We attributed this high proportion of Pd^{II} to the small particle size (less than 2 nm) and the presence of the ZrO₂ overcoat. Both catalysts possessed ultra-small Pd clusters embedded in the ZrO₂ overcoat and the strong interaction between Pd and the ZrO₂ framework could have increased the oxidation state of Pd clusters. A similar trend was also observed when embedding Pd single atoms in metal oxide network.¹³² Based on these characterization results, designing heterogeneous catalysts using overcoating can not only produce the unique inverted metal-support interfaces (metal oxide-metal-metal oxide) but also modify the chemical properties of nanoparticles.

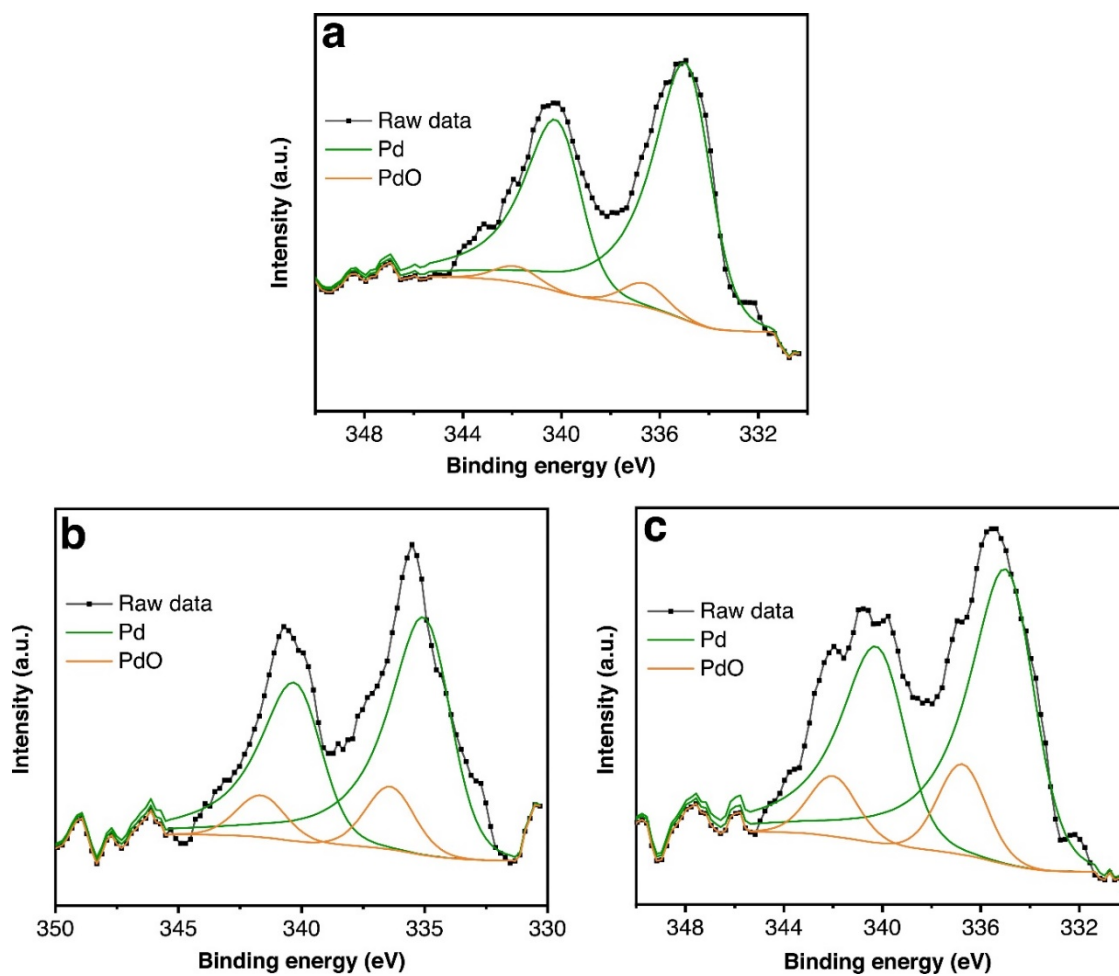


Figure 4.1.3 XPS results of (a) g-Pd/SiO₂, (b) Al₂O₃@Pd/SiO₂ and (c) Pd/Al₂O₃

4.2 CO₂ hydrogenation study

Many studies have concluded that metal-metal oxide interfaces play an important role during the catalytic conversion of CO₂.¹³³ Specifically, DFT simulation showed that the metal-metal oxide interface can facilitate the chemisorption of CO₂, which is the first step in the CO₂ conversion mechanism.^{54,133} The importance of metal oxides and/or other promoters was also experimentally identified when studying CO₂ hydrogenation using Pd supported on activated carbon.¹³⁴ At atmospheric pressure, the activated (i.e. adsorbed) CO₂ intermediate could be subsequently converted into CO or/and CH₄ (via reverse water-gas shift (RWGS) or/and methanation). Engineering metal-metal oxide interfaces using overcoating could represent a promising strategy to design active catalysts with improved thermal stability for CO₂ conversion.

To test this hypothesis, CO₂ hydrogenation was run using a quartz tubular at 450 °C and 1 atm. We chose a relatively high temperature in order to study the stability of Pd clusters at conditions favoring thermal sintering. g-Pd/SiO₂ showed a fairly high selectivity towards CO (above 80%) but a very low conversion (approximately 2%, **Figure A.3.6a**), which was in agreement with a previous study.¹³⁵ Selectivities towards CO and CH₄ (**Figure A.3.6a and b**) for this control catalyst remained stable over 20 h time-on-stream. The low conversion of g-Pd/SiO₂ could be attributed to the slow activation of CO₂ on the relatively inert silica support. Using Pd supported on Al₂O₃ significantly increased the conversion (**Figure A.3.7a**). Although the higher conversion could be partially ascribed to the higher dispersion of Pd/Al₂O₃, the rate of this catalyst was one order of magnitude higher than that of g-Pd/SiO₂ (**Table 4.1-1**), which made dispersion unlikely to be able to explain the lower reaction rate of g-Pd/SiO₂ alone.

Several studies have indicated that the nature of catalyst supports highly affect the reaction rate of CO₂ hydrogenation.^{134,136} The interfacial sites created when supporting Pd on

Al₂O₃ may be more favorable for CO₂ chemisorption, thus increasing the rate of CO₂ conversion. Despite its higher activity, Pd/Al₂O₃ was less selective with approximately 45% CH₄ selectivity (**Figure A.3.7b**). According to Wang et al., the selectivity of Pd/Al₂O₃ is highly dependent on Pd particle size and smaller Pd particles are more selective towards CO.¹³⁷ To study the effects of particle size and Al₂O₃ overcoat on CO₂ hydrogenation, Al₂O₃@Pd/SiO₂ was tested for CO₂ hydrogenation. This catalyst also showed a significantly higher rate (1 mmol CO₂/Pt·s, **Table 4.1-1**) compared to g-Pd/SiO₂ due to the formation of Al₂O₃-Pd interface and smaller Pd clusters. The selectivity of Al₂O₃@Pd/SiO₂ was also improved. The initial measured CO selectivity reached 90% and CH₄ selectivity was only 5% (**Figure A.3.7c and d**). Although smaller Pd clusters tend to catalyze reverse water gas shift and produce CO, selectivities above 90% has never been reported using Pd/Al₂O₃ even when Pd was nearly atomically dispersed.^{134,137} Unfortunately, we further observed that the yield of CO rapidly dropped with prolonged time-on-stream while the conversion and low CH₄ selectivity remained relatively unchanged. The reduced carbon balance indicated that this catalyst was catalyzing the formation of carbonaceous deposits. The formation of such carbon species is not uncommon during hydrocarbon conversion over acidic catalyst (i.g. zeolite).¹³⁸ The Pd clusters located on the mixed Al₂O₃-SiO₂ interface appeared to have distinct catalytic properties from those of either Pd/Al₂O₃ or Pd/SiO₂. We hypothesized that this Al₂O₃-SiO₂ interface could have acted as an acid site and converted CO₂ intermediates into carbon deposits. NH₃-TPD also revealed that Al₂O₃@Pd/SiO₂ had more acid sites than Pd/Al₂O₃ (**Figure A.3.8**). Consequently, even though some interesting properties and high initial CO selectivity were observed using Al₂O₃@Pd/SiO₂, the poor carbon balance over extended period of time limits its practical use.

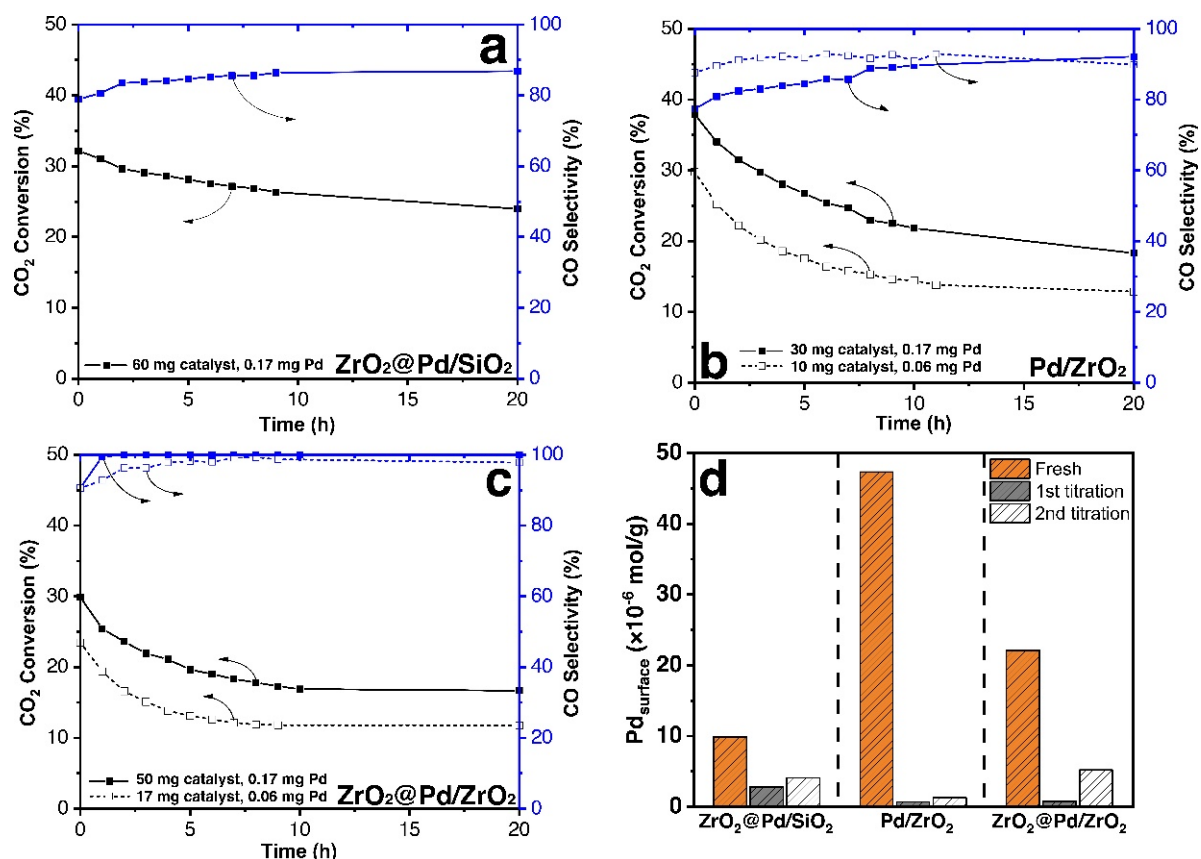


Figure 4.2.1 CO₂ hydrogenation of (a) ZrO₂@Pd/SiO₂ (b) Pd/ZrO₂ and (c) ZrO₂@Pd/ZrO₂. To be able to compare the conversions directly, the mass of added catalyst was adjusted to always have the same Pd quantities in the reactor. (d) CO chemisorption analyses of fresh and spent catalysts.

Besides Al₂O₃, ZrO₂ has also frequently been used to prepare catalysts, especially for producing methanol from CO₂.^{139,140} Both theoretical calculations and *in-situ* experiments have observed that CO₂ can adsorb and then be activated on ZrO₂ surface.¹⁴¹ Thus, another series of catalysts prepared with ZrO₂, both as support and overcoat, were also studied. Similar to Al₂O₃@Pd/SiO₂, the activity was significantly improved after overcoating ZrO₂ on Pd/SiO₂, confirming the high reactivity of Pd-ZrO₂ interfaces (**Figure 4.2.1a**). More importantly, ZrO₂@Pd/SiO₂ outperformed any catalysts containing Al₂O₃. Because Pd/Al₂O₃, Al₂O₃@Pd/SiO₂ and ZrO₂@Pd/SiO₂ have similar dispersions (**Table 4.1-1**), we concluded that the Pd-ZrO₂ interface is more active for catalytic CO₂ transformation than the Pd-Al₂O₃

interface. Moreover, the use of $\text{ZrO}_2@\text{Pd}/\text{SiO}_2$ not only led to a high CO selectivity (80%) but also showed little deactivation. Unlike $\text{Al}_2\text{O}_3@\text{Pd}/\text{SiO}_2$ that showed pronounced carbon deposition over time, $\text{ZrO}_2@\text{Pd}/\text{SiO}_2$ maintained a carbon balance over 95% and both CO and CH_4 selectivities (**Figure A.3.9a**) remained stable for 20 h. Since the results of $\text{Al}_2\text{O}_3@\text{Pd}/\text{SiO}_2$ and $\text{Pd}/\text{Al}_2\text{O}_3$ indicated that distinct catalytic properties can be found on the mixed oxide interface, we subsequently studied Pd/ZrO_2 to see whether this reference catalyst showed substantially different catalytic properties. To facilitate the comparison of the activities, the weight of Pd/ZrO_2 in the reactor was adjusted (to 30 mg) based on its loading (**Table 4.1-1**) so its overall quantity of Pd was identical to 60 mg of $\text{ZrO}_2@\text{Pd}/\text{SiO}_2$. Pd/ZrO_2 showed a higher conversion (**Figure 4.2.1b**), presumably because the Pd was better dispersed (89%, **Table 4.1-1**). This catalyst also had a similarly high CO selectivity (79%). Interestingly, the selectivity increased over time (to 91% at 20 h) while CH_4 selectivity also consistently went down (**Figure A.3.9b**). Although Pd/ZrO_2 seemed to have a slightly higher rate and selectivity compared to $\text{ZrO}_2@\text{Pd}/\text{SiO}_2$, this catalyst deactivated faster than the overcoated catalyst did.

Water is a product in RWGS and the presence of steam has been identified as a factor that accelerates catalyst deactivation.¹⁴² Furthermore, the reaction temperature (450 °C) was close to the Hüttig temperature of Pd (548 °C) (i.e. the temperature at which surface atoms become significantly mobile) and even higher than the Hüttig temperature of PdO (307 °C).¹⁴³ Under our harsh operating condition, the undercoordinated Pd atoms are assumed to be quite mobile. In gas phase reaction, particle sintering can result from both particle coalescence and Ostwald (atomic) ripening.¹⁴⁴ A recent study using a high-resolution microscope has shown that the under-coordinated Pd atoms on the particle surface possess high surface energy and are mobile.¹⁴⁵ Our XPS results indicated the overcoats can interact with Pd as an increased PdO signal was observed. Therefore, we speculated that the ZrO_2 overcoat could have capped undercoordinated Pd and thus limiting the mobility of these Pd atoms. Moreover, ZrO_2 could

have also served as a physical barrier that resulted in a longer diffusion path for the migrating particle to reach another particle, which delayed particle coalescence.

Finally, $\text{ZrO}_2@\text{Pd}/\text{ZrO}_2$ was also tested to investigate the effects of the overcoat when Pd was supported on ZrO_2 . With the same amount of Pd in the reactor (50 mg $\text{ZrO}_2@\text{Pd}/\text{ZrO}_2$), the conversion over $\text{ZrO}_2@\text{Pd}/\text{ZrO}_2$ was close to that of $\text{ZrO}_2@\text{Pd}/\text{SiO}_2$ but still lower than that of Pd/ZrO_2 . Intriguingly, this catalyst showed the highest initial CO selectivity (90%) and the selectivity quickly rose to 100% within 2 h (**Figure 4.2.1c**). No CH_4 was detected from 2 to 20 h time-on-stream (**Figure A.3.9c**). $\text{Cu}/\text{Al}_2\text{O}_3$ catalysts have been reported to have 100% selectivity towards CO at atmospheric pressure and they showed very little activity for methanation.^{53,146} However, when Cu supported on other metal oxides (ZrO_2 or TiO_2), it could produce methanol, which also makes the catalysts unselective. Noble metals like Pd usually has a higher rate (For instance, $\text{Pd}/\text{Al}_2\text{O}_3$ could achieve a similar rate at a lower temperature compared to $\text{Cu}/\text{Al}_2\text{O}_3$)^{134,146}, but they typically also catalyze methanation and then decreases CO selectivity. Attempts to inhibit the competing methanation over noble metal (e.g. Rh, Ru, and Ir) have been made, including controlling particle size and the porous environment.^{147–151} However, to the best of our knowledge, this is the first Pd-based catalyst reaching 100% CO selectivity. To demonstrate that Pd/ZrO_2 cannot reach 100% CO selectivity at the same conversion, we reduced the weight of Pd/ZrO_2 (to 10 mg) to have the same conversion as the overcoated catalyst (dash line in **Figure 4.2.1b**). A slightly increased initial selectivity was observed (89%) but the selectivity fluctuated around 90% throughout the test. Although this result emphasized the unique catalytic property of $\text{ZrO}_2@\text{Pd}/\text{ZrO}_2$, it also indicated that the selectivity was dependent on conversion. Therefore, we similarly varied the conversion of $\text{ZrO}_2@\text{Pd}/\text{ZrO}_2$ by reducing the catalyst's weight (to 17 mg) in the reactor. Interestingly, the initial selectivity of $\text{ZrO}_2@\text{Pd}/\text{ZrO}_2$ remained the same (around 90%) at 24% of conversion and $\text{ZrO}_2@\text{Pd}/\text{ZrO}_2$ still reached almost 100% CO selectivity with additional time-on-stream.

Moreover, similar to what we have observed when studying $\text{ZrO}_2@\text{Pd}/\text{SiO}_2$, $\text{ZrO}_2@\text{Pd}/\text{ZrO}_2$ also deactivated less quickly compared to Pd/ZrO_2 . $\text{ZrO}_2@\text{Pd}/\text{ZrO}_2$ did deactivate in the early stage but the conversion remained quite stable after 10 h. In contrast, Pd/ZrO_2 continuously deactivated throughout the catalytic run. Based on these results, we concluded that not only could the ZrO_2 overcoat create a new ZrO_2 -Pd interface and result in an exceptional CO selectivity, but it also mitigated the deactivation at harsh reaction conditions (450 °C with the presence of steam).

To study the deactivation mechanism, CO_2 hydrogenation was run using $\text{ZrO}_2@\text{Pd}/\text{SiO}_2$, Pd/ZrO_2 and $\text{ZrO}_2@\text{Pd}/\text{ZrO}_2$ on a Micromeritics Autochem, which allows us to perform CO chemisorption directly on spent catalysts. The reaction was run for 48 h, reduced again at 300 °C with a flow of H_2 , and after which the spent catalysts were titrated using CO pulses. To verify whether carbon deposition also occurred, a second CO chemisorption was performed after calcining the spent catalysts for 1 h. The first CO titration showed that the $\text{Pd}_{\text{surface}}$ on the three spent catalysts were reduced after 48 h reaction. The quantity of detected $\text{Pd}_{\text{surface}}$ decreased according to: $\text{ZrO}_2@\text{Pd}/\text{SiO}_2 > \text{ZrO}_2@\text{Pd}/\text{ZrO}_2 > \text{Pd}/\text{ZrO}_2$ (**Figure 4.2.1d**), which agreed with the observed deactivation rates in the catalysis tests. Interestingly, all spent catalysts showed increased $\text{Pd}_{\text{surface}}$ after calcination, which indicated the presence of carbonaceous deposits on the spent catalysts. After removing the deposits by calcination, Pd/ZrO_2 still lost the largest amount of $\text{Pd}_{\text{surface}}$ (from 47.3 to 1.2 μmol). Sintered Pd particles were also observed when analyzing the spent Pd/ZrO_2 by microscopy (**Figure A.3.10**) These results confirmed that the catalysts with a ZrO_2 overcoat were more resistant to sintering under harsh reaction conditions. The $\text{ZrO}_2@\text{Pd}/\text{ZrO}_2$ catalyst recovered the greatest quantity of $\text{Pd}_{\text{surface}}$ (from 0.8 to 5 μmol) among the three spent catalysts. In contrast, calcination had less effect on Pd/ZrO_2 and $\text{ZrO}_2@\text{Pd}/\text{SiO}_2$, which implied that more carbonaceous deposits were formed on $\text{ZrO}_2@\text{Pd}/\text{ZrO}_2$. Based on the deactivation study, we

believed that catalyst deactivation was caused by both sintering and carbon deposition. The larger amount of deposits formed over $\text{ZrO}_2@\text{Pd}/\text{ZrO}_2$ was particularly interesting, since the rise of CO selectivity accompanied the initial deactivation (the deactivation slowed down after CO selectivity reached 100%). This selectivity change was unlikely caused by particle sintering because most of literature reports that smaller Pd particles are more selective RWGS catalysts. Additionally, if Pd with a specific size could lead 100% CO selectivity, the same phenomenon would have been observed on Pd/ZrO_2 once the Pd agglomerates had formed. The rise of selectivity towards CO due dynamic changes of catalysts during CO_2 hydrogenation has been previously reported including due to self-poisoning on Ru/CeO_2 and the transformation of methanation sites on Rh/TiO_2 .^{147,152} The switch from methanation to RWGS sites resulted from the encapsulation of Rh by a thin reducible metal oxide overcoat due to strong metal support interactions. Since ZrO_2 is a non-reducible metal oxide and the Pd has been overcoated, the occurrence of active site transformation is less likely. Therefore, we propose that the carbon deposited on methanation sites of the $\text{ZrO}_2@\text{Pd}/\text{ZrO}_2$ catalyst allowed the reaction to reach 100% CO selectivity.

4.3 *In-situ* characterization and reaction mechanism

To further investigate the superior selectivity of $\text{ZrO}_2@\text{Pd}/\text{ZrO}_2$ and the reaction mechanism, *in-situ* DRIFTS was carried out to identify reaction intermediates (**Figure 4.3.1**). The catalysts were reduced with a flow of H_2 at 300 °C and then the feed was switched to He. Subsequently the temperature was elevated to 450 °C and the spectrum was recorded (black lines in **Figure 4.3.1**). Subsequently, the He flow was switched into a mixture of CO_2 and H_2 and another spectrum was obtained (green lines in **Figure 4.3.1**). $\text{ZrO}_2@\text{Pd}/\text{SiO}_2$, $\text{ZrO}_2@\text{Pd}/\text{ZrO}_2$ and Pd/ZrO_2 displayed similar spectra before flowing CO_2 and H_2 . The two

small bands at 1539 and 1449 cm^{-1} were assigned to the bending modes of strongly bound H_2O .¹⁵³ These two bands were not observed on g-Pd/SiO₂, suggesting that most of adsorbed water had been removed during reduction, which was likely due to the weaker interaction between SiO₂ and H₂O. The reaction intermediates were studied after feeding CO₂ and H₂. Surprisingly, only Pd@ZrO₂ showed new absorbance bands whereas g-Pd/SiO₂, ZrO₂@Pd/SiO₂, ZrO₂@Pd/ZrO₂ displayed similar spectra under reaction condition as they did in the presence of He. By analogy with past reports, the emerging bands on Pd/ZrO₂ were assigned to bicarbonate-derived species.^{137,154,155} Therefore, we inferred that CO₂ was converted via the bicarbonate-mediated RWGS pathway on Pd/ZrO₂. In contrast, the other three catalysts might activate CO₂ through direct C-O cleavage pathway because no absorbance associated with either formate or bicarbonate was observed.^{149,156} The intensity of the water bands decreased when CO₂ and H₂ were present. Strongly bound water was reported to be associated with zirconium centers having oxygen vacancies.¹⁵³ The desorption of water might result from the competitive chemisorbed CO₂ or other reaction intermediates and such observation is consistent with a hypothesis suggesting that oxygen vacancy is critical for CO₂ activation.¹⁵⁷

The bicarbonate-mediated mechanism on Pd/ZrO₂ is similar to a reported mechanism on an analogous Pd/Al₂O₃ system (**Figure 4.3.2a**).¹³⁷ The first step is the chemisorption of CO₂, presumably on the zirconium center with O-vacancies according to our DRIFTS measurements. The chemisorbed CO₂ then either interacted with surface hydroxyl groups or dissociated H to form bicarbonate-like intermediates. The intermediates subsequently converted into chemisorbed CO. This step is especially influential on CO and CH₄ selectivities, where CO can be either linearly chemisorbed on an isolated Pd atom (k_1) or on Pd atoms with bridge configuration (k_2). The linearly adsorbed CO has a lower desorption barrier, thus eventually forming the CO product whereas the bridge bound CO can be more prone to further

hydrogenation into CH_4 .¹³⁷ Therefore, methanation and RWGS have been thought to be occurring on two different sites and reducing the nanoparticles' size can favor the production of CO because of the larger fraction of isolated metal sites.^{137,147,149–151} Although we were unable to detect chemisorbed CO using our DRIFTS setup, likely due to the catalysts' low loadings and insufficient detection sensitivity, a high CO selectivity was indeed obtained from highly dispersed Pd/ZrO₂, which was in agreement with mechanisms described in literature. Another intriguing observation on Pd/ZrO₂ was the aforementioned increased CH₄ selectivity at higher conversion. This phenomenon can also be explained by the competing RWGS and methanation reactions. The equilibrium conversion of RWGS under our condition was calculated as 43%.¹⁵⁸ Therefore, the production of CO was close to the thermodynamic controlled equilibrium at high conversion (solid line, **Figure 4.2.1b**). At such conditions, any excess amount of catalyst would not produce more CO and just contribute to methanation. Once Pd/ZrO₂ deactivated, the RWGS reaction was no longer thermodynamically controlled, which led to less pronounced methanation and CO selectivity increased back to 90% (similar to that obtained at lower conversion, dashed line, **Figure 4.2.1c**).

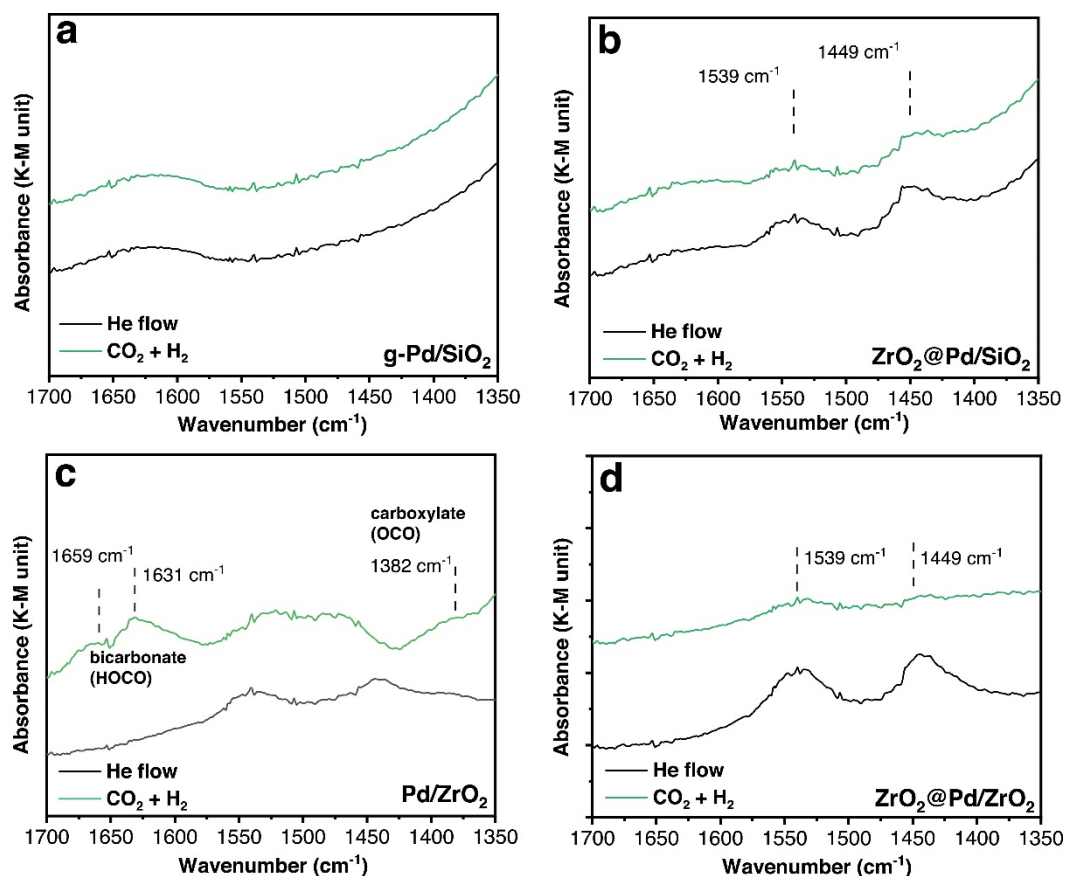


Figure 4.3.1 *In-situ* DRIFTS spectra in the presence of He and then CO₂ and H₂ for (a) g-Pd/SiO₂ (b) ZrO₂@Pd/SiO₂ (c) Pd/ZrO₂ and (d) ZrO₂@Pd/ZrO₂.

As previously mentioned, we did not observe any IR signals representing formate and bicarbonate intermediate when analyzing the catalysts with ZrO₂ overcoat. Because so far there are only three possible mechanisms of CO₂ hydrogenation that have been proposed (bicarbonate, formate, and C-O cleavage pathways), we hypothesized that CO₂ was likely converted through the C-O cleavage route on ZrO₂@Pd/ZrO₂ and ZrO₂@Pd/SiO₂. Our previous XPS results have shown a significant rise of Pd²⁺ character in the catalysts with a ZrO₂ overcoat, which implied the formation of ZrO₂-Pd interface. Therefore, we attributed the switch of reaction pathways to the presence of this newly engineered interfacial site. Similar to the aforementioned bicarbonate-mediated pathway, CO₂ could be initially chemisorbing on O-vacancies. According to DFT calculation, the subsequent C-O bond cleavage involves the

reaction of dissociated O (from CO₂) and H (from H₂, adsorbed on Pd).¹³³ Therefore, the CO₂ dissociation step presumably occurred on the new ZrO₂-Pd interface and then formed a CO intermediate (**Figure 4.3.2b**). A recent theoretical study suggested that the adsorbed CO can either desorb (k_1) or further dissociate (k_2).¹⁴⁹ Accordingly, the energy barriers of CO dissociation and desorption are two key factors controlling CO and CH₄ selectivities. DFT also suggested that the intermediates of methanation proposed here might differ from those in bicarbonate-mediated route, where the adsorbed CO was assumed to be hydrogenated several times to form CH₄ and H₂O.¹³³ In the direct C-O cleavage pathway, the chemisorbed CO might be undergoing a second C-O cleavage, forming *C and *O and CH₄ forms from the hydrogenation of *C. Based on our CO chemisorption results of spent catalyst (**Figure 4.2.1d**), we hypothesized that besides being hydrogenated to CH₄, the adsorbed carbon could also nucleate on the surface leading to carbonaceous deposits, poisoning methanation site. This hypothesis might explain the self-poisoning phenomenon observed by Aitbekova et al. and us.¹⁴⁷ On the ZrO₂-Pd interface, a small fraction of the CO intermediate that adsorbed on the sites favoring C-O cleavage was initially converted into CH₄ (at 10% selectivity in our initial measurement). However, carbon deposition likely occurred on the same active sites, which quickly poisoned methanation (causing a quick initial deactivation) and subsequently the selectivity towards CO rose to 100%. Interestingly, the original support of Pd seemed to play a crucial role because this self-poisoning effect was less discernible (CH₄ selectivity only slightly increased by 4%) when using ZrO₂@Pd/SiO₂. This difference could be explained by the sensitivity of these sub-nanometer metal clusters to their local coordination environment, which is observed in the literature.¹⁵⁹ As a result, Pd clusters coordinated with pure ZrO₂ could have shown a different reactivity that facilitates carbon deposition. Further elucidation of the factors governing the self-poisoning of methanation sites will likely require more theoretical

and analytical investigations including DFT simulations and more advanced *in-situ* spectroscopies (e.g. near-ambient pressure X-ray photoelectron spectroscopy).¹⁶⁰

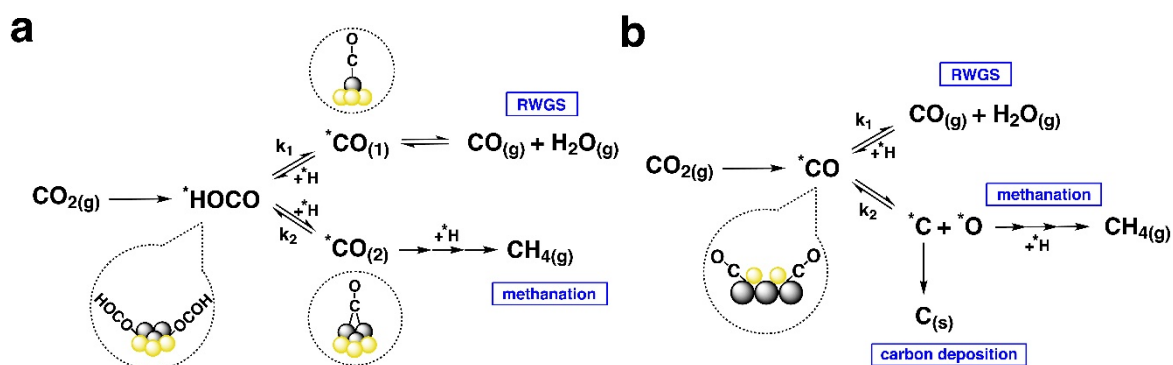


Figure 4.3.2 Proposed reaction networks of (a) Pd/ZrO₂, (b) ZrO₂@Pd/ZrO₂ and ZrO₂@Pd/SiO₂. The yellow and grey spheres denote ZrO₂ and Pd, respectively.

4.4 Summary of Chapter 4

A novel sol-gel based synthetic strategy was developed to prepare an atomically dispersed Pd(en)₂/SiO₂ that was compatible with sol-gel overcoating. Coating this material with various metal oxide, prior to reduction, could tailor metal oxide-Pd interface sites and provide highly accessible metal on the final catalyst. In contrast to the traditional method where Pd particles had been formed on SiO₂ prior to coating, this new synthetic approach could limit particle growth during thermal activations, resulting in highly accessible sub-nanometer Pd clusters. Because of the formation of new metal oxide-metal interfaces, both ZrO₂@Pd/SiO₂ and Al₂O₃@Pd/SiO₂ showed significant improved activity for CO₂ hydrogenation compared to the uncoated g-Pd/SiO₂. Moreover, this strategy could be applied to additional metal oxide supports to synthesize catalysts with distinct catalytic properties. Specifically, when using Pd(en)₂/ZrO₂ to synthesize a ZrO₂@Pd/ZrO₂ catalyst, the overcoat not only mitigated the

agglomeration of Pd under the severe reaction condition but also increased the CO₂ selectivity. This improvement was attributed to self-poisoning of the methanation sites by carbon deposition, which was exclusively favorable to the ZrO₂@Pd/ZrO₂ catalyst, leading to an unprecedented 100% CO selectivity on Pd after 1 h time-on-stream.

4.5 Experimental section of Chapter 4

Chemicals and Materials

All chemicals and materials were analytical grade and obtained from commercial suppliers. They were used without further purification unless stated otherwise. Air and moisture-sensitive reagents were handled in a N₂ filled glove box and a standard Schlenk line apparatus. SiO₂ (AEROSIL® 200) was obtained from Evonik. ZrO₂ (1/8" Pellets) was obtained from Alfa Aesar. The pellets were crushed to a powder using a mortar and pestle. Al₂O₃ (Pural SB) was obtained from Sasol. All metal oxides were calcined at 500 °C for 5 h prior to use. Zr(O^tBu)₄ (80% in butanol) was obtained from Fluka. Molecular sieves (4 Å), HCl (ca. 37%) and Al(O^sBu)₃ were obtained from Merck. Ethanol was obtained from Fisher Scientific. NH_{3(aq)} (ca. 25%) and toluene were obtained from VWR Chemicals. Toluene was dried by adding fresh toluene into a degassed, nitrogen filled flask containing molecular sieves (pre-activated at 120 °C under vacuum). [3-(2-Aminoethylamino)propyl] trimethoxysilane, palladium(II) bis(acetylacetonate) [Pd(acac)₂], ethyl acetoacetate, potassium bromide (KBr) and HNO₃ (ca. 68%) were obtained from Sigma-Aldrich. The water used in this study was purified by a Millipore Milli-Q Advantage A10 water purification system until its resistivity was higher than 18 MΩ cm. All gases were purchased from Carbagas.

Synthesis of atomically pre-catalysts

72 mg (used to target a 0.5 wt% loading) of palladium(II) bis(acetylacetonate) was dissolved in 10 mL of dried toluene. 104 mg of [3-(2-Aminoethylamino)propyl]trimethoxysilane was added and then the yellow solution became lighter. The mixture was stirred for 1 h under nitrogen flow. Meanwhile, 5 g of SiO₂ was dispersed in 100 mL dried toluene by ultra-sonicating the mixture for 30 min. After sonication, the silane complex was injected into the SiO₂ suspension and the mixture was refluxed at 80 °C for 15 h. The crude Pd(en)₂/SiO₂ was then separated by centrifugation and washed three times with ethanol and then water. Finally, the powder was dried in a vacuum oven at 45 °C for 24 h. Pd(en)₂/ZrO₂ was synthesized using the same procedure except the amount of ZrO₂ was 1.5 g and the quantity of toluene used for dispersing ZrO₂ was 40 mL. The quantities of Pd precursor and silane were adjusted accordingly to target a loading of 0.5wt%.

Synthesis of reference catalysts

Pd/ZrO₂ and Pd/Al₂O₃ were prepared using the wet impregnation method. Typically, 29 mg of Pd(acac)₂ was dissolved in 20 mL toluene and mixed with 2 g of the metal oxide support. The mixture was first ultra-sonicated for 30 min and then stirred for 30 min. The toluene was first removed using a rotary evaporator and the powder was further dried in an oven at 120 °C overnight. The dried impregnated powder was calcined at 300 °C for 3 h with a flow of synthetic air and then reduced at 300 °C for 3 h with a flow of hydrogen. The reference g-Pd/SiO₂ was prepared by calcining and reducing the Pd(en)₂/SiO₂ at the same conditions as those described above.

Synthesis of the overcoated catalysts

Prior to the coating procedure, the quantity of the metal alkoxides that was necessary to achieve a monolayer-equivalent of coverage was estimated by dividing BET surface area of

the substrate by the Van Der Waals projection area of $\text{Zr}(\text{O}^t\text{Bu})_4$ or $\text{Al}(\text{O}^s\text{Bu})_3$ (1.2 nm^2 and 1 nm^2 respectively, estimated by MarvinSketch), similar to what has been described in Chapter 2 and 3.^{74,120}

Synthesis of $\text{ZrO}_2@\text{Pd}/\text{SiO}_2$ and $\text{ZrO}_2@\text{Pd}/\text{ZrO}_2$

1 g of $\text{Pd}(\text{en})_2/\text{SiO}_2$ ($S_{\text{BET}} = 160 \text{ m}^2/\text{g}$) was dispersed in a mixture of 40 mL ethanol, 2 mL H_2O and 0.04 mL NH_3 (25%). The zirconia precursor (used for 20 monolayer-equivalents of coverage) was prepared by mixing calculated amounts of EAA and $\text{Zr}(\text{O}^t\text{Bu})_4$ (1.15 g and 1.7 g, respectively; the molar ratio of EAA and $\text{Zr}(\text{O}^t\text{Bu})_4$ was 2) and the final precursor volume was fixed to 10 mL by adding ethanol. The precursor was stirred for 1 h and injected into the $\text{Pd}(\text{en})_2/\text{SiO}_2$ suspension at a rate of 1 mL/h using a KDS 100 legacy syringe pump. The reaction mixture was left stirring for 6 h after the injection was complete. The product was separated using centrifugation and washed three times first with ethanol and then with water. An excess quantity of ammonia was added to the supernatant and neither precipitation nor gelation was observed, suggesting most of the ZrO_2 precursor had reacted. The product was calcined and reduced with the same procedure as for the reference catalysts. $\text{ZrO}_2@\text{Pd}/\text{ZrO}_2$ was synthesized with the same procedure except $\text{Pd}(\text{en})_2/\text{ZrO}_2$ ($S_{\text{BET}} = 65 \text{ m}^2/\text{g}$) was used. Because of its smaller surface area, the amounts of EAA and $\text{Zr}(\text{O}^t\text{Bu})_4$ were adjusted to 0.47 g and 0.7 g, respectively.

Synthesis of $\text{Al}_2\text{O}_3@\text{Pd}/\text{SiO}_2$

1 g of $\text{Pd}(\text{en})_2/\text{SiO}_2$ ($S_{\text{BET}} = 160 \text{ m}^2/\text{g}$) was dispersed in a mixture of 40 mL ethanol, 1 mL H_2O and 0.02 mL NH_3 (25%). The alumina precursor (used for 20 monolayer-equivalents of coverage) was prepared by mixing calculated amounts of EAA and $\text{Al}(\text{O}^s\text{Bu})_3$ (1.3 g and 0.5 g, respectively; the molar ratio of EAA and $\text{Al}(\text{O}^s\text{Bu})_3$ was 0.75) and the final precursor volume

was fixed to 10 mL by adding ethanol. The injection, purification and thermal treatment steps were the same as those used in the synthesis of $\text{ZrO}_2@\text{Pd}/\text{SiO}_2$.

CO₂ hydrogenation study

CO₂ hydrogenation was performed using a fixed-bed tubular quartz reactor with an inner diameter 6 mm. Typically, a known quantity of catalyst (typically 50 mg unless otherwise stated) was immobilized between two quartz wool plugs. Prior to the reaction, the catalyst was reduced with 25% H₂/Ar flow (60 mL/min) at 300 °C for 1 h. After reduction, the gas flow was switched to pure Ar and the reactor temperature was ramped to 450 °C. Subsequently, a gas mixture containing 5% CO₂ and 15% H₂ in Ar (total flow rate = 60 mL/min and H₂/CO₂ = 3) was fed into the reactor. The reaction was performed at atmospheric pressure and the product stream was monitored using an on-line MATRIX-MG01 FTIR spectrometer (Bruker) equipped with OPUS-GA software and a 10 cm gas cell heated at 120 °C. The measurements were free from both external and internal mass transfer limitations, which were verified using Mears and Weisz-Prater criteria, respectively (section A.3.3). The presented results were calculated as shown below.

$$\text{Conversion} = \frac{CO_2(t_0) - CO_2(t)}{CO_2(t_0)}$$

$$\text{Rate} = \frac{CO_2(t_0) - CO_2(t)}{Pd_{total}}$$

$$\text{Selectivity}_{CO} = \frac{CO(t)}{CO_2(t_0) - CO_2(t)} ; \text{Selectivity}_{CH_4} = \frac{CH_4(t)}{CO_2(t_0) - CO_2(t)}$$

Material characterizations

Physisorption, NH₃-TPD, TEM, STEM, XRD and XPS were performed using the same methods and instruments described in section 2.8. The Pd_{surface} atoms were quantified on a

Micromeritics AutoChem II 2920 using a pulse chemisorption method with CO as a probe molecule. Prior to CO chemisorption, the sample was reduced at 300 °C for 30 min with 10% H₂ flow in Ar (50 mL/min). Subsequently, the sample was cooled down to 50 °C, a pulse of 5% CO in He was injected, during which a thermal conductivity signal was recorded. The injection was repeated until the peak area of thermal conductivity signal remained nearly constant, which indicated that the saturation of surface Pd had taken place. The Pd_{surface} was finally quantified using the areas of the thermal conductivity signal and assuming the stoichiometric ratio between Pd and CO to be 1. The catalyst stability study was performed on the same AutoChem II 2920 instrument. In this case, the catalyst was reduced at 300 °C for 30 min with 10% H₂ flow in Ar (50 mL/min). The temperature was then ramped up to 450 °C under He flow (50 mL/min) and then the gas was switched to reactant stream (20% H₂ and 7% CO₂, with the remainder being He, 60 mL/min). The H₂ and CO₂ flow was maintained for 48 h and, then, a first chemisorption was performed with the same procedure described above. A second chemisorption was performed after calcining the sample at 400 °C under 50% synthetic air in He (50 mL/min) for 1 h in order to remove carbonaceous deposits.

DRIFTS were performed on a PerkinElmer Frontier spectrometer equipped with a mercury cadmium telluride detector and Praying Mantis™ accessories. The presented spectra were an average of 32 scans with a resolution of 4 cm⁻¹. The spectra of SiO₂ and Pd(en)₂/SiO₂ were recorded after removing physisorbed water at 200 °C under vacuum for 2 h. For the *in-situ* CO₂ hydrogenation measurements, the catalysts were mixed with equal amount of KBr using a mortar and pestle. The catalyst was reduced with pure H₂ flow (20 mL/min) at 300 °C for 30 min prior to the reaction. The reaction cell was cooled down and then the H₂ flow was switched to a He flow (60 mL/min). The temperature was then elevated to 450 °C and CO₂ hydrogenation was carried out by from He flow to a mixture of CO₂ and H₂ streams (20 and 60 mL/min, respectively).

Conclusions and Outlook

This thesis tackles the issues that arose from the emerging challenges associated with sustainable catalysis and does so by exploring opportunities in catalyst design with metal oxide deposition. I demonstrated that sol-gel based overcoating methods are not necessarily restricted to oxides with precursors that have slow kinetics such as SiO_2 or TiO_2 once the kinetics of precursors are controlled by either non-hydrolytic sol-gel techniques or coordination chemistry. Similar to ALD processes, the sol-gel methods could form a uniform overcoat over $\text{Cu}/\text{Al}_2\text{O}_3$, which significantly improved the thermal stability of Cu. Specifically, the initial activity of $\text{Al}_2\text{O}_3@\text{Cu}/\text{Al}_2\text{O}_3$ for furfural hydrogenation could be fully recovered after several catalyst regenerations whereas the high temperature of the regeneration steps caused particle sintering and continuously deactivated uncoated $\text{Cu}/\text{Al}_2\text{O}_3$. Another benefit of sol-gel deposition is that the physical properties of overcoat could be easily controlled using different precursors and reaction routes. In particular, using a less bulky Al_2O_3 precursor and non-hydrolytic sol-gel chemistry results in a denser overcoat, creating a highly active $\text{Pd}-\text{Al}_2\text{O}_3$ interface for hydrodeoxygenating lignin monomers.

In addition to improving the stability and selectivity of supported metal catalysts, sol-gel coatings could also be used to synthesize more thermally stable solid acids, especially when the material's acidity was dependent on its crystal structure. Depositing Nb_2O_5 on SBA-15 lead to a high-surface-area mesoporous niobia catalyst. Notably, the Si-O-Nb linkage of overcoated catalyst appeared to restrain the crystallization of niobia, thus maintaining its acidity during high temperature catalyst regeneration. The optimal ratio of Brønsted and Lewis acid sites of $\text{Nb}_2\text{O}_5@\text{SBA-15}$ increased the selectivity towards furfural by 10% during xylose dehydration. More interestingly, $\text{Nb}_2\text{O}_5@\text{SBA-15}$ was more active for catalytic alkylation than a commercial Nb_2O_5 that had stronger acidity. The higher activity was attributed to its

mesoporous structure, which inhibits the formation of hydrophilic hydrogen bond networks composed of surface hydroxyls and thus favored the adsorption of hydrophobic reactants.

Lastly, I showed that the atom efficiency of overcoated catalyst can be considerably improved by introducing a supported molecular metal complex into the synthetic procedures. Thanks to the protective overcoat and ligands, a sintering resistant Pd catalyst with nearly the same metal dispersion as the uncoated catalyst could be produced after calcining and reducing the overcoated materials with Pd(en)₂ complex. With ZrO₂ deposition, the Pd-ZrO₂ interface of Pd/ZrO₂ could be engineered into an inverted ZrO₂-Pd interface and this new interfacial site achieves 100% CO selectivity during CO₂ hydrogenation.

Overall, the improved catalyst stability and selectivity seen in a wide range of catalytic reactions coupled with the simplicity of sol-gel methods described in this thesis, could greatly expand the application scope of catalyst overcoating. The sol-gel based procedures developed here open new avenues to synthesize more robust heterogeneous catalysts using simple apparatuses (laboratory glassware). We envisioned that the reinforcement provided by overcoats could particularly benefit heterogeneous catalysts used in sustainable processes. Chapter 3 showed that the overcoated catalyst had a greater resistance against phase transformation. It has been known that phase transformation can have deleterious effects on not only acidity but also on catalyst surface area. A possible future application of overcoating methods could be designing more stable catalysts for valorizing bio-refined molecules with high oxygen content. Valorization in aqueous phase would be especially environmentally and industrially favorable since such bio-refined feedstocks are often produced in the presence of water, sometimes by fermentation. The overcoat could maintain the surface area of catalysts in such hydrothermal conditions and therefore increase catalysts' life times.

Furthermore, the synthesis of supported metal complexes using ethylenediamine that can then be transformed to highly dispersed and active catalysts (Chapter 4) could be extended to other group 10 metals besides Pd. I also believe that supported complexes comprising metals in other groups could be developed with different coordination chemistry. In this regard, combining various catalytic materials with sol-gel overcoating would enable us to create a broad array of highly dispersed metals with engineered metal oxide-metal interfaces, which could give new impetus to the development of more active and selective catalysts for the reactions catalyzed by interfacial sites. Finally, solution-based synthesis allows us to incorporate organic templates in overcoating procedures for tailoring unique nanostructures, since some soft templates rely on self-assembly in liquid phase in order to form specific morphologies. The template might enable area-selective metal oxide deposition and removing the template by thermal treatment could create a targeted cavity as a nanoreactor. Such cavity might allow us to control the alignment of substrate molecules, leading to a transition-state selectivity. With the control over the substrate orientation the active interfacial sites formed by metal oxide overcoat, selective cleavage or transformation of desired functional groups might be realized, which is invaluable for upgrading highly functional oxygenate molecules found in biomass feedstocks. The long-term goal of catalyst overcoating is to rationally design porous structure and active site to achieve regioselectivity or even enantioselectivity of other reactions beyond renewable catalysis. As such, I believe the immense versatility and applicability of overcoating technique could have a great impact in catalysis field in the future.

List of Figures in Appendix

Figure A.1.1 TEM images of (a) C-5Al ₂ O ₃ @SBA-15 and (b) C-5Al ₂ O ₃ @SBA-15 prepared using an excess concentration of ammonia.....	101
Figure A.1.2 (a) Pore size distribution and (b) small angle XRD analyses of Pt based catalysts and C-5Al ₂ O ₃ @SBA-15.	101
Figure A.1.3 TEM and STEM images of (a) α -Fe ₂ O ₃ ellipsoid, (b) C-Al ₂ O ₃ @ α -Fe ₂ O ₃ , (c) carbon sphere and (d) C-Al ₂ O ₃ @carbon sphere.	102
Figure A.1.4 Uncontrolled alumina deposition on Pt/SBA-15.....	103
Figure A.1.5 Physisorption of C9nm-Al ₂ O ₃ @SiO ₂ and N-Al ₂ O ₃ @SiO ₂	103
Figure A.1.6 Furfural hydrogenation of overcoated Cu/Al ₂ O ₃ synthesized by the reported method.....	104
Figure A.1.7 TEM images and particle size distribution (insets) of spent (a) C-Al ₂ O ₃ @Cu/Al ₂ O ₃ and (b) Cu/Al ₂ O ₃ after furfural hydrogenation.	104
Figure A.1.8 HDO results of N-Al ₂ O ₃ @2%Pt/SBA-15 at high conversion.....	105
Figure A.1.9 XRD of supported Pt catalysts in the high angle range.....	105
Figure A.1.10 FTIR spectra of the OH stretching band of catalysts with and without alumina overcoat.....	106
Figure A.1.11 ¹ H ssNMR spectra of SBA-15 and Pt catalysts.	106
Figure A.1.12 Pyridine-DRIFT analyses of (a) Pt/Al ₂ O ₃ , (b) N-Al ₂ O ₃ @2%Pt/SBA-15 and (c) C-Al ₂ O ₃ @2%Pt/SBA-15.	107
Figure A.2.1 Microscope images of 2Nb ₂ O ₅ @SBA-15 under (a) regular TEM bright field and (b) STEM HAADF mode with EDX mapping of (c) Nb and (d) Si.....	113
Figure A.2.2 Microscope images of 3Nb ₂ O ₅ @SBA-15 under (a) regular TEM bright field and (b) STEM HAADF mode with EDX mapping of (c) Nb and (d) Si.....	114
Figure A.2.3 Microscope images of 4Nb ₂ O ₅ @SBA-15 under (a) regular TEM bright field and (b) STEM HAADF mode with EDX mapping of (c) Nb and (d) Si.....	115
Figure A.2.4 XRD analyses of (a) bulk niobia and overcoated catalysts and, (b) HY-340 and 4Nb ₂ O ₅ @SBA-15 after three catalyst regenerations.	116

Figure A.2.5 FTIR spectra of dried uncoated and overcoated SBA-15 in the OH region.....	116
Figure A.2.6 ^1H ssNMR spectra of SBA-15, $4\text{Nb}_2\text{O}_5@\text{SBA-15}$ and HY-340.....	117
Figure A.2.7 DRIFT-Pyridine spectra of overcoated and bulk niobia catalysts.....	117
Figure A.2.8 Spent $4\text{Nb}_2\text{O}_5@\text{SBA-15}$ (a) at 84% and (b) at 100% conversion.....	118
Figure A.2.9 Ammonia TPD result for (a) $4\text{Nb}_2\text{O}_5@\text{SBA-15}$ and (b) HY-340.....	118
Figure A.3.1 Picture of as-synthesis $\text{Pd}(\text{en})_2/\text{SiO}_2$	123
Figure A.3.2 FTIR spectra of pristine SiO_2 and $\text{Pd}(\text{en})_2/\text{SiO}_2$	123
Figure A.3.3 (a) STEM and (b) TEM images of $\text{ZrO}_2@\text{Pd}/\text{SiO}_2$	124
Figure A.3.4 N_2 Physisorption results of Pd catalysts with (a) SiO_2 and (b) ZrO_2 support...	124
Figure A.3.5 XPS results of (a) Pd/ZrO_2 (b) $\text{ZrO}_2@\text{Pd}/\text{SiO}_2$ and (c) $\text{ZrO}_2@\text{Pd}/\text{ZrO}_2$	125
Figure A.3.6 (a) Conversion, CO selectivity and (b) CH_4 selectivities of g-Pd/ SiO_2	125
Figure A.3.7 (a) Conversion, CO selectivity and (b) CH_4 selectivity of $\text{Pd}/\text{Al}_2\text{O}_3$. (c) Conversion, CO selectivity and (d) CH_4 selectivity of $\text{Al}_2\text{O}_3@\text{Pd}/\text{SiO}_2$	126
Figure A.3.8 NH_3 -TPD results of $\text{Al}_2\text{O}_3@\text{Pd}/\text{SiO}_2$ (red) and $\text{Pd}/\text{Al}_2\text{O}_3$ (black).....	126
Figure A.3.9 CH_4 selectivities of (a) $\text{ZrO}_2@\text{Pd}/\text{SiO}_2$, (b) Pd/ZrO_2 and (c) $\text{ZrO}_2@\text{Pd}/\text{ZrO}_2$.	127
Figure A.3.10 STEM analyses of spent Pd/ZrO_2 (a) under HAADF mode and (b) with EDX mapping as well as spend $\text{ZrO}_2@\text{Pd}@\text{ZrO}_2$ (c) under HAADF mode and (d) with EDX mapping.....	127

List of Tables in Appendix

Table A.1-1 Physical properties of solvent of FF hydrogenation and HDO	109
Table A.1-2 Physical properties of solute of FF hydrogenation and HDO	110
Table A.1-3 Summary of Weisz-Prater criterion.....	112
Table A.2-1 Physical properties of solute and HY-340.....	121
Table A.2-2 Summary of Weisz-Prater criterion.....	122

Appendix

A.1 Supplementary information of Chapter 2

A.1.1 Supporting figure and table

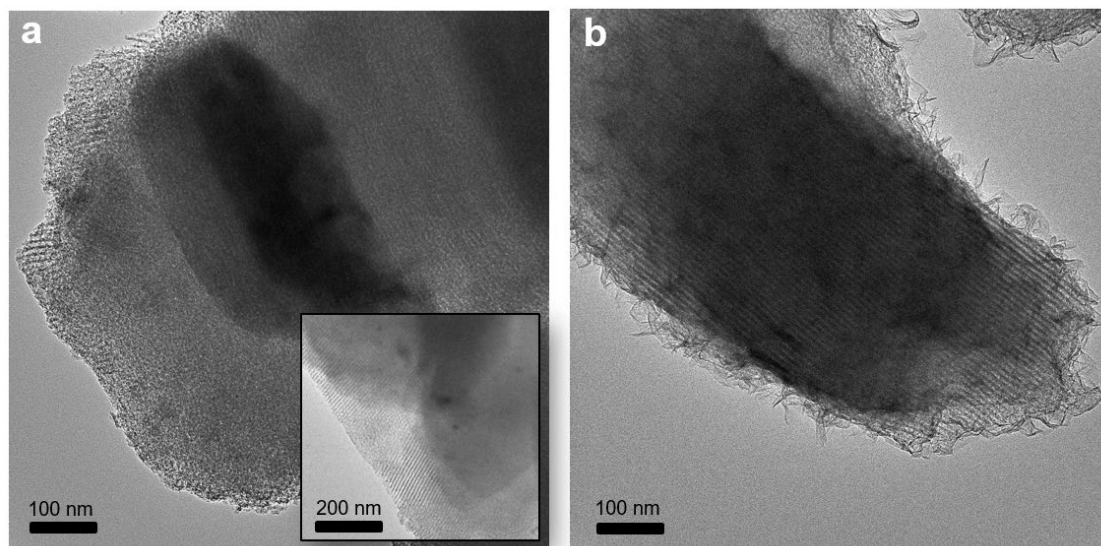


Figure A.1.1 TEM images of (a) C-5Al₂O₃@SBA-15, (with a comparison to uncoated 2%Pt/SBA-15, inset) and (b) C-5Al₂O₃@SBA-15 prepared using an excess concentration of ammonia (0.04 mL).

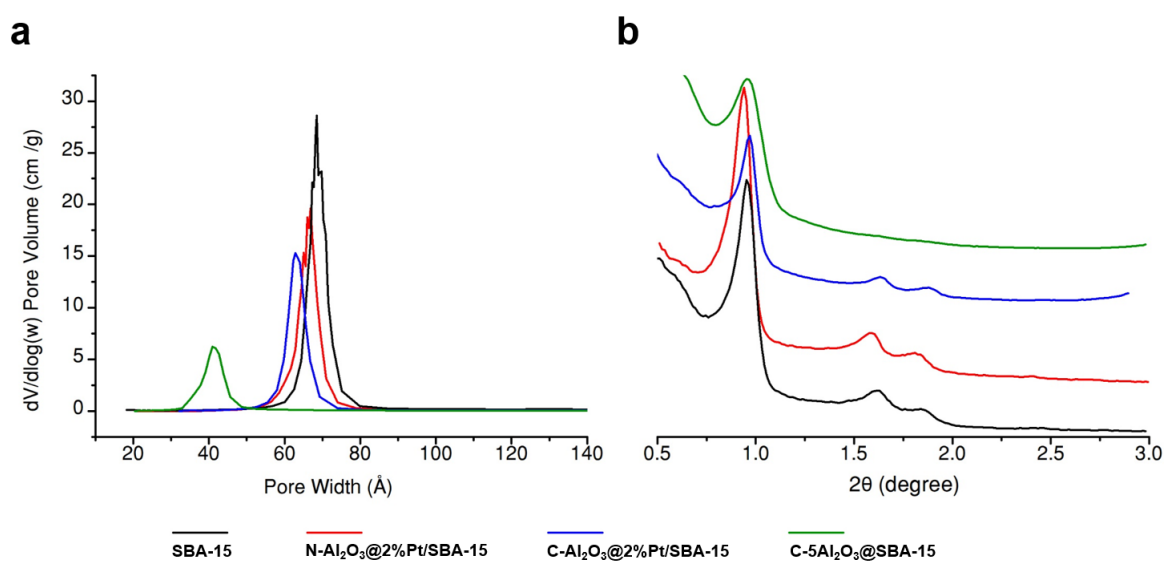


Figure A.1.2 (a) Pore size distribution and (b) small angle XRD analyses of Pt based catalysts and C-5Al₂O₃@SBA-15.

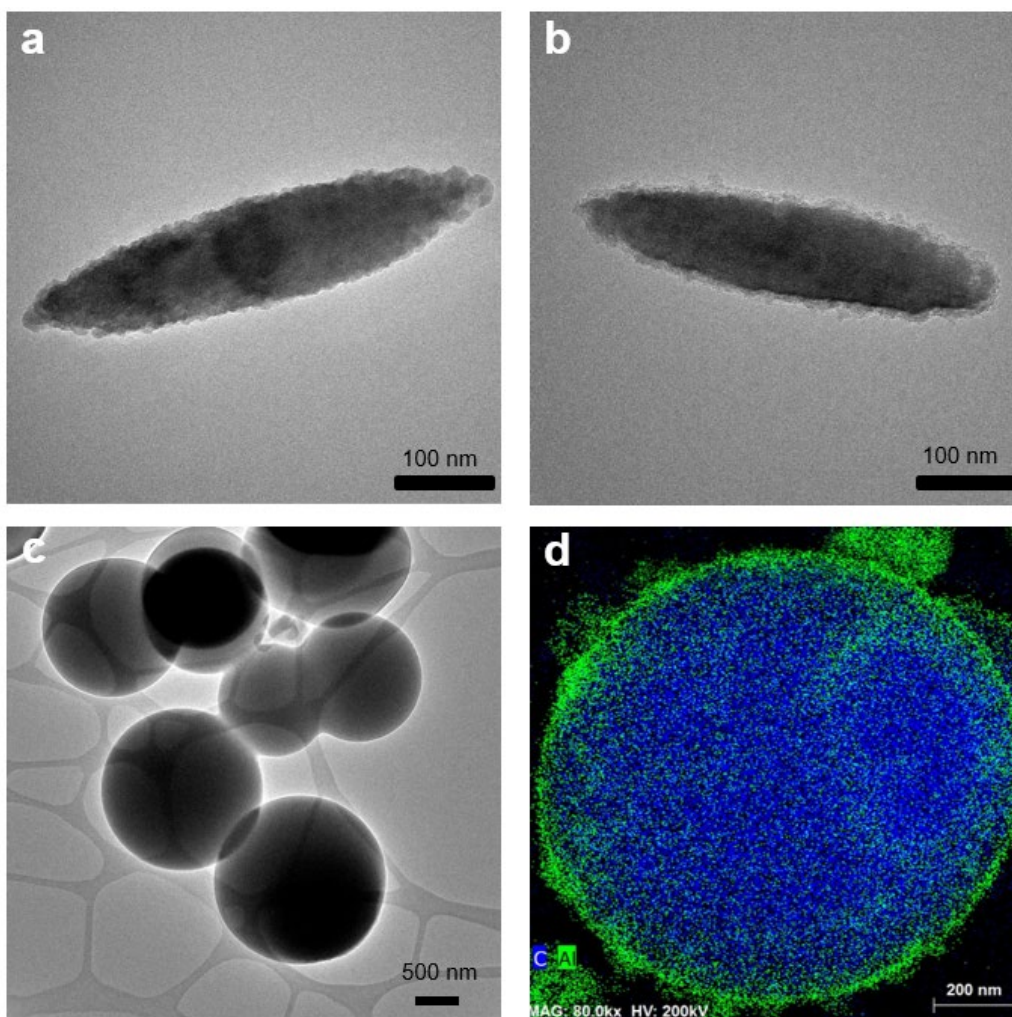


Figure A.1.3 TEM and STEM images of (a) $\alpha\text{-Fe}_2\text{O}_3$ ellipsoid, (b) $\text{C-Al}_2\text{O}_3@\alpha\text{-Fe}_2\text{O}_3$, (c) carbon sphere and (d) $\text{C-Al}_2\text{O}_3@\text{carbon sphere}$.

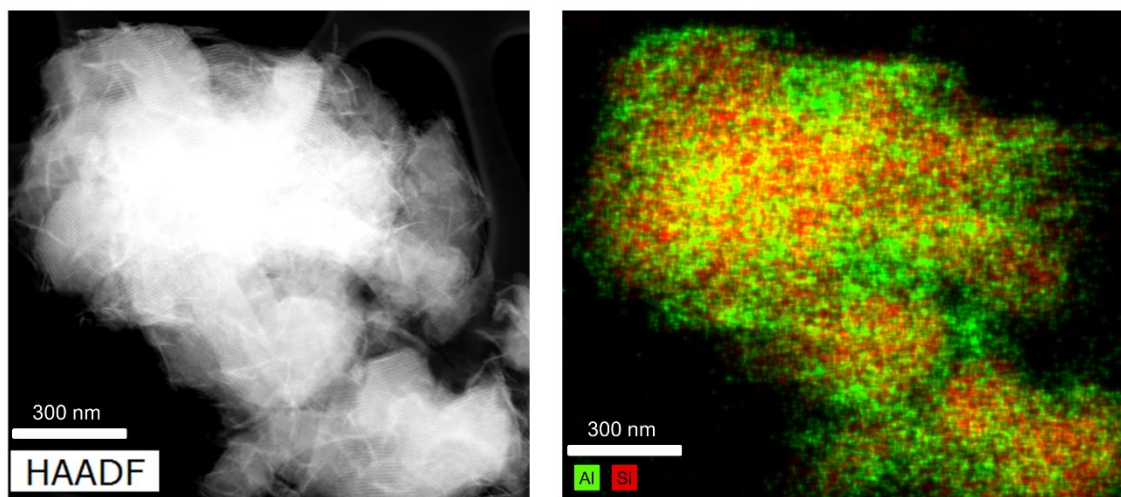


Figure A.1.4 Uncontrolled alumina deposition on 2%Pt/SBA-15 by injecting the mixture of $\text{Al}(\text{}^{\text{t}}\text{BuO})_3$ and AlBr_3 with an excessive concentration.

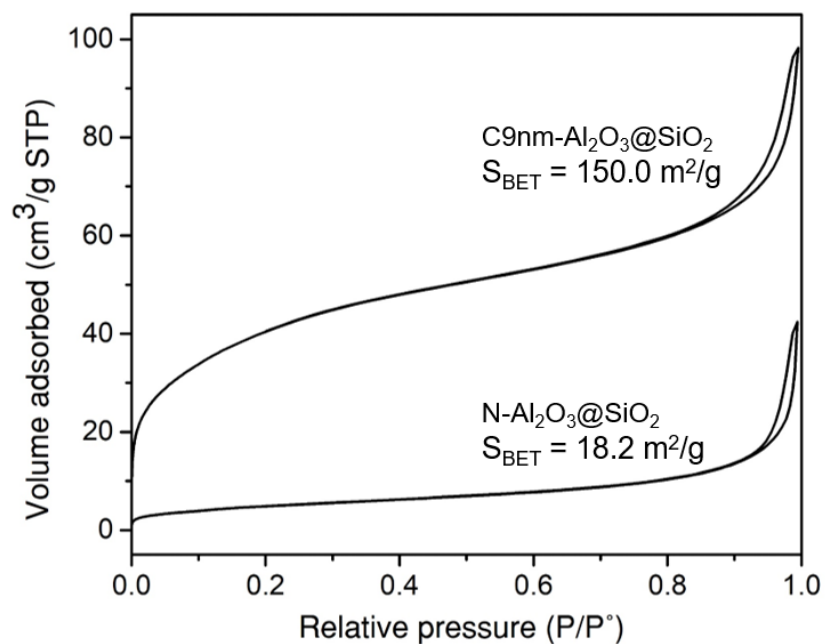


Figure A.1.5 Physisorption of $\text{C9nm-Al}_2\text{O}_3@\text{SiO}_2$ and $\text{N-Al}_2\text{O}_3@\text{SiO}_2$.

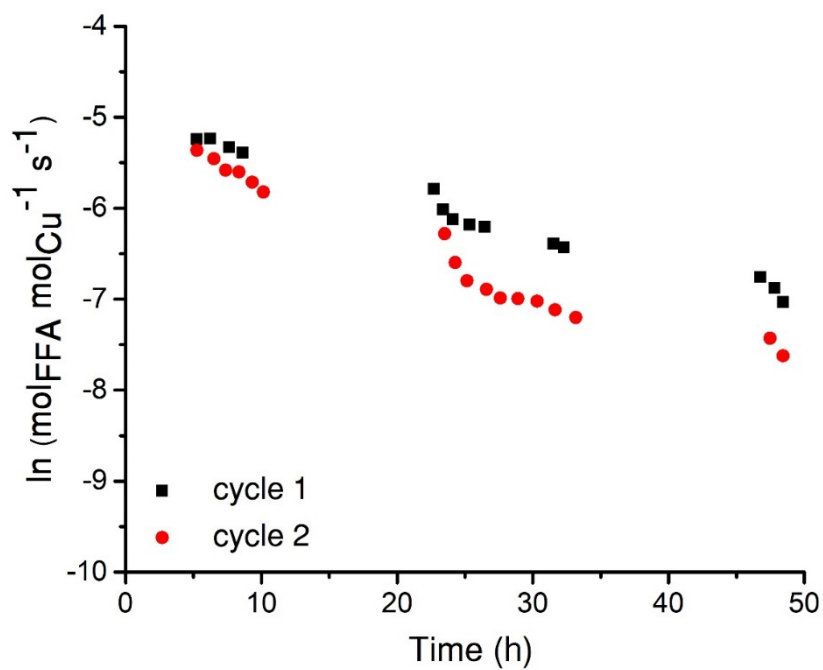


Figure A.1.6 Furfural hydrogenation of overcoated Cu/Al₂O₃ synthesized by the reported method.⁷ The catalyst began to deactivate after the second cycles, suggesting the formation of non-uniform overcoat.

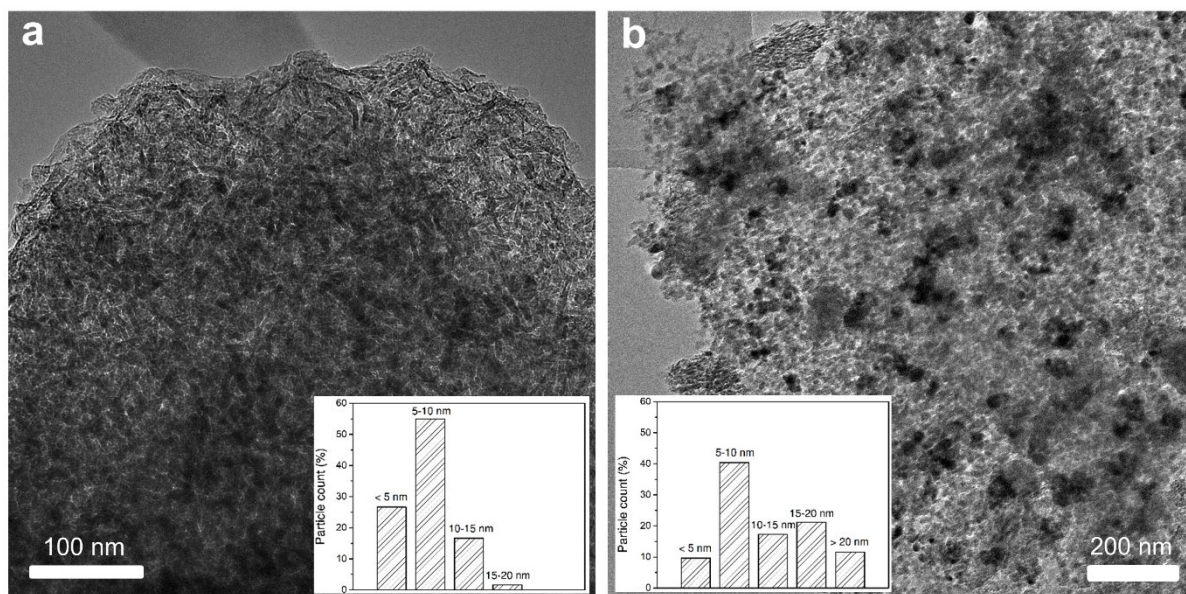


Figure A.1.7 TEM images and particle size distribution (insets) of spent (a) C-Al₂O₃@Cu/Al₂O₃ and (b) Cu/Al₂O₃ after furfural hydrogenation.

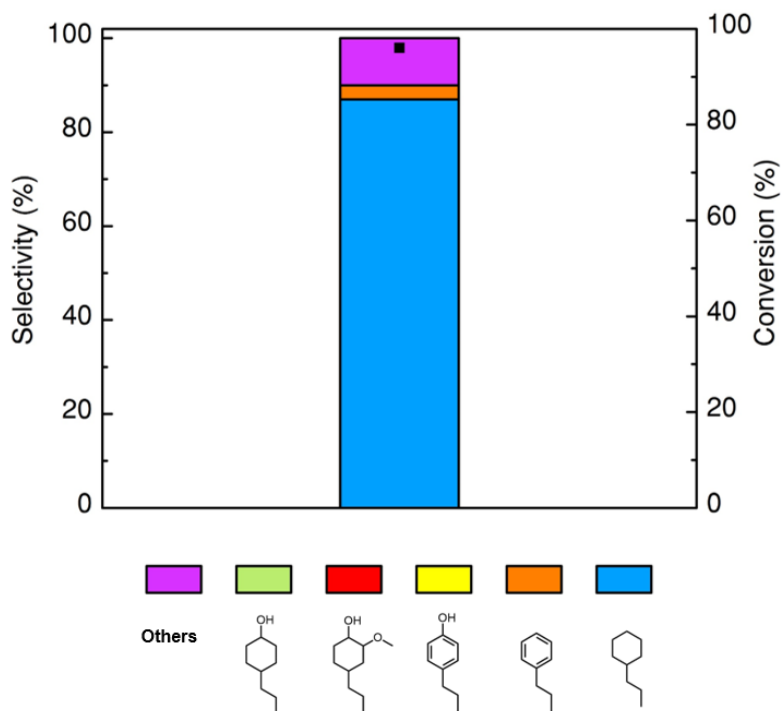


Figure A.1.8 HDO results of N-Al₂O₃@2%Pt/SBA-15 at high conversion. Condition: 30 mg catalyst, 0.1 mL 4-propylguaiacol in 10.5 mL isooctane, 200 °C, 15 bar H₂, 3 h.

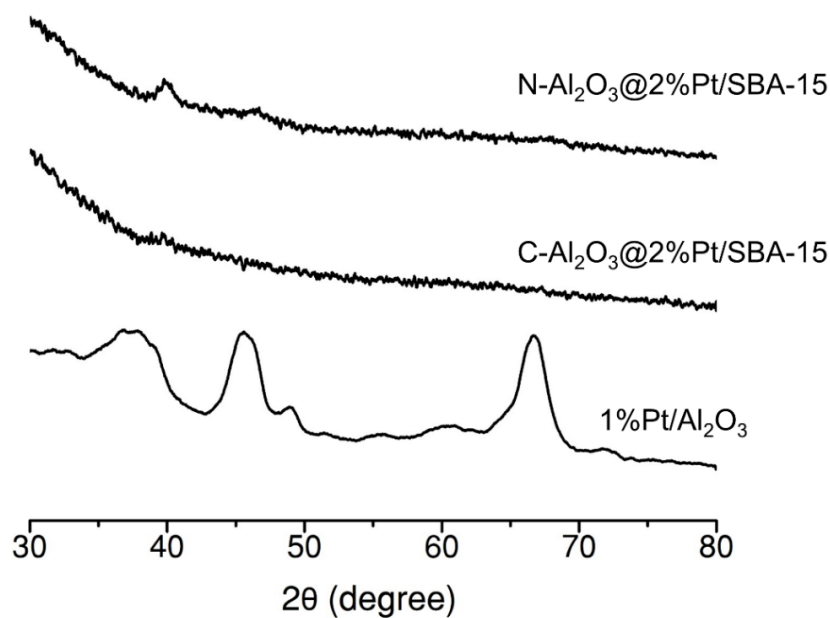


Figure A.1.9 XRD of supported Pt catalysts in the large angle range.

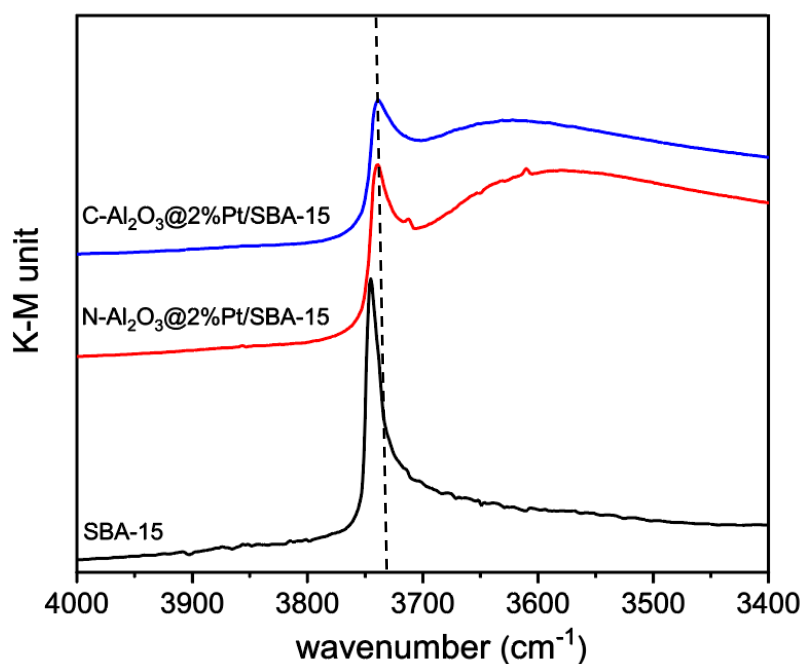


Figure A.1.10 FTIR spectra at the OH stretching area. The shift of sharp OH band suggested the formation of Al-OH group.^{81,161} Furthermore, a broad band at 3600 cm^{-1} that was found in both overcoated catalysts likely resulted from the bridged Al-OH-Si formed on the support-overcoat interface.¹⁶²

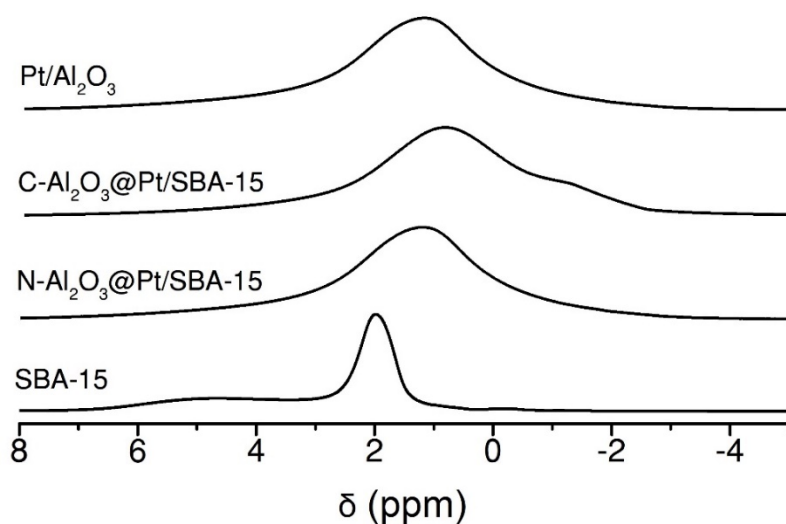


Figure A.1.11 ^1H ssNMR spectra of SBA-15 and Pt catalysts. The broadening of proton signals of overcoated catalyst and $\text{Pt}/\text{Al}_2\text{O}_3$ resulted from the presence of multiple types of Al-OH and strong dipole-dipole interactions between the protons of adjacent hydroxyl groups or physisorbed water.^{163,164}

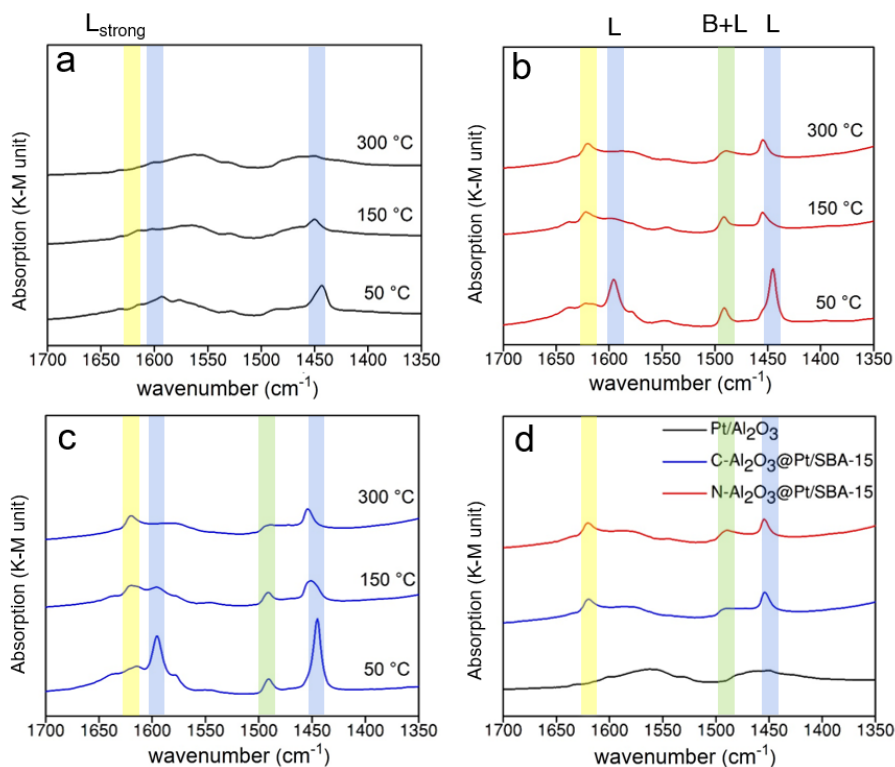


Figure A.1.12 Pyridine-DRIFTS analyses of (a) Pt/Al₂O₃, (b) N-Al₂O₃@2%Pt/SBA-15 and (c) C-Al₂O₃@2%Pt/SBA-15. The comparison of the three catalysts at 300 °C is shown in (d). The bands at around 1450 and 1600 cm⁻¹ (blue) were characteristic of a typical Lewis acid site. The band at 1625 cm⁻¹ is assigned as pyridine reacting with strong Lewis acid sites (yellow) and they were only found in the overcoated catalysts. The band at 1490 cm⁻¹ could result from Lewis acid or Brønsted acid sites (green). Given the absence of the band indicative of Brønsted acidity at 1545 cm⁻¹, we concluded that Brønsted acid sites are not present in these samples.^{165–167}

A.1.2 Mass transfer effects on reaction

Mass transfer effects were assessed using the Weisz-Prater criterion:

$$\frac{r_{obs} (R_p)^2}{D_{TA}^e C_{AS}} < 1$$

Where:

r_{obs} is the observed reaction rate per unit volume of catalyst ($\text{mol}\cdot\text{s}^{-1}\cdot\text{cm}^{-3}$)

R_p is the spherical particles radius (cm)

D_{TA}^e is the effective transition diffusivity ($\text{cm}^2\cdot\text{s}^{-1}$)

C_{AS} is the concentration at the surface of the catalyst particle ($\text{mol}\cdot\text{cm}^{-3}$)

Reaction rates were obtained experimentally using the rate obtained using uncoated catalyst, which had higher reaction rates than overcoated samples. The particle radius can be estimated by TEM. The concentration at the surface of the catalyst pellet (C_{AS}) was assumed to be the same as the bulk concentration because of the fast stirring rate (600 rpm) for HDO and flow conditions for FF hydrogenation. Bulk diffusivities of furfural in 1-butanol and 4-propylguaiaicol in isooctane, were calculated using the Wilke-Chang equation:¹⁶⁸

$$D_{AB} = 7.4 \times 10^{-8} \frac{T}{\mu}$$

Table A.1-1 Physical properties of solvent of FF hydrogenation and HDO

Parameter	Description	Unit	Values	
			FF hydrogenation	HDO
T	absolute temperature	K	403	473
x	association parameter	-	1	1
M _B	molecular weight of the solvent	G·mol ⁻¹	74	114.2
μ	dynamic viscosity of the solvent	cP or mPas	0.36	0.47
V _A	molar volume at boiling point	cm ³ ·mol ⁻¹	90	182
D _{AB}	bulk diffusivity	cm ² ·s ⁻¹	4.8×10^{-5}	3.5×10^{-5}

Where solvents dynamic viscosities μ were obtained from the literature.^{169,170} In the absence of data at the reaction temperature, the dynamic viscosity at a lower temperature was used. This simplification leads to an underestimation of D_{AB}, and hence, an overestimation of the Weisz-Prater criterion, ensuring that no mass transfer issues are present.

Molar volume at the boiling point V_A was calculated using the method presented by Sastri *et al.*¹⁷¹ The size ratio of solute (λ) over the pore diameter was calculated.¹⁶⁸ This ratio was used to calculate the internal diffusivity within the pores of the catalyst particles with respect to that

of the bulk for liquid phase conditions. The physical properties of solvents were summarized in **Table A.1-1**.

$$\lambda = \frac{d_s}{d_p}$$

$$\frac{D_{AB,pore}}{D_{AB}} = (1 - \lambda)^4$$

The solute diameter was calculated using the MarvinSketch software. The average pore diameter of Cu/Al₂O₃ and 2%Pt/SBA-15 was determined by using the BJH adsorption analysis. The results are shown in **Table A.1-2**.

Table A.1-2 Physical properties of solute of FF hydrogenation and HDO

Parameter	Description	Unit	Values	
			FF hydrogenation	HDO
d_s	solute diameter	nm	0.45	0.5
d_p	pore diameter	nm	10	7
$\frac{D_{AB,pore}}{D_{AB}}$	variation of diffusivity	-	0.77	0.77
$D_{AB,pore}$	pore diffusivity	cm ² ·s ⁻¹	4×10^{-5}	2.6×10^{-5}

The effective diffusivity was then calculated using the porosity (ε) and the tortuosity (τ) as follows:

$$D_{TA}^e = D_{AB}^e = \frac{\varepsilon}{\tau} D_{AB,pore}$$

In the absence of experimental data, ε and τ can be estimated according to Davis et al.¹⁷² The ε is 0.5 and the τ is 4 for both reactions. The D_{TA}^e for HDO and FF hydrogenation were then calculated as 3.25×10^{-6} and 5×10^{-6} ($\text{cm}^2 \cdot \text{s}^{-1}$), respectively.

Weisz-Prater criterion was then estimated and summarized in **Table A.1-3**.

Table A.1-3 Summary of Weisz-Prater criterion

Parameter	Description	Unit	Values	
			FF hydrogenation	HDO
r_{obs}	observed rate of reaction	$\text{mol}\cdot\text{cm}^{-3}\cdot\text{s}^{-1}$	9.9×10^{-6}	2.3×10^{-5}
R_p	particle radius	cm	1×10^{-5}	6×10^{-5}
D_{TA}^e	Effective diffusivity	$\text{cm}^2\cdot\text{s}^{-1}$	5×10^{-6}	3.25×10^{-6}
C_{AS}	surface concentration	$\text{mol}\cdot\text{cm}^{-3}$	6.4×10^{-4}	5.9×10^{-5}
	Weisz-Prater criterion		3.1×10^{-5}	4.3×10^{-4}

Since the calculated criterions were systematically several orders of magnitude below unity, we concluded that the reactions we ran were free of internal diffusion limitation. Although the observed rates were not obtained from the experiment with low conversion (ideally <5%) and no external diffusion limitation we assumed for calculations, the very low values of the Weisz-Prater criterion (between 10^{-5} and 10^{-4}) suggest that these assumptions/simplifications are not going to change our conclusions.

A.2 Supplementary information of Chapter 3

A.2.1 Supporting figure and table

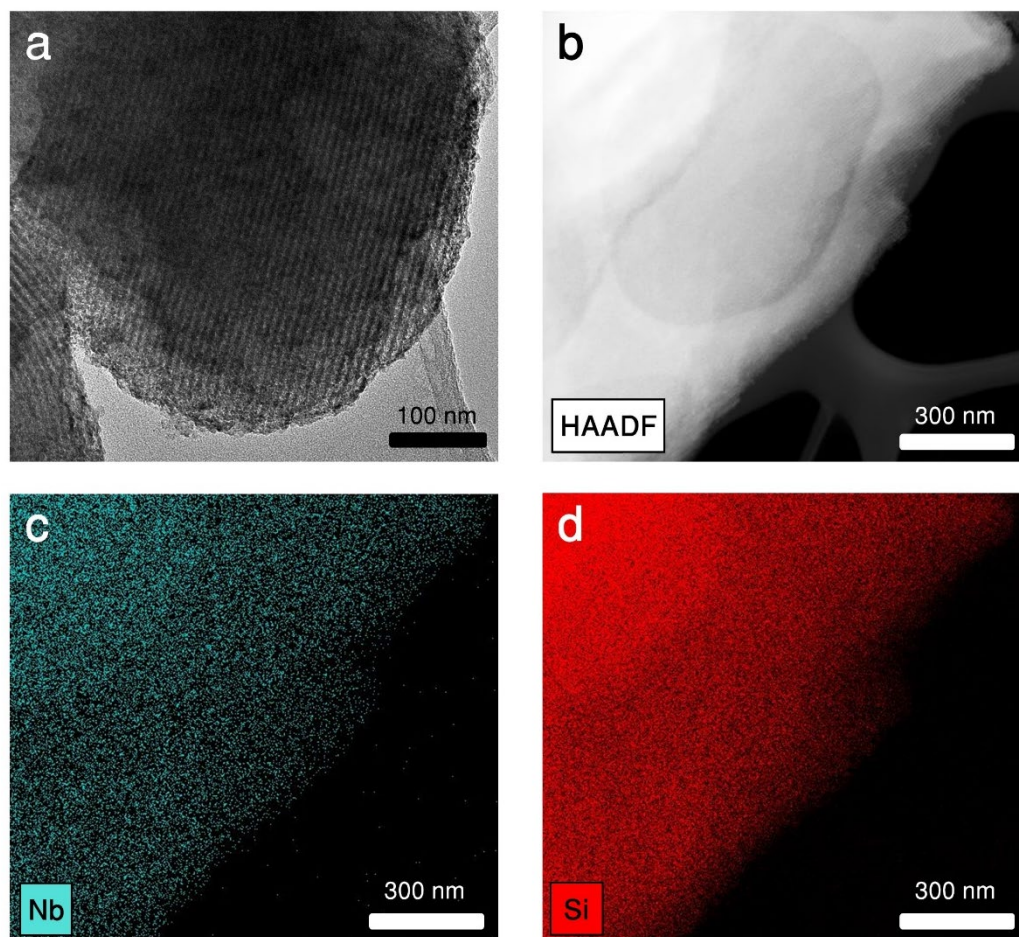


Figure A.2.1 Microscope images of $2\text{Nb}_2\text{O}_5@\text{SBA-15}$ under (a) regular TEM bright field and (b) STEM HAADF mode with EDX mapping of (c) Nb and (d) Si.

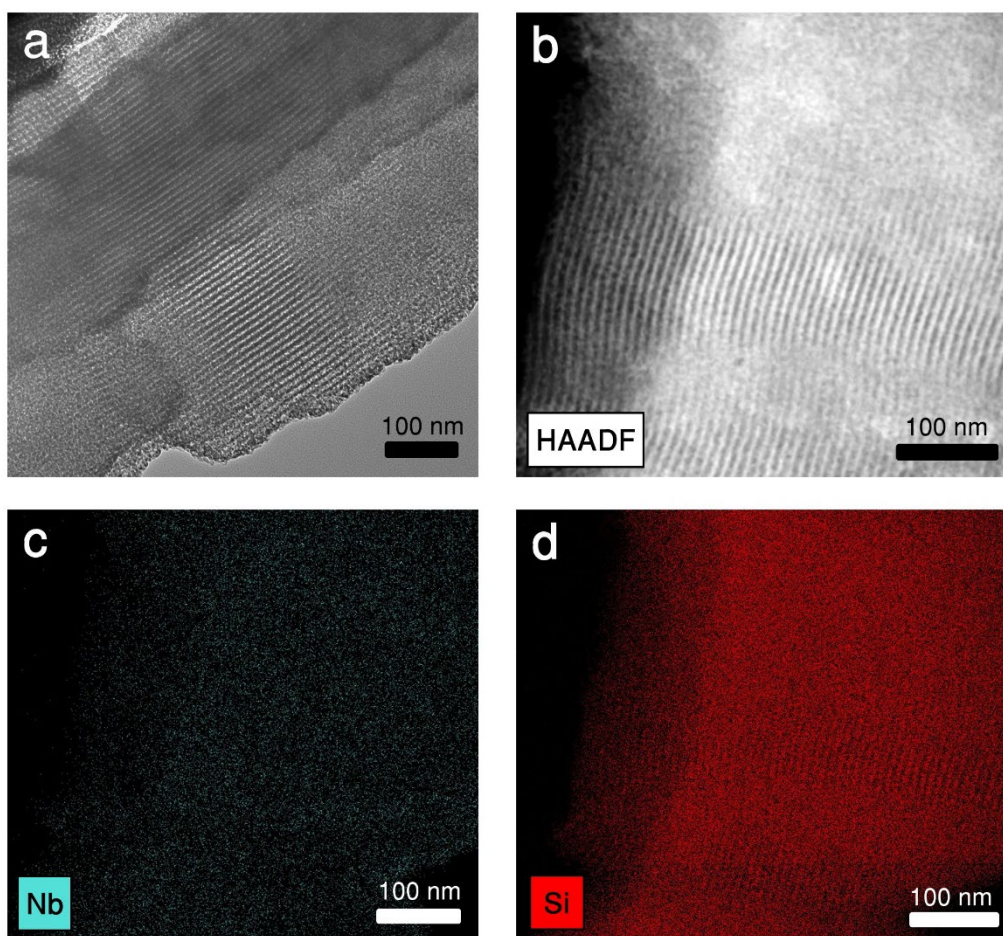


Figure A.2.2 Microscope images of $3\text{Nb}_2\text{O}_5@\text{SBA-15}$ under (a) regular TEM bright field and (b) STEM HAADF mode with EDX mapping of (c) Nb and (d) Si.

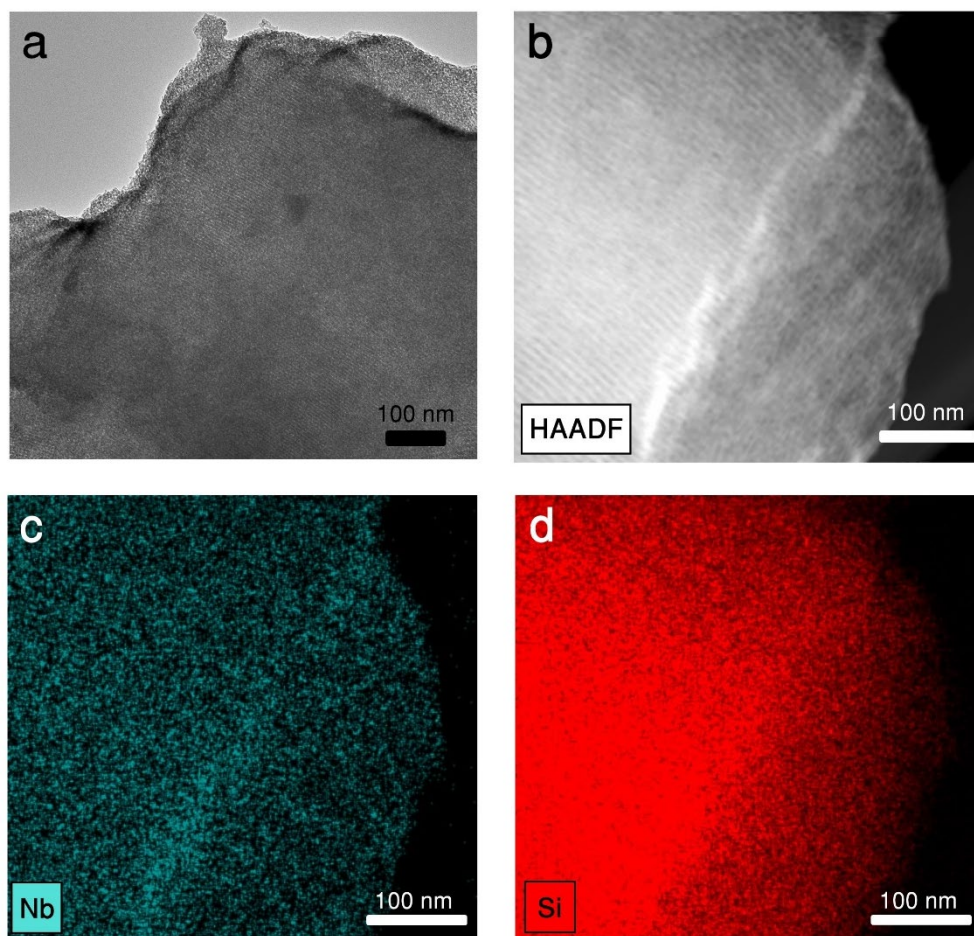


Figure A.2.3 Microscope images of $4\text{Nb}_2\text{O}_5@\text{SBA-15}$ under (a) regular TEM bright field and (b) STEM HAADF mode with EDX mapping of (c) Nb and (d) Si.

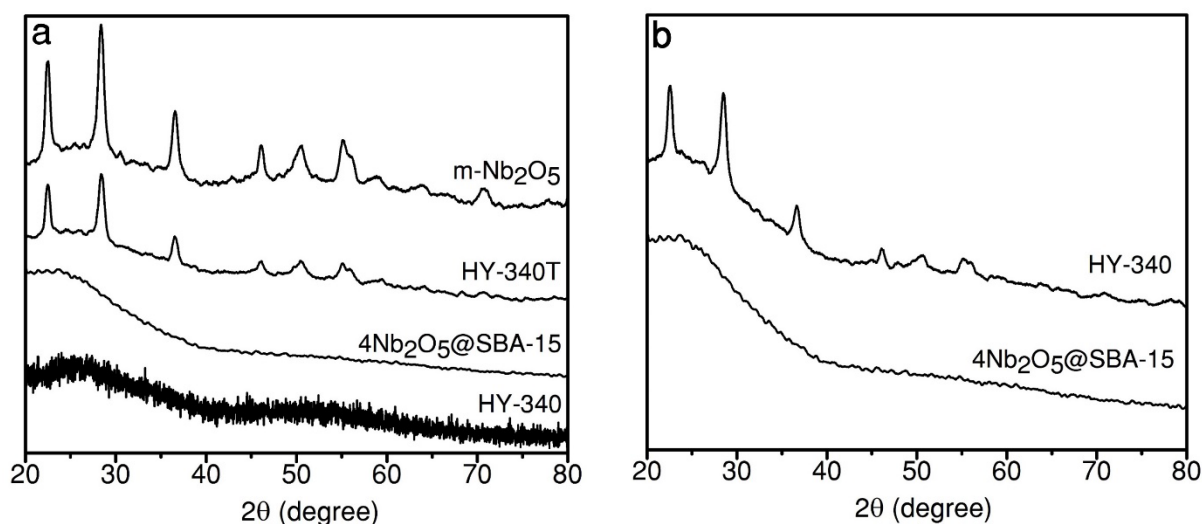


Figure A.2.4 XRD analyses of (a) bulk niobia and overcoated catalysts and, (b) HY-340 and $4\text{Nb}_2\text{O}_5@\text{SBA-15}$ after three catalyst regenerations. The crystal phases of $\text{m-Nb}_2\text{O}_5$, HY340T and regenerated HY-340 were identified as a pseudo-hexagonal phase in accordance with past reports.¹⁷³ All data were smoothed using the adjacent-averaging method with a 40 point window.

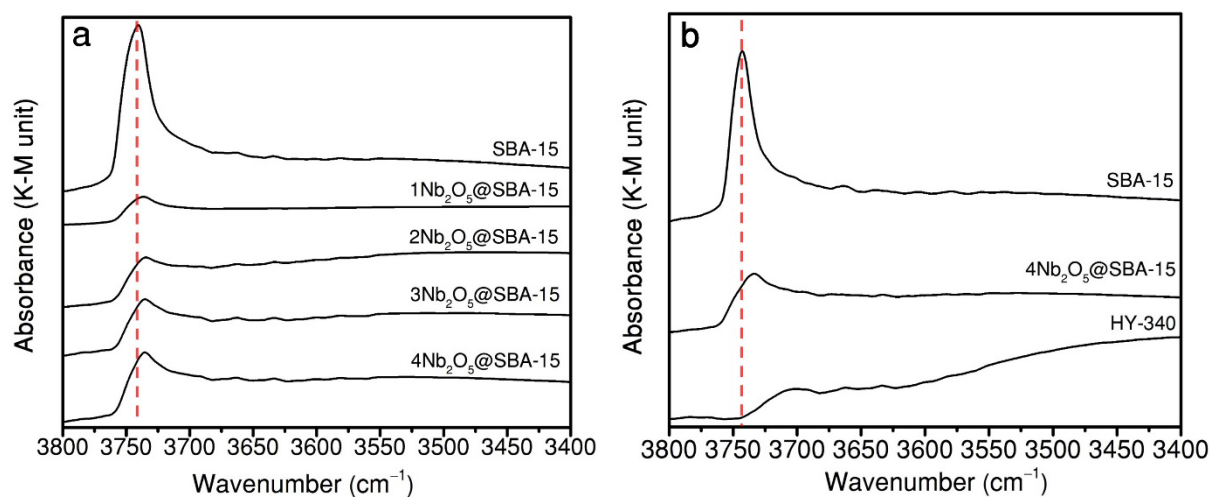


Figure A.2.5 (a) FTIR spectra of dried uncoated and overcoated SBA-15 in the OH region. SBA-15 displays a strong Si–OH stretching peak at 3745 cm^{-1} . A slight increase of intensity and redshift of this peak can be observed for overcoated samples because of the association with the Nb–OH band. This band can be seen in the FTIR spectra of (b) SBA-15, HY-340, and $4\text{Nb}_2\text{O}_5@\text{SBA-15}$. All the data were smoothed using the adjacent-averaging method with a 40-point window.

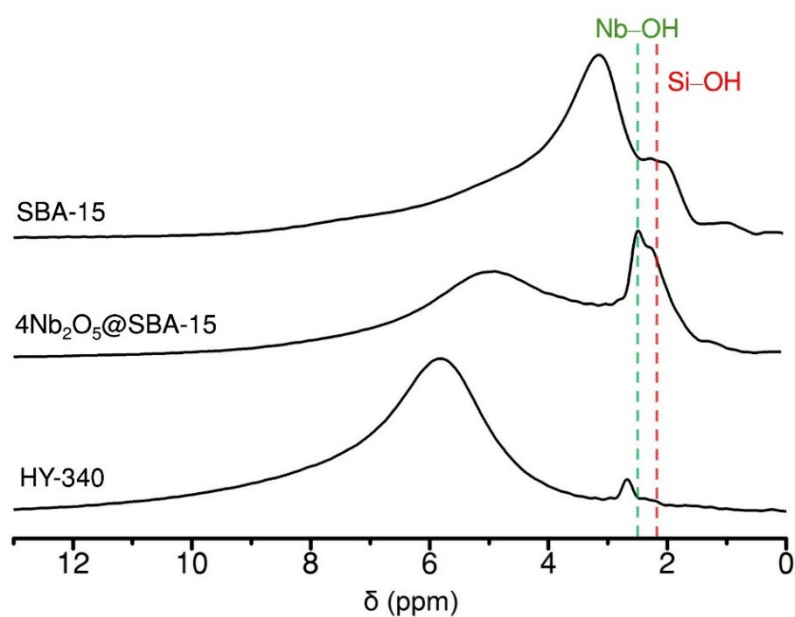


Figure A.2.6 ^1H ssNMR spectra of SBA-15, $4\text{Nb}_2\text{O}_5@\text{SBA-15}$ and HY-340. For SBA-15, the peak at 2.2 ppm was assigned to isolated silanols and the broad peak from 3 ppm to 8 ppm is attributed to strongly physisorbed water and hydrogen bonded silanols.¹⁷⁴ The isolated silanol peak can still be observed for $4\text{Nb}_2\text{O}_5@\text{SBA-15}$ and partially overlaps with a peak at 2.4 ppm, which was assigned to isolated Nb–OH.¹¹²

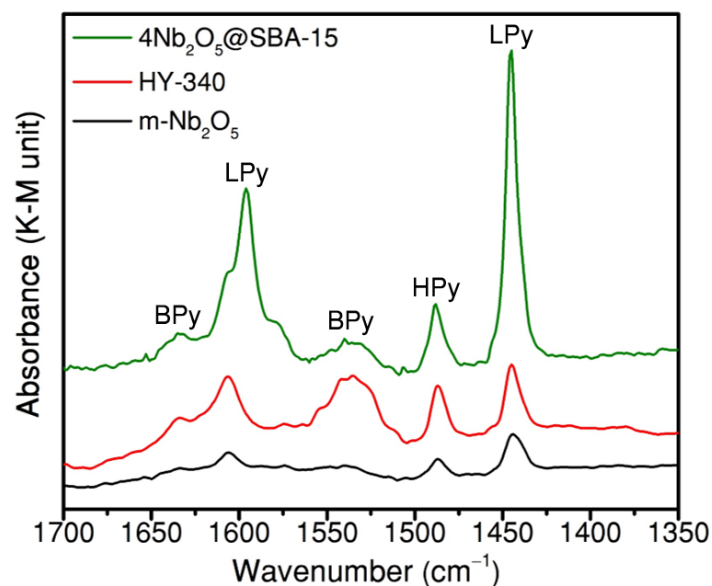


Figure A.2.7 DRIFTS-Pyridine spectra of overcoated and bulk niobia catalysts recorded at 50 °C. BPy, LPy and HPy denote pyridine adsorbing on Brønsted acid sites, pyridine adsorbing on Lewis acid site and H-bonded pyridine, respectively.¹⁰⁹

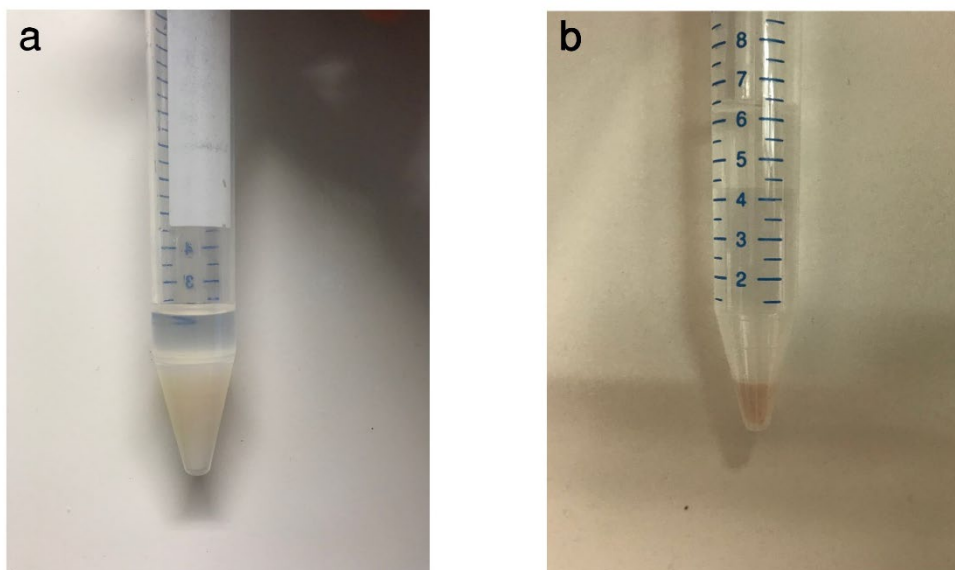


Figure A.2.8 Spent $4\text{Nb}_2\text{O}_5@\text{SBA-15}$ (a) at 84% and (b) at 100% conversion.

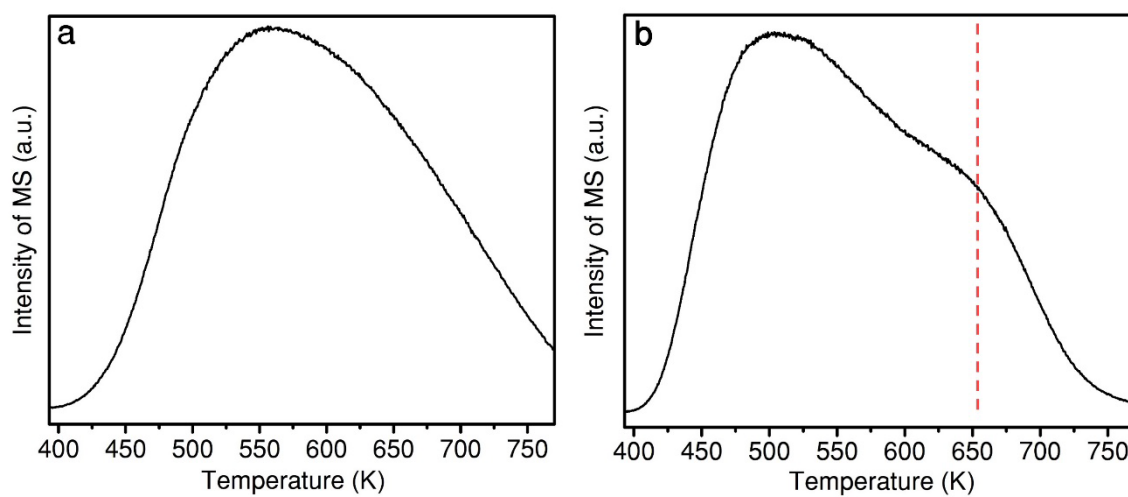


Figure A.2.9 Ammonia TPD result for (a) $4\text{Nb}_2\text{O}_5@\text{SBA-15}$ and (b) HY-340. HY-340 has a desorption band at $380\text{ }^\circ\text{C}$, which can be assigned to strong Brønsted acid sites.⁵¹

A.2.2 Mass transfer effects on reaction

HY-340 had a lower activity in Friedel-Crafts alkylation and a lower selectivity in xylose dehydration. To confirm that these observations were not due to mass transfer limitations, we performed stirring tests to exclude the effect of any external mass transfer and used the Weisz-Prater criterion to exclude the effects of internal mass transfer limitations. Specifically, we performed control experiments with a faster and slower stirring rate. We observed 57% (550 rpm) and 57% (700 rpm) conversion at 3 h for Friedel-Crafts alkylation and 42% (550 rpm) and 41% (700 rpm) conversion at 30 min for xylose dehydration. Because no significant external mass transfer limitation was observed, the concentration at the surface of the catalyst (C_{AS}) was assumed to be identical as the bulk concentration. Following this, we assessed any internal effects by using the Weisz-Prater criterion, which is the same equation described in section A.1.3:

$$\frac{r_{obs}(R_p)^2}{D_{TA}^e C_{AS}} < 1$$

Where:

r_{obs} is the observed reaction rate per unit volume of catalyst ($\text{mol}\cdot\text{s}^{-1}\cdot\text{cm}^{-3}$)

R_p is the spherical particles radius (cm)

D_{TA}^e is the effective transition diffusivity ($\text{cm}^2\cdot\text{s}^{-1}$)

C_{AS} is the concentration at the surface of the catalyst particle ($\text{mol}\cdot\text{cm}^{-3}$) which was set equal to the bulk concentration.

The particle radius of HY-340 was estimated using an optical microscope. The reaction rates were obtained experimentally. For Friedel-Crafts alkylation, the initial rate shown in Figure 6 was directly used for the calculation. For xylose dehydration, we performed the

reaction with a shorter reaction time (10 min) to obtained an average reaction rate at low conversion (14 %).

Bulk diffusivities of benzyl alcohol in anisole and xylose in water, were calculated using the Wilke-Chang equation:¹⁶⁸

$$D_{AB} = 7.4 \times 10^{-8} \frac{T (x M_B)^{1/2}}{\mu V_A^{0.6}}$$

Where μ is the solvent dynamic viscosity, T is the reaction temperature (K), M_B is the molecular weight of solvent, x is the association parameter (taken as 1) and V_A is the molar volume at the boiling point of the solute. The solvent dynamic viscosities were obtained from the literature (0.908 mPa·s for anisole and 0.89 mPa·s for water).^{175,176} In the absence of data at the reaction temperature, the dynamic viscosity at a lower temperature was used. This simplification leads to an underestimation of D_{AB} , and hence, an overestimation of the Weisz-Prater criterion, ensuring that no mass transfer effects are present. Using the method reported by Sastri, V_A was calculated as 124 cm³·mol⁻¹ for benzyl alcohol and 120 cm³·mol⁻¹ for xylose (furanose structure).¹⁷¹ The D_{AB} coefficient was then calculated as 1.89·10⁻⁵ for Friedel-Crafts alkylation and 7.84·10⁻⁶ for xylose dehydration.

The pore diffusivity can be determined by the equation below:¹⁶⁸

$$\frac{D_{AB,pore}}{D_{AB}} = (1 - \lambda)^4$$

$$\text{Where } \lambda = \frac{d_s}{d_p}$$

The solute diameter (d_s) was calculated using the MarvinSketch software and the average pore diameter of HY-340 (d_p) was determined by using the BJH adsorption analysis. The internal

diffusivity within the pores of the catalyst particles with respect to that of the bulk for liquid phase conditions was determined with this equation and summarized in Table A.2-1.

Table A.2-1 Physical properties of solute and HY-340

Parameter	Description	Unit	Friedel-Crafts alkylation	Xylose dehydration
d_s	solute diameter	nm	0.26	0.45
d_p	pore diameter	nm	6	6
$\frac{D_{AB,pore}}{D_{AB}}$	variation of diffusivity	-	0.837	0.732
$D_{AB,pore}$	pore diffusivity	$\text{cm}^2 \cdot \text{s}^{-1}$	$1.58 \cdot 10^{-5}$	$5.74 \cdot 10^{-6}$

The effective diffusivity was subsequently calculated using the porosity (ϵ) and the tortuosity (τ):

$$D_{TA}^e = D_{AB}^e = \frac{\epsilon}{\tau} D_{AB,pore}$$

In the absence of experimental data, ϵ and τ can be estimated according to Davis et al.¹⁷² The ϵ is 0.5 and the τ is 4 for both reactions. The D_{TA}^e was then calculated and the Weisz-Prater criterion was estimated (Table A.2-2).

Table A.2-2 Summary of Weisz-Prater criterion.

Parameter	Description	Unit	Friedel-Crafts alkylation	Xylose dehydration
r_{obs}	observed rate of reaction	$\text{mol}\cdot\text{cm}^{-3}\cdot\text{s}^{-1}$	$2.04\cdot 10^{-6}$	$8.7\cdot 10^{-7}$
R_p	particle radius	cm	$2\cdot 10^{-3}$	$2\cdot 10^{-3}$
D_{TA}^e	Effective diffusivity	$\text{cm}\cdot\text{s}^{-1}$	$1.98\cdot 10^{-6}$	$7.18\cdot 10^{-7}$
C_{AS}	surface concentration	$\text{mol}\cdot\text{cm}^{-3}$	$4.34\cdot 10^{-4}$	$2.5\cdot 10^{-4}$
	Weisz-Prater criterion		$9.5\cdot 10^{-3}$	$1.9\cdot 10^{-2}$

Since the calculated criterions were systematically several orders of magnitude below unity, we concluded that the reactions we ran were free of internal diffusion limitation. Although the observed rates were not obtained from the experiment with low conversion (ideally <5%) and no external diffusion limitation we assumed for calculations, the very low values of the Weisz-Prater criterion (between 10^{-3} to 10^{-2}), which suggest that these assumptions/simplifications are not going to change our conclusions.

A.3 Supplementary information of Chapter 4

A.3.1 Supporting figure and table



Figure A.3.1 Picture of as-synthesized $\text{Pd}(\text{en})_2/\text{SiO}_2$. The grafting of the yellow Pd complex on silica can be observed after the sedimentation of powder.

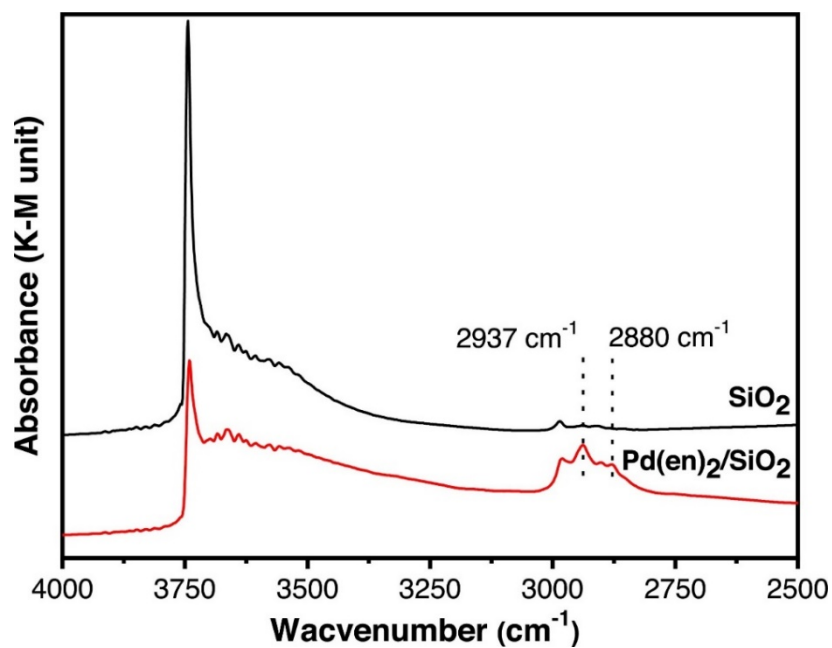


Figure A.3.2 FTIR spectra of pristine SiO_2 and $\text{Pd}(\text{en})_2/\text{SiO}_2$. The absorbance at around 2937 and 2880 cm^{-1} can be assigned to C-H stretching, indicating the presence of the Pd complex on SiO_2 surface.

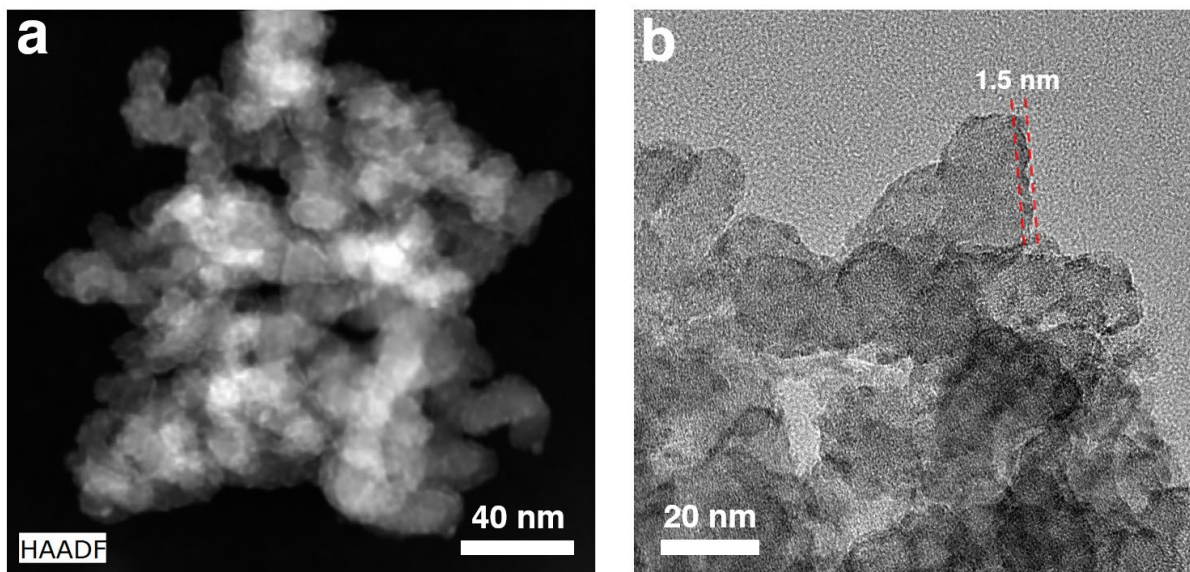


Figure A.3.3 (a) STEM and (b) TEM images of $\text{ZrO}_2@\text{Pd}/\text{SiO}_2$.

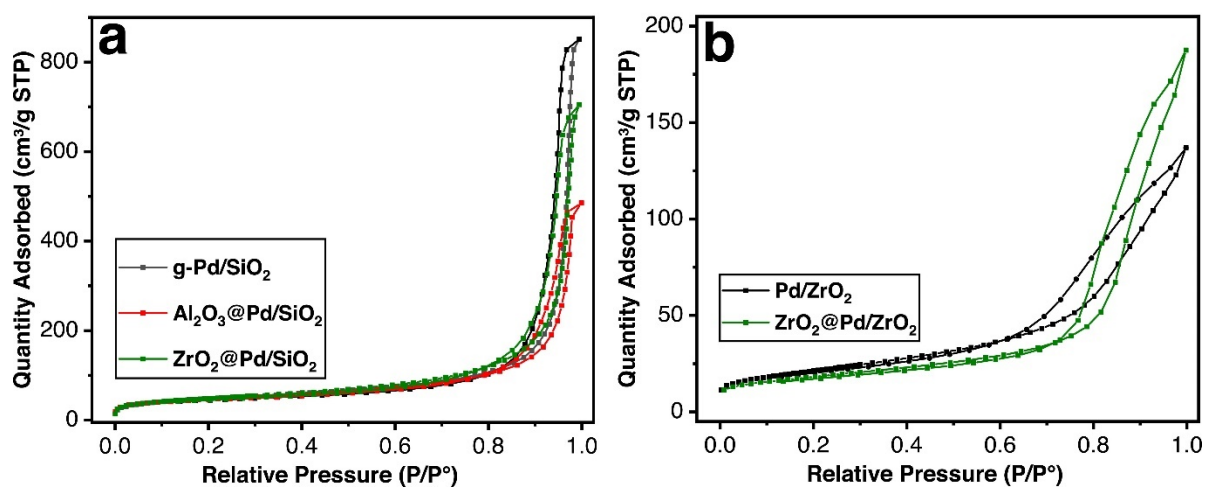


Figure A.3.4 N_2 Physisorption results for Pd catalysts with (a) SiO_2 and (b) ZrO_2 supports.

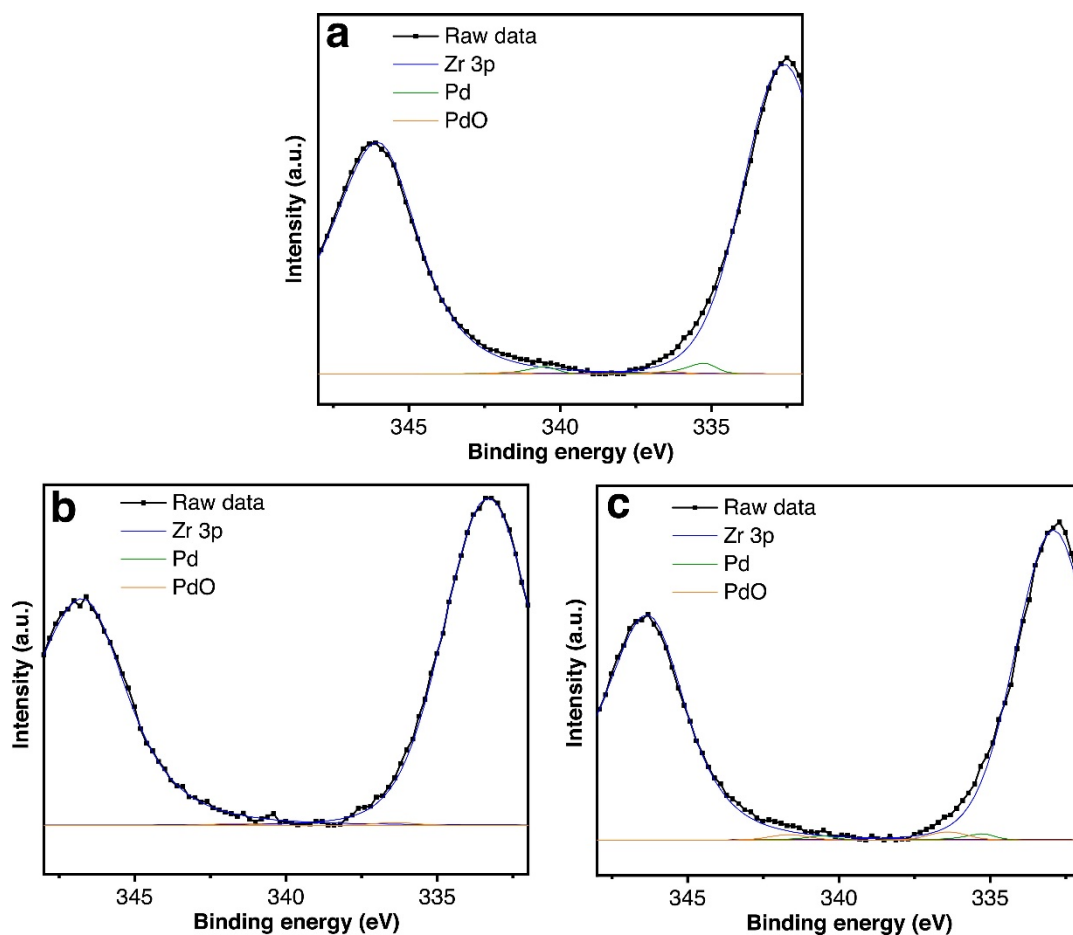


Figure A.3.5 XPS results for (a) Pd/ZrO₂ (b) ZrO₂@Pd/SiO₂ and (c) ZrO₂@Pd/ZrO₂.

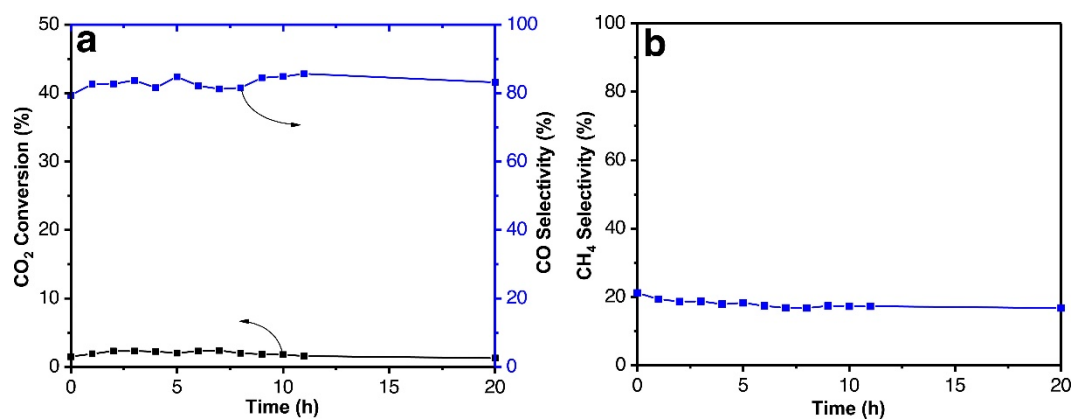


Figure A.3.6 (a) Conversion and CO selectivity and (b) CH₄ selectivities for CO₂ hydrogenation studies using g-Pd/SiO₂. The reaction condition was described in section 4.5.

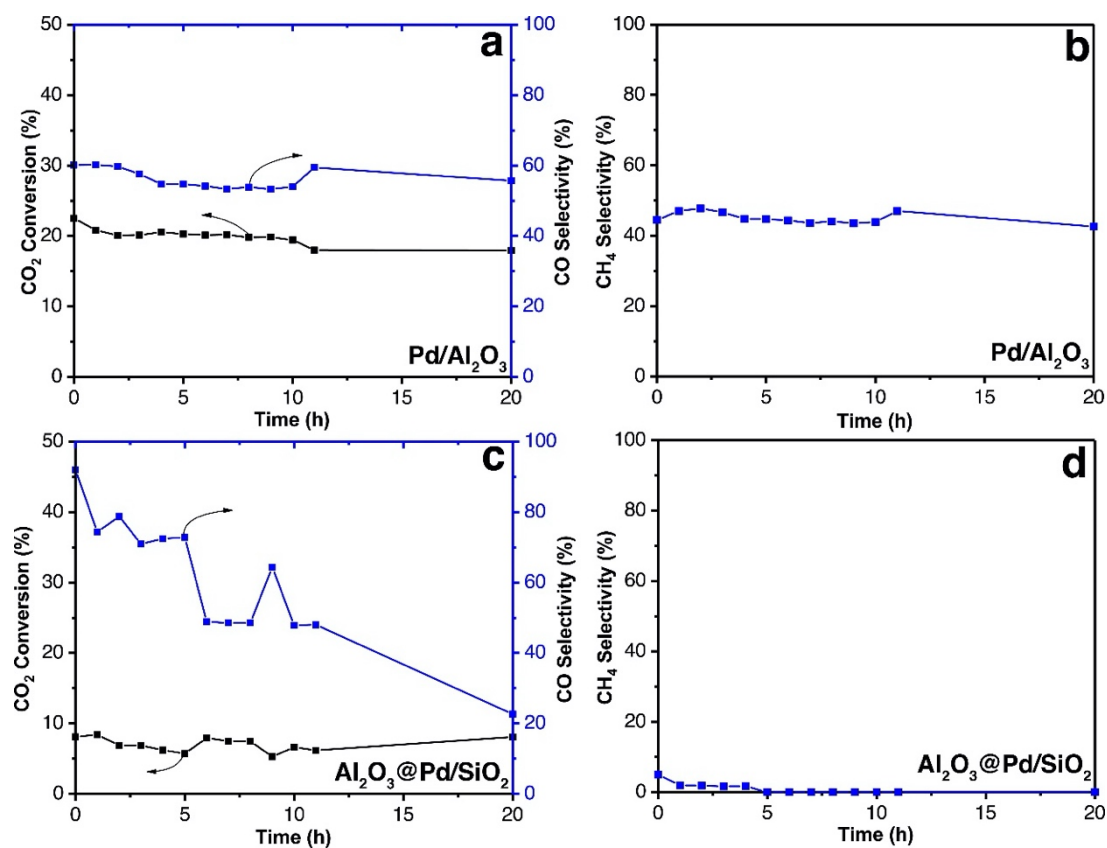


Figure A.3.7 (a) Conversion, CO selectivity and (b) CH₄ selectivity during CO₂ hydrogenation over Pd/Al₂O₃. (c) Conversion, CO selectivity and (d) CH₄ selectivity during CO₂ hydrogenation over Al₂O₃@Pd/SiO₂. The reaction condition was described in section 4.5.

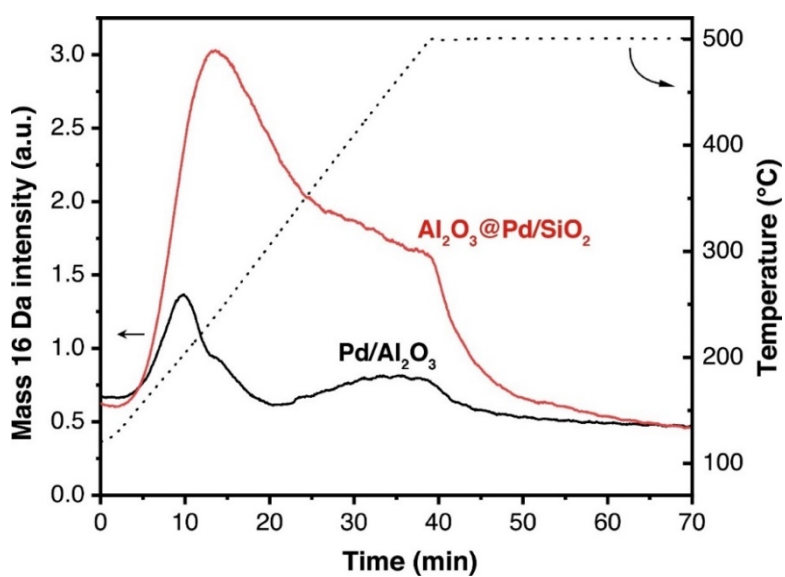


Figure A.3.8 NH₃-TPD results for Al₂O₃@Pd/SiO₂ (red) and Pd/Al₂O₃ (black).

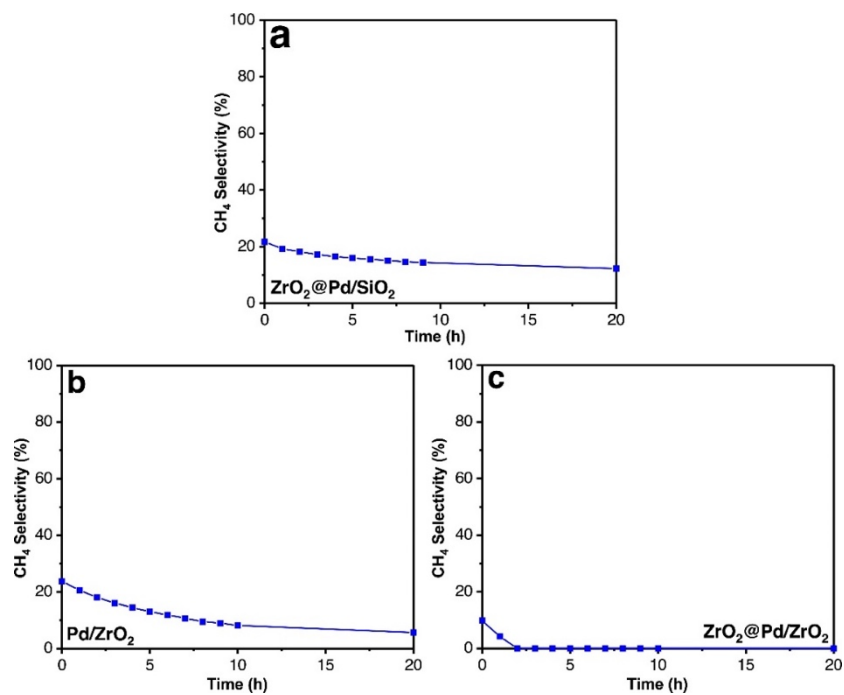


Figure A.3.9 CH₄ selectivities during CO₂ hydrogenation over (a) ZrO₂@Pd/SiO₂, (b) Pd/ZrO₂ and (c) ZrO₂@Pd/ZrO₂. The reaction condition was described in section 4.5.

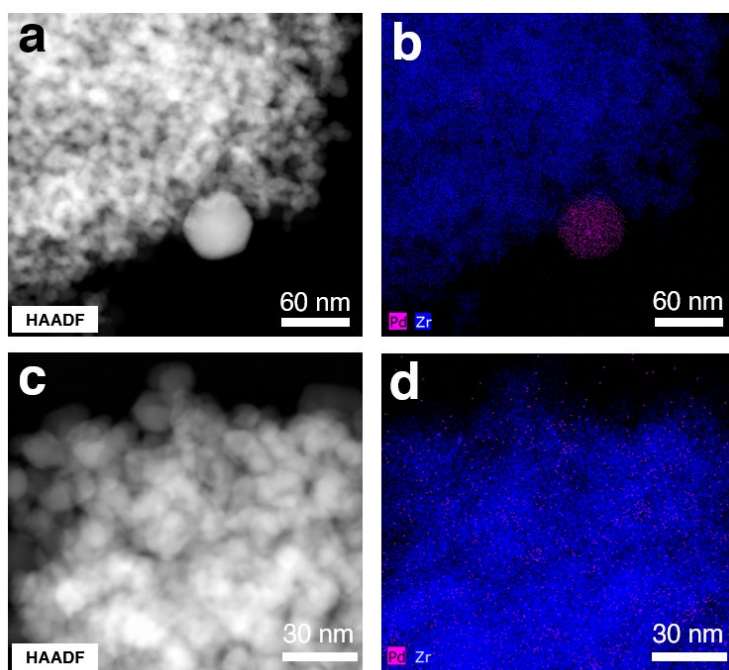


Figure A.3.10 STEM analyses of spent Pd/ZrO₂ (a) under HAADF mode and (b) with EDX mapping as well as spent ZrO₂@Pd@ZrO₂ (c) under HAADF mode and (d) with EDX mapping.

A.3.2 Mass transfer effects on reaction

To confirm that all measurements were free from external mass transfer effect, the Mears criterion was used to assess the influence of external mass transfer:

$$\frac{r_{obs} \cdot \rho \cdot d_p \cdot n}{k_c \cdot C_b} < 0.15$$

Where

r_{obs} = observed rate

ρ = catalyst bed density

d_p = catalyst pellet radius

n = reaction order

k_c = mass transfer coefficient

C_b = bulk concentration of reactant

For the assessment, the data of Pd/ZrO₂ was used because it had the highest observed reaction rate (based on the amount of CO₂ converted) per unit weight of catalyst, which would give the highest value in Mears criterion. The highest observed rate (r_{obs}) of Pd/ZrO₂ is 60.8 (μmol/g·s). The average radius of crushed pellets (d_p) was approximately 500 μm. Catalyst density (ρ) was 1060 g/m³. Concentration of CO₂ (C_b) was 16 mol/m³. Reaction order was less than 1 according to the literature so we used 1 for the calculation to calculate a worst case scenario.¹³⁷ For a packed bed reactor, the mass transfer coefficient is calculated using Sherwood number and Frössling correlation, which are shown below:¹⁷⁷

$$Sh = k_c \cdot \frac{d_p}{D_{AB}} = 2 + 0.6Re^{1/2} \cdot Sc^{1/3}$$

Where D_{AB} is diffusivity, Re is the Reynolds number and Sc is the Schmidt number, which is defined as the ratio of kinematic viscosity and diffusivity. Due to the relatively low concentration of H_2 in the reaction stream, we approximate our reaction system as a binary system (CO_2 and Ar) to simplify the calculation. The binary diffusion coefficient was estimated using the following equation:¹⁷⁸

$$D_{AB} = \frac{10^{-3} \cdot T^{1.75} \cdot (M_{CO_2}^{-1} + M_{Ar}^{-1})^{0.5}}{P \cdot (v_{CO_2}^{1/3} + v_{Ar}^{1/3})^2}$$

Where M is the molecular weight, T is the temperature (K), P is pressure (atm), and v is the special atomic diffusion volume of a gaseous component, which is provided by Fuller et al..¹⁷⁸ D_{AB} was calculated to be 0.0073 (m/s). The Reynolds and Schmidt number of our reaction were estimated as 0.23 and 0.0001, respectively. Using the above data and Frössling correlation, k_c was then calculated as 29 m/s. With k_c and the other experimental observables, the approximate value of Mears criterion was calculated as 6.6×10^{-8} , which was significantly lower than 0.15. Thus, we could safely assume that the reaction is free from external mass transfer limitations. Next, any internal mass transfer limitations were assessed by using the Weisz-Prater criterion:

$$\frac{r_{obs}(d_p)^2}{D_{AB}^e C_{AS}} < 1$$

Where D_{AB}^e is the effective diffusion coefficient in the pores and C_{AS} is the concentration on the catalyst surface. Because external mass transfer limitations are negligible, C_{AS} was set as equal to C_b . The effective diffusion coefficient for multicomponent mixture is calculated using the following equation:¹⁷⁹

$$\frac{1}{D_{AB}^*} = \frac{1}{D_k} + \sum_{\substack{j=1 \\ j \neq i}}^N \frac{C_j}{D_{i,j} C_t}$$

Where D_{ij} is the bulk diffusion coefficient, C is the concentration of gas component and D_K is the Knudsen diffusion coefficient which is given by the equation shown below:

$$D_K = \frac{4}{3} r_{pore} \sqrt{\frac{8RT}{\pi M}}$$

Where r_{pore} is the pore radius of catalyst. The average pore radius of Pd/ZrO₂ was 5 nm which was obtained using BJH desorption model. The D_K for CO₂ was then calculated as 1.24×10^{-7} (m/s). Since we have previously calculated the diffusion coefficient of the CO₂-Ar mixture (0.0073 m/s) that is four order of magnitude larger than D_K , the bulk coefficient terms would be insignificant when estimating D_{AB}^* . Therefore, D_K can be used as an approximation of D_{AB}^* . To obtain D_{AB}^e , D_K has to be multiplied by a catalyst internal porosity and a tortuosity factor (ε/τ). Although it is difficult to obtain these two data experimentally, the factor is usually bigger than 0.05.^{180,181} Given the slow reaction rate we observed (6.08×10^{-5} mol/g·s) and the small particle size (5×10^{-4} m), the resulting Weisz-Prater value would be below 10^{-2} even if an extremely low ε/τ value (0.01) was used. Therefore, we concluded that internal mass transfer limitations were negligible.

References

- (1) Concepts of Modern Catalysis and Kinetics | Wiley Online Books <https://onlinelibrary.wiley.com/doi/book/10.1002/3527602658> (accessed Dec 4, 2019).
- (2) Heterogeneous Catalysis. In *Catalysis*; John Wiley & Sons, Ltd, 2008; pp 127–187. <https://doi.org/10.1002/9783527621866.ch4>.
- (3) Fechete, I.; Wang, Y.; Védrine, J. C. The Past, Present and Future of Heterogeneous Catalysis. *Catalysis Today* **2012**, *189* (1), 2–27. <https://doi.org/10.1016/j.cattod.2012.04.003>.
- (4) Hakim, L. F.; Blackson, J.; George, S. M.; Weimer, A. W. Nanocoating Individual Silica Nanoparticles by Atomic Layer Deposition in a Fluidized Bed Reactor. *Chemical Vapor Deposition* **2005**, *11* (10), 420–425. <https://doi.org/10.1002/cvde.200506392>.
- (5) Leskelä, M.; Ritala, M. Atomic Layer Deposition Chemistry: Recent Developments and Future Challenges. *Angewandte Chemie International Edition* **2003**, *42* (45), 5548–5554. <https://doi.org/10.1002/anie.200301652>.
- (6) Li, W.; Yang, J.; Wu, Z.; Wang, J.; Li, B.; Feng, S.; Deng, Y.; Zhang, F.; Zhao, D. A Versatile Kinetics-Controlled Coating Method To Construct Uniform Porous TiO₂ Shells for Multifunctional Core–Shell Structures. *J. Am. Chem. Soc.* **2012**, *134* (29), 11864–11867. <https://doi.org/10.1021/ja3037146>.
- (7) Héroguel, F.; Le Monnier, B. P.; Brown, K. S.; Siu, J. C.; Luterbacher, J. S. Catalyst Stabilization by Stoichiometrically Limited Layer-by-Layer Overcoating in Liquid Media. *Applied Catalysis B: Environmental* **2017**, *218*, 643–649. <https://doi.org/10.1016/j.apcatb.2017.07.006>.
- (8) Wu, Y.; Döhler, D.; Barr, M.; Oks, E.; Wolf, M.; Santinacci, L.; Bachmann, J. Atomic Layer Deposition from Dissolved Precursors. *Nano Lett.* **2015**, *15* (10), 6379–6385. <https://doi.org/10.1021/acs.nanolett.5b01424>.
- (9) O'Neill, B. J.; Jackson, D. H. K.; Lee, J.; Canlas, C.; Stair, P. C.; Marshall, C. L.; Elam, J. W.; Kuech, T. F.; Dumesic, J. A.; Huber, G. W. Catalyst Design with Atomic Layer Deposition. *ACS Catal.* **2015**, *5* (3), 1804–1825. <https://doi.org/10.1021/cs501862h>.
- (10) Longrie, D.; Deduytsche, D.; Detavernier, C. Reactor Concepts for Atomic Layer Deposition on Agitated Particles: A Review. *Journal of Vacuum Science & Technology A* **2013**, *32* (1), 010802. <https://doi.org/10.1116/1.4851676>.
- (11) Brinker, C. J.; Scherer, G. W. *Sol-Gel Science: The Physics and Chemistry of Sol-Gel Processing*; Academic Press, 2013.
- (12) E. Danks, A.; R. Hall, S.; Schnepf, Z. The Evolution of ‘Sol–Gel’ Chemistry as a Technique for Materials Synthesis. *Materials Horizons* **2016**, *3* (2), 91–112. <https://doi.org/10.1039/C5MH00260E>.
- (13) Brown, K. S.; Saggese, C.; Le Monnier, B. P.; Héroguel, F.; Luterbacher, J. S. Simulation of Gas- and Liquid-Phase Layer-By-Layer Deposition of Metal Oxides by Coarse-Grained Modeling. *J. Phys. Chem. C* **2018**, *122* (12), 6713–6720. <https://doi.org/10.1021/acs.jpcc.8b00197>.

- (14) Stöber, W.; Fink, A.; Bohn, E. Controlled Growth of Monodisperse Silica Spheres in the Micron Size Range. *Journal of Colloid and Interface Science* **1968**, *26* (1), 62–69. [https://doi.org/10.1016/0021-9797\(68\)90272-5](https://doi.org/10.1016/0021-9797(68)90272-5).
- (15) Nozawa, K.; Gailhanou, H.; Raison, L.; Panizza, P.; Ushiki, H.; Sellier, E.; Delville, J. P.; Delville, M. H. Smart Control of Monodisperse Stöber Silica Particles: Effect of Reactant Addition Rate on Growth Process. *Langmuir* **2005**, *21* (4), 1516–1523. <https://doi.org/10.1021/la048569r>.
- (16) Matsoukas, T.; Gulari, E. Dynamics of Growth of Silica Particles from Ammonia-Catalyzed Hydrolysis of Tetra-Ethyl-Orthosilicate. *Journal of Colloid and Interface Science* **1988**, *124* (1), 252–261. [https://doi.org/10.1016/0021-9797\(88\)90346-3](https://doi.org/10.1016/0021-9797(88)90346-3).
- (17) Han, Y.; Lu, Z.; Teng, Z.; Liang, J.; Guo, Z.; Wang, D.; Han, M.-Y.; Yang, W. Unraveling the Growth Mechanism of Silica Particles in the Stöber Method: In Situ Seeded Growth Model. *Langmuir* **2017**, *33* (23), 5879–5890. <https://doi.org/10.1021/acs.langmuir.7b01140>.
- (18) Zhang, Q.; Lee, I.; Joo, J. B.; Zaera, F.; Yin, Y. Core–Shell Nanostructured Catalysts. *Acc. Chem. Res.* **2013**, *46* (8), 1816–1824. <https://doi.org/10.1021/ar300230s>.
- (19) Vehkamäki, H. *Classical Nucleation Theory in Multicomponent Systems*; Springer-Verlag: Berlin Heidelberg, 2006. <https://doi.org/10.1007/3-540-31218-8>.
- (20) Okudera, H.; Hozumi, A. The Formation and Growth Mechanisms of Silica Thin Film and Spherical Particles through the Stöber Process. *Thin Solid Films* **2003**, *434* (1), 62–68. [https://doi.org/10.1016/S0040-6090\(03\)00535-2](https://doi.org/10.1016/S0040-6090(03)00535-2).
- (21) Ichinose, I.; Senzu, H.; Kunitake, T. Stepwise Adsorption of Metal Alkoxides on Hydrolyzed Surfaces: A Surface Sol-Gel Process. *CHEM. LETT.* **1996**, No. 10, 831–832. <https://doi.org/10.1246/cl.1996.831>.
- (22) Osatiashtiani, A.; Lee, A. F.; Granollers, M.; Brown, D. R.; Olivi, L.; Morales, G.; Melero, J. A.; Wilson, K. Hydrothermally Stable, Conformal, Sulfated Zirconia Monolayer Catalysts for Glucose Conversion to 5-HMF. *ACS Catal.* **2015**, *5* (7), 4345–4352. <https://doi.org/10.1021/acscatal.5b00965>.
- (23) O'Neill, B. J.; Jackson, D. H. K.; Crisci, A. J.; Farberow, C. A.; Shi, F.; Alba-Rubio, A. C.; Lu, J.; Dietrich, P. J.; Gu, X.; Marshall, C. L.; et al. Stabilization of Copper Catalysts for Liquid-Phase Reactions by Atomic Layer Deposition. *Angew. Chem. Int. Ed.* **2013**, *52* (51), 13808–13812. <https://doi.org/10.1002/anie.201308245>.
- (24) Kresge, C. T.; Leonowicz, M. E.; Roth, W. J.; Vartuli, J. C.; Beck, J. S. Ordered Mesoporous Molecular Sieves Synthesized by a Liquid-Crystal Template Mechanism. *Nature* **1992**, *359* (6397), 710. <https://doi.org/10.1038/359710a0>.
- (25) Yang, P.; Zhao, D.; Margolese, D. I.; Chmelka, B. F.; Stucky, G. D. Generalized Syntheses of Large-Pore Mesoporous Metal Oxides with Semicrystalline Frameworks. *Nature* **1998**, *396* (6707), 152–155. <https://doi.org/10.1038/24132>.
- (26) Mahurin, S.; Bao, L.; Yan, W.; Liang, C.; Dai, S. Atomic Layer Deposition of TiO₂ on Mesoporous Silica. *Journal of Non-Crystalline Solids* **2006**, *352* (30), 3280–3284. <https://doi.org/10.1016/j.jnoncrysol.2006.05.008>.
- (27) Singh, R.; Bapat, R.; Qin, L.; Feng, H.; Polshettiwar, V. Atomic Layer Deposited (ALD) TiO₂ on Fibrous Nano-Silica (KCC-1) for Photocatalysis: Nanoparticle Formation and

- Size Quantization Effect. *ACS Catal.* **2016**, *6* (5), 2770–2784. <https://doi.org/10.1021/acscatal.6b00418>.
- (28) Perathoner, S.; Lanzafame, P.; Passalacqua, R.; Centi, G.; Schlögl, R.; Su, D. S. Use of Mesoporous SBA-15 for Nanostructuring Titania for Photocatalytic Applications. *Microporous and Mesoporous Materials* **2006**, *90* (1), 347–361. <https://doi.org/10.1016/j.micromeso.2005.10.024>.
 - (29) Pagán-Torres, Y. J.; Gallo, J. M. R.; Wang, D.; Pham, H. N.; Libera, J. A.; Marshall, C. L.; Elam, J. W.; Datye, A. K.; Dumesic, J. A. Synthesis of Highly Ordered Hydrothermally Stable Mesoporous Niobia Catalysts by Atomic Layer Deposition. *ACS Catal.* **2011**, *1* (10), 1234–1245. <https://doi.org/10.1021/cs200367t>.
 - (30) Héroguel, F.; Rozmysłowicz, B.; Luterbacher, J. S. Improving Heterogeneous Catalyst Stability for Liquid-Phase Biomass Conversion and Reforming. *CHIMIA International Journal for Chemistry* **2015**, *69* (10), 582–591. <https://doi.org/10.2533/chimia.2015.582>.
 - (31) Goodman, E. D.; Schwalbe, J. A.; Cargnello, M. Mechanistic Understanding and the Rational Design of Sinter-Resistant Heterogeneous Catalysts. *ACS Catal.* **2017**, 7156–7173. <https://doi.org/10.1021/acscatal.7b01975>.
 - (32) Liu, J.; Ji, Q.; Imai, T.; Ariga, K.; Abe, H. Sintering-Resistant Nanoparticles in Wide-Mouthed Compartments for Sustained Catalytic Performance. *Scientific Reports* **2017**, *7*, 41773. <https://doi.org/10.1038/srep41773>.
 - (33) Liu, X.; Zhu, Q.; Lang, Y.; Cao, K.; Chu, S.; Shan, B.; Chen, R. Oxide-Nanotrap-Anchored Platinum Nanoparticles with High Activity and Sintering Resistance by Area-Selective Atomic Layer Deposition. *Angew. Chem.* **2017**, *129* (6), 1670–1674. <https://doi.org/10.1002/ange.201611559>.
 - (34) Lee, I.; Zhang, Q.; Ge, J.; Yin, Y.; Zaera, F. Encapsulation of Supported Pt Nanoparticles with Mesoporous Silica for Increased Catalyst Stability. *Nano Res.* **2011**, *4* (1), 115–123. <https://doi.org/10.1007/s12274-010-0059-8>.
 - (35) Zhu, H.; Ma, Z.; Overbury, S. H.; Dai, S. Rational Design of Gold Catalysts with Enhanced Thermal Stability: Post Modification of Au/TiO₂ by Amorphous SiO₂ Decoration. *Catal Lett* **2007**, *116* (3–4), 128–135. <https://doi.org/10.1007/s10562-007-9144-3>.
 - (36) Lu, J.; Fu, B.; Kung, M. C.; Xiao, G.; Elam, J. W.; Kung, H. H.; Stair, P. C. Coking- and Sintering-Resistant Palladium Catalysts Achieved Through Atomic Layer Deposition. *Science* **2012**, *335* (6073), 1205–1208. <https://doi.org/10.1126/science.1212906>.
 - (37) Lee, J.; Jackson, D. H. K.; Li, T.; Winans, R. E.; Dumesic, J. A.; Kuech, T. F.; Huber, G. W. Enhanced Stability of Cobalt Catalysts by Atomic Layer Deposition for Aqueous-Phase Reactions. *Energy Environ. Sci.* **2014**, *7* (5), 1657–1660. <https://doi.org/10.1039/C4EE00379A>.
 - (38) Zhang, Q.; Lee, I.; Ge, J.; Zaera, F.; Yin, Y. Surface-Protected Etching of Mesoporous Oxide Shells for the Stabilization of Metal Nanocatalysts. *Advanced Functional Materials* **2010**, *20* (14), 2201–2214. <https://doi.org/10.1002/adfm.201000428>.
 - (39) Lu, P.; Campbell, C. T.; Xia, Y. A Sinter-Resistant Catalytic System Fabricated by Maneuvering the Selectivity of SiO₂ Deposition onto the TiO₂ Surface versus the Pt

- Nanoparticle Surface. *Nano Lett.* **2013**, *13* (10), 4957–4962. <https://doi.org/10.1021/nl4029973>.
- (40) Lu, J.; Stair, P. C. Low-Temperature ABC-Type Atomic Layer Deposition: Synthesis of Highly Uniform Ultrafine Supported Metal Nanoparticles. *Angewandte Chemie International Edition* **2010**, *49* (14), 2547–2551. <https://doi.org/10.1002/anie.200907168>.
 - (41) Frenkel, A. I.; Rodriguez, J. A.; Chen, J. G. Synchrotron Techniques for In Situ Catalytic Studies: Capabilities, Challenges, and Opportunities. *ACS Catal.* **2012**, *2* (11), 2269–2280. <https://doi.org/10.1021/cs3004006>.
 - (42) Nørskov, J. K.; Bligaard, T.; Rossmeisl, J.; Christensen, C. H. Towards the Computational Design of Solid Catalysts. *Nature Chemistry* **2009**, *1* (1), 37–46. <https://doi.org/10.1038/nchem.121>.
 - (43) Tauster, S. J.; Fung, S. C.; Baker, R. T. K.; Horsley, J. A. Strong Interactions in Supported-Metal Catalysts. *Science* **1981**, *211* (4487), 1121–1125. <https://doi.org/10.1126/science.211.4487.1121>.
 - (44) Ro, I.; Resasco, J.; Christopher, P. Approaches for Understanding and Controlling Interfacial Effects in Oxide-Supported Metal Catalysts. *ACS Catal.* **2018**, *8* (8), 7368–7387. <https://doi.org/10.1021/acscatal.8b02071>.
 - (45) Albani, D.; Li, Q.; Vilé, G.; Mitchell, S.; Almora-Barrios, N.; Witte, P. T.; López, N.; Pérez-Ramírez, J. Interfacial Acidity in Ligand-Modified Ruthenium Nanoparticles Boosts the Hydrogenation of Levulinic Acid to Gamma-Valerolactone. *Green Chem.* **2017**, *19* (10), 2361–2370. <https://doi.org/10.1039/C6GC02586B>.
 - (46) Lu, J.; Behtash, S.; Mamun, O.; Heyden, A. Theoretical Investigation of the Reaction Mechanism of the Guaiacol Hydrogenation over a Pt(111) Catalyst. *ACS Catal.* **2015**, *5* (4), 2423–2435. <https://doi.org/10.1021/cs5016244>.
 - (47) Zhang, J.; Medlin, J. W. Catalyst Design Using an Inverse Strategy: From Mechanistic Studies on Inverted Model Catalysts to Applications of Oxide-Coated Metal Nanoparticles. *Surface Science Reports* **2018**, *73* (4), 117–152. <https://doi.org/10.1016/j.surfrep.2018.06.002>.
 - (48) Onn, T. M.; Zhang, S.; Arroyo-Ramirez, L.; Chung, Y.-C.; Graham, G. W.; Pan, X.; Gorte, R. J. Improved Thermal Stability and Methane-Oxidation Activity of Pd/Al₂O₃ Catalysts by Atomic Layer Deposition of ZrO₂. *ACS Catal.* **2015**, *5* (10), 5696–5701. <https://doi.org/10.1021/acscatal.5b01348>.
 - (49) Yi, H.; Du, H.; Hu, Y.; Yan, H.; Jiang, H.-L.; Lu, J. Precisely Controlled Porous Alumina Overcoating on Pd Catalyst by Atomic Layer Deposition: Enhanced Selectivity and Durability in Hydrogenation of 1,3-Butadiene. *ACS Catal.* **2015**, *5* (5), 2735–2739. <https://doi.org/10.1021/acscatal.5b00129>.
 - (50) Leydier, F.; Chizallet, C.; Chaumonnot, A.; Digne, M.; Soyer, E.; Quoineaud, A.-A.; Costa, D.; Raybaud, P. Brønsted Acidity of Amorphous Silica–Alumina: The Molecular Rules of Proton Transfer. *Journal of Catalysis* **2011**, *284* (2), 215–229. <https://doi.org/10.1016/j.jcat.2011.08.015>.
 - (51) Ardagh, M. A.; Bo, Z.; Nauert, S. L.; Notestein, J. M. Depositing SiO₂ on Al₂O₃: A Route to Tunable Brønsted Acid Catalysts. *ACS Catal.* **2016**, *6* (9), 6156–6164. <https://doi.org/10.1021/acscatal.6b01077>.

- (52) Weng, Z.; Zaera, F. Sub-Monolayer Control of Mixed-Oxide Support Composition in Catalysts via Atomic Layer Deposition: Selective Hydrogenation of Cinnamaldehyde Promoted by (SiO₂-ALD)-Pt/Al₂O₃. *ACS Catal.* **2018**, *8* (9), 8513–8524. <https://doi.org/10.1021/acscatal.8b02431>.
- (53) Álvarez Galván, C.; Schumann, J.; Behrens, M.; Fierro, J. L. G.; Schlögl, R.; Frei, E. Reverse Water-Gas Shift Reaction at the Cu/ZnO Interface: Influence of the Cu/Zn Ratio on Structure-Activity Correlations. *Applied Catalysis B: Environmental* **2016**, *195*, 104–111. <https://doi.org/10.1016/j.apcatb.2016.05.007>.
- (54) Rodriguez, J. A.; Liu, P.; Stacchiola, D. J.; Senanayake, S. D.; White, M. G.; Chen, J. G. Hydrogenation of CO₂ to Methanol: Importance of Metal–Oxide and Metal–Carbide Interfaces in the Activation of CO₂. *ACS Catal.* **2015**, *5* (11), 6696–6706. <https://doi.org/10.1021/acscatal.5b01755>.
- (55) Acosta, S.; Corriu, R. J. P.; Leclercq, D.; Lefèvre, P.; Mutin, P. H.; Vioux, A. Preparation of Alumina Gels by a Non-Hydrolytic Sol-Gel Processing Method. *Journal of Non-Crystalline Solids* **1994**, *170* (3), 234–242. [https://doi.org/10.1016/0022-3093\(94\)90052-3](https://doi.org/10.1016/0022-3093(94)90052-3).
- (56) Arnal, P.; Corriu, R. J. P.; Leclercq, D.; Mutin, P. H.; Vioux, A. A Solution Chemistry Study of Nonhydrolytic Sol–Gel Routes to Titania. *Chem. Mater.* **1997**, *9* (3), 694–698. <https://doi.org/10.1021/cm960337t>.
- (57) Vioux, A. Nonhydrolytic Sol–Gel Routes to Oxides. *Chem. Mater.* **1997**, *9* (11), 2292–2299. <https://doi.org/10.1021/cm970322a>.
- (58) Babonneau, F.; Coury, L.; Livage, J. Aluminum Sec-Butoxide Modified with Ethylacetoacetate: An Attractive Precursor for the Sol-Gel Synthesis of Ceramics. *Journal of Non-Crystalline Solids* **1990**, *121* (1–3), 153–157. [https://doi.org/10.1016/0022-3093\(90\)90122-3](https://doi.org/10.1016/0022-3093(90)90122-3).
- (59) Bonhomme-Coury, L.; Babonneau, F.; Livage, J. Investigation of the Sol-Gel Chemistry of Ethylacetoacetate Modified Aluminum Sec-Butoxide. *J Sol-Gel Sci Technol* **1994**, *3* (3), 157–168. <https://doi.org/10.1007/BF00486555>.
- (60) Kurajica, S.; Popović, J.; Kraljević, T. G.; Tkalčec, E.; Simčić, I.; Mandić, V.; Altomare, A.; Moliterni, A.; Rocquefelte, X. A Structural Investigation of Tris(Ethyl Acetoacetate)Aluminium (III). *J Sol-Gel Sci Technol* **2014**, *71* (2), 217–223. <https://doi.org/10.1007/s10971-014-3345-1>.
- (61) Baca, M.; de la Rochefoucauld, E.; Ambroise, E.; Krafft, J.-M.; Hajjar, R.; Man, P. P.; Carrier, X.; Blanchard, J. Characterization of Mesoporous Alumina Prepared by Surface Alumination of SBA-15. *Microporous and Mesoporous Materials* **2008**, *110* (2–3), 232–241. <https://doi.org/10.1016/j.micromeso.2007.06.010>.
- (62) Parlett, C. M. A.; Durndell, L. J.; Machado, A.; Cibir, G.; Bruce, D. W.; Hondow, N. S.; Wilson, K.; Lee, A. F. Alumina-Grafted SBA-15 as a High Performance Support for Pd-Catalysed Cinnamyl Alcohol Selective Oxidation. *Catalysis Today* **2014**, *229*, 46–55. <https://doi.org/10.1016/j.cattod.2013.11.056>.
- (63) Iengo, P.; Di Serio, M.; Sorrentino, A.; Solinas, V.; Santacesaria, E. Preparation and Properties of New Acid Catalysts Obtained by Grafting Alkoxides and Derivatives on the Most Common Supports Note I — Grafting Aluminium and Zirconium Alkoxides and Related Sulphates on Silica. *Applied Catalysis A: General* **1998**, *167* (1), 85–101. [https://doi.org/10.1016/S0926-860X\(97\)00303-7](https://doi.org/10.1016/S0926-860X(97)00303-7).

- (64) Canlas, C. P.; Lu, J.; Ray, N. A.; Grosso-Giordano, N. A.; Lee, S.; Elam, J. W.; Winans, R. E.; Van Duyne, R. P.; Stair, P. C.; Notestein, J. M. Shape-Selective Sieving Layers on an Oxide Catalyst Surface. *Nat Chem* **2012**, *4* (12), 1030–1036. <https://doi.org/10.1038/nchem.1477>.
- (65) Nass, R.; Schmidt, H. Synthesis of an Alumina Coating from Chelated Aluminium Alkoxides. *Journal of Non-Crystalline Solids* **1990**, *121* (1), 329–333. [https://doi.org/10.1016/0022-3093\(90\)90153-D](https://doi.org/10.1016/0022-3093(90)90153-D).
- (66) Luterbacher, J. S.; Alonso, D. M.; Dumesic, J. A. Targeted Chemical Upgrading of Lignocellulosic Biomass to Platform Molecules. *Green Chem.* **2014**, *16* (12), 4816–4838. <https://doi.org/10.1039/C4GC01160K>.
- (67) Huber, G. W.; Iborra, S.; Corma, A. Synthesis of Transportation Fuels from Biomass: Chemistry, Catalysts, and Engineering. *Chem. Rev.* **2006**, *106* (9), 4044–4098. <https://doi.org/10.1021/cr068360d>.
- (68) Lu, Q.; Li, W.-Z.; Zhu, X.-F. Overview of Fuel Properties of Biomass Fast Pyrolysis Oils. *Energy Conversion and Management* **2009**, *50* (5), 1376–1383. <https://doi.org/10.1016/j.enconman.2009.01.001>.
- (69) Shuai, L.; Amiri, M. T.; Questell-Santiago, Y. M.; Héroguel, F.; Li, Y.; Kim, H.; Meilan, R.; Chapple, C.; Ralph, J.; Luterbacher, J. S. Formaldehyde Stabilization Facilitates Lignin Monomer Production during Biomass Depolymerization. *Science* **2016**, *354* (6310), 329–333. <https://doi.org/10.1126/science.aaf7810>.
- (70) Lan, W.; Amiri, M. T.; Hunston, C. M.; Luterbacher, J. S. Protection Group Effects During α,γ -Diol Lignin Stabilization Promote High-Selectivity Monomer Production. *Angew. Chem. Int. Ed.* **2018**, *57* (5), 1356–1360. <https://doi.org/10.1002/anie.201710838>.
- (71) Klein, I.; Saha, B.; Abu-Omar, M. M. Lignin Depolymerization over Ni/C Catalyst in Methanol, a Continuation: Effect of Substrate and Catalyst Loading. *Catal. Sci. Technol.* **2015**, *5* (6), 3242–3245. <https://doi.org/10.1039/C5CY00490J>.
- (72) Koelewijn, S.-F.; Bosch, S. V. den; Renders, T.; Schutyser, W.; Lagrain, B.; Smet, M.; Thomas, J.; Dehaen, W.; Puyvelde, P. V.; Witters, H.; et al. Sustainable Bisphenols from Renewable Softwood Lignin Feedstock for Polycarbonates and Cyanate Ester Resins. *Green Chem.* **2017**, *19* (11), 2561–2570. <https://doi.org/10.1039/C7GC00776K>.
- (73) Robinson, A. M.; Hensley, J. E.; Medlin, J. W. Bifunctional Catalysts for Upgrading of Biomass-Derived Oxygenates: A Review. *ACS Catal.* **2016**, *6* (8), 5026–5043. <https://doi.org/10.1021/acscatal.6b00923>.
- (74) Héroguel, F.; Silvioli, L.; Du, Y.-P.; Luterbacher, J. S. Controlled Deposition of Titanium Oxide Overcoats by Non-Hydrolytic Sol Gel for Improved Catalyst Selectivity and Stability. *Journal of Catalysis* **2018**, *358*, 50–61. <https://doi.org/10.1016/j.jcat.2017.11.023>.
- (75) Lee, H.; Kim, H.; Yu, M. J.; Ko, C. H.; Jeon, J.-K.; Jae, J.; Park, S. H.; Jung, S.-C.; Park, Y.-K. Catalytic Hydrodeoxygenation of Bio-Oil Model Compounds over Pt/HY Catalyst. *Scientific Reports* **2016**, *6*, 28765. <https://doi.org/10.1038/srep28765>.
- (76) Nimmanwudipong, T.; Runnebaum, R. C.; Block, D. E.; Gates, B. C. Catalytic Conversion of Guaiacol Catalyzed by Platinum Supported on Alumina: Reaction Network Including Hydrodeoxygenation Reactions. *Energy Fuels* **2011**, *25* (8), 3417–3427. <https://doi.org/10.1021/ef200803d>.

- (77) Hellinger, M.; Carvalho, H. W. P.; Baier, S.; Wang, D.; Kleist, W.; Grunwaldt, J.-D. Catalytic Hydrodeoxygenation of Guaiacol over Platinum Supported on Metal Oxides and Zeolites. *Applied Catalysis A: General* **2015**, *490*, 181–192. <https://doi.org/10.1016/j.apcata.2014.10.043>.
- (78) de Souza, P. M.; Rabelo-Neto, R. C.; Borges, L. E. P.; Jacobs, G.; Davis, B. H.; Resasco, D. E.; Noronha, F. B. Hydrodeoxygenation of Phenol over Pd Catalysts. Effect of Support on Reaction Mechanism and Catalyst Deactivation. *ACS Catal.* **2017**, *7* (3), 2058–2073. <https://doi.org/10.1021/acscatal.6b02022>.
- (79) Bykova, M. V.; Ermakov, D. Yu.; Kaichev, V. V.; Bulavchenko, O. A.; Saraev, A. A.; Lebedev, M. Yu.; Yakovlev, V. A. Ni-Based Sol–Gel Catalysts as Promising Systems for Crude Bio-Oil Upgrading: Guaiacol Hydrodeoxygenation Study. *Applied Catalysis B: Environmental* **2012**, *113–114*, 296–307. <https://doi.org/10.1016/j.apcatb.2011.11.051>.
- (80) Horáček, J.; Štávková, G.; Kelbichová, V.; Kubička, D. Zeolite-Beta-Supported Platinum Catalysts for Hydrogenation/Hydrodeoxygenation of Pyrolysis Oil Model Compounds. *Catalysis Today* **2013**, *204*, 38–45. <https://doi.org/10.1016/j.cattod.2012.08.015>.
- (81) Digne, M.; Sautet, P.; Raybaud, P.; Euzen, P.; Toulhoat, H. Hydroxyl Groups on γ -Alumina Surfaces: A DFT Study. *Journal of Catalysis* **2002**, *211* (1), 1–5. <https://doi.org/10.1006/jcat.2002.3741>.
- (82) Chen, F. R.; Davis, J. G.; Fripiat, J. J. Aluminum Coordination and Lewis Acidity in Transition Aluminas. *Journal of Catalysis* **1992**, *133* (2), 263–278. [https://doi.org/10.1016/0021-9517\(92\)90239-E](https://doi.org/10.1016/0021-9517(92)90239-E).
- (83) Galarneau, A.; Cambon, H.; Di Renzo, F.; Fajula, F. True Microporosity and Surface Area of Mesoporous SBA-15 Silicas as a Function of Synthesis Temperature. *Langmuir* **2001**, *17* (26), 8328–8335. <https://doi.org/10.1021/la0105477>.
- (84) Berlowitz, P. J.; Peden, C. H. F.; Goodman, D. W. Kinetics of Carbon Monoxide Oxidation on Single-Crystal Palladium, Platinum, and Iridium. *J. Phys. Chem.* **1988**, *92* (18), 5213–5221. <https://doi.org/10.1021/j100329a030>.
- (85) Hinrichsen O.; Genger T.; Muhler M. Chemisorption of N₂O and H₂ for the Surface Determination of Copper Catalysts. *Chemical Engineering & Technology* **2000**, *23* (11), 956–959. [https://doi.org/10.1002/1521-4125\(200011\)23:11<956::AID-CEAT956>3.0.CO;2-L](https://doi.org/10.1002/1521-4125(200011)23:11<956::AID-CEAT956>3.0.CO;2-L).
- (86) Krishnan, C. K.; Hayashi, T.; Ogura, M. A New Method for Post-Synthesis Coating of Zirconia on the Mesopore Walls of SBA-15 Without Pore Blocking. *Adv. Mater.* **2008**, *20* (11), 2131–2136. <https://doi.org/10.1002/adma.200702822>.
- (87) Kondo, J. N.; Hiyoshi, Y.; Osuga, R.; Ishikawa, A.; Wang, Y.-H.; Yokoi, T. Thin (Single–Triple) Niobium Oxide Layers on Mesoporous Silica Substrate. *Microporous and Mesoporous Materials* **2018**, *262*, 191–198. <https://doi.org/10.1016/j.micromeso.2017.11.032>.
- (88) Zhao, D.; Feng, J.; Huo, Q.; Melosh, N.; Fredrickson, G. H.; Chmelka, B. F.; Stucky, G. D. Triblock Copolymer Syntheses of Mesoporous Silica with Periodic 50 to 300 Angstrom Pores. *Science* **1998**, *279* (5350), 548–552. <https://doi.org/10.1126/science.279.5350.548>.

- (89) Grundner, M.; Halbritter, J. XPS and AES Studies on Oxide Growth and Oxide Coatings on Niobium. *Journal of Applied Physics* **1980**, *51* (1), 397–405. <https://doi.org/10.1063/1.327386>.
- (90) Hu, Z. P.; Li, Y. P.; Ji, M. R.; Wu, J. X. The Interaction of Oxygen with Niobium Studied by XPS and UPS. *Solid State Communications* **1989**, *71* (10), 849–852. [https://doi.org/10.1016/0038-1098\(89\)90210-X](https://doi.org/10.1016/0038-1098(89)90210-X).
- (91) Murayama, T.; Chen, J.; Hirata, J.; Matsumoto, K.; Ueda, W. Hydrothermal Synthesis of Octahedra-Based Layered Niobium Oxide and Its Catalytic Activity as a Solid Acid. *Catal. Sci. Technol.* **2014**, *4* (12), 4250–4257. <https://doi.org/10.1039/C4CY00713A>.
- (92) Kreissl, H. T.; Li, M. M. J.; Peng, Y.-K.; Nakagawa, K.; Hooper, T. J. N.; Hanna, J. V.; Shepherd, A.; Wu, T.-S.; Soo, Y.-L.; Tsang, S. C. E. Structural Studies of Bulk to Nanosize Niobium Oxides with Correlation to Their Acidity. *J. Am. Chem. Soc.* **2017**, *139* (36), 12670–12680. <https://doi.org/10.1021/jacs.7b06856>.
- (93) Platon, A.; Thomson, W. J. Quantitative Lewis/Brønsted Ratios Using DRIFTS. *Ind. Eng. Chem. Res.* **2003**, *42* (24), 5988–5992. <https://doi.org/10.1021/ie030343g>.
- (94) Nakajima, K.; Baba, Y.; Noma, R.; Kitano, M.; N. Kondo, J.; Hayashi, S.; Hara, M. Nb₂O₅·nH₂O as a Heterogeneous Catalyst with Water-Tolerant Lewis Acid Sites. *J. Am. Chem. Soc.* **2011**, *133* (12), 4224–4227. <https://doi.org/10.1021/ja110482r>.
- (95) Zhuravlev, L. T. The Surface Chemistry of Amorphous Silica. Zhuravlev Model. *Colloids and Surfaces A: Physicochemical and Engineering Aspects* **2000**, *173* (1), 1–38. [https://doi.org/10.1016/S0927-7757\(00\)00556-2](https://doi.org/10.1016/S0927-7757(00)00556-2).
- (96) Rascón, F.; Wischert, R.; Copéret, C. Molecular Nature of Support Effects in Single-Site Heterogeneous Catalysts : Silica vs. Alumina. *Chemical Science* **2011**, *2* (8), 1449–1456. <https://doi.org/10.1039/C1SC00073J>.
- (97) García-Sancho, C.; Agirrezabal-Telleria, I.; Güemez, M. B.; Maireles-Torres, P. Dehydration of D-Xylose to Furfural Using Different Supported Niobia Catalysts. *Applied Catalysis B: Environmental* **2014**, *152–153*, 1–10. <https://doi.org/10.1016/j.apcatb.2014.01.013>.
- (98) Gupta, N. K.; Fukuoka, A.; Nakajima, K. Amorphous Nb₂O₅ as a Selective and Reusable Catalyst for Furfural Production from Xylose in Biphasic Water and Toluene. *ACS Catal.* **2017**, *7* (4), 2430–2436. <https://doi.org/10.1021/acscatal.6b03682>.
- (99) García-Sancho, C.; Sádaba, I.; Moreno-Tost, R.; Mérida-Robles, J.; Santamaría-González, J.; López-Granados, M.; Maireles-Torres, P. Dehydration of Xylose to Furfural over MCM-41-Supported Niobium-Oxide Catalysts. *ChemSusChem* **6** (4), 635–642. <https://doi.org/10.1002/cssc.201200881>.
- (100) Choudhary, V.; Sandler, S. I.; Vlachos, D. G. Conversion of Xylose to Furfural Using Lewis and Brønsted Acid Catalysts in Aqueous Media. *ACS Catal.* **2012**, *2* (9), 2022–2028. <https://doi.org/10.1021/cs300265d>.
- (101) Choudhary, V.; Pinar, A. B.; Sandler, S. I.; Vlachos, D. G.; Lobo, R. F. Xylose Isomerization to Xylulose and Its Dehydration to Furfural in Aqueous Media. *ACS Catal.* **2011**, *1* (12), 1724–1728. <https://doi.org/10.1021/cs200461t>.
- (102) Weingarten, R.; Tompsett, G. A.; Conner, W. C.; Huber, G. W. Design of Solid Acid Catalysts for Aqueous-Phase Dehydration of Carbohydrates: The Role of Lewis and

- Brønsted Acid Sites. *Journal of Catalysis* **2011**, 279 (1), 174–182. <https://doi.org/10.1016/j.jcat.2011.01.013>.
- (103) Gürbüz, E. I.; Gallo, J. M. R.; Alonso, D. M.; Wettstein, S. G.; Lim, W. Y.; Dumesic, J. A. Conversion of Hemicellulose into Furfural Using Solid Acid Catalysts in γ -Valerolactone. *Angewandte Chemie International Edition* **2013**, 52 (4), 1270–1274. <https://doi.org/10.1002/anie.201207334>.
- (104) Wada, E.; Kitano, M.; Nakajima, K.; Hara, M. Effect of Preparation Conditions on the Structural and Acid Catalytic Properties of Protonated Titanate Nanotubes. *J. Mater. Chem. A* **2013**, 1 (41), 12768–12774. <https://doi.org/10.1039/C3TA13015K>.
- (105) Narender, N.; Mohan, K. V. V. K.; Kulkarni, S. J.; Reddy, I. A. K. Liquid Phase Benzylolation of Benzene and Toluene with Benzyl Alcohol over Modified Zeolites. *Catalysis Communications* **2006**, 7 (8), 583–588. <https://doi.org/10.1016/j.catcom.2006.01.013>.
- (106) Takagaki, A.; Lu, D.; Kondo, J. N.; Hara, M.; Hayashi, S.; Domen, K. Exfoliated HNb_3O_8 Nanosheets as a Strong Protonic Solid Acid. *Chem. Mater.* **2005**, 17 (10), 2487–2489. <https://doi.org/10.1021/cm047990y>.
- (107) Bokade, V. V.; Yadav, G. D. Synthesis of Pharmaceutical Intermediates by Toluene Benzylolation over Heteropoly Acids on Different Support. *Journal of Natural Gas Chemistry* **2007**, 16 (2), 186–192. [https://doi.org/10.1016/S1003-9953\(07\)60046-2](https://doi.org/10.1016/S1003-9953(07)60046-2).
- (108) Khadilkar, B. M.; Borkar, S. D. Environmentally Clean Synthesis of Diphenylmethanes Using Silica Gel-Supported ZnCl_2 and FeCl_3 . *Journal of Chemical Technology & Biotechnology* **1998**, 71 (3), 209–212. [https://doi.org/10.1002/\(SICI\)1097-4660\(199803\)71:3<209::AID-JCTB786>3.0.CO;2-Z](https://doi.org/10.1002/(SICI)1097-4660(199803)71:3<209::AID-JCTB786>3.0.CO;2-Z).
- (109) Datka, J.; Turek, A. M.; Jehng, J. M.; Wachs, I. E. Acidic Properties of Supported Niobium Oxide Catalysts: An Infrared Spectroscopy Investigation. *Journal of Catalysis* **1992**, 135 (1), 186–199. [https://doi.org/10.1016/0021-9517\(92\)90279-Q](https://doi.org/10.1016/0021-9517(92)90279-Q).
- (110) N. Rashed, M.; H. Siddiki, S. M. A.; A. Ali, M.; K. Moromi, S.; S. Touchy, A.; Kon, K.; Toyao, T.; Shimizu, K. Heterogeneous Catalysts for the Cyclization of Dicarboxylic Acids to Cyclic Anhydrides as Monomers for Bioplastic Production. *Green Chemistry* **2017**, 19 (14), 3238–3242. <https://doi.org/10.1039/C7GC00538E>.
- (111) Takagaki, A.; Sugisawa, M.; Lu, D.; Kondo, J. N.; Hara, M.; Domen, K.; Hayashi, S. Exfoliated Nanosheets as a New Strong Solid Acid Catalyst. *J. Am. Chem. Soc.* **2003**, 125 (18), 5479–5485. <https://doi.org/10.1021/ja034085q>.
- (112) Takagaki, A.; Tagusagawa, C.; Hayashi, S.; Hara, M.; Domen, K. Nanosheets as Highly Active Solid Acid Catalysts for Green Chemical Syntheses. *Energy Environ. Sci.* **2010**, 3 (1), 82–93. <https://doi.org/10.1039/B918563A>.
- (113) Du, Y.-P.; Héroguel, F.; Luterbacher, J. S. Slowing the Kinetics of Alumina Sol–Gel Chemistry for Controlled Catalyst Overcoating and Improved Catalyst Stability and Selectivity. *Small* **2018**, 14 (34), 1801733. <https://doi.org/10.1002/smll.201801733>.
- (114) Yoshinaga, I.; Yamada, N.; Katayama, S. Effect of Inorganic Components on Thermal Stability of Methylsiloxane-Based Inorganic/Organic Hybrids. *J Sol-Gel Sci Technol* **2005**, 35 (1), 21–26. <https://doi.org/10.1007/s10971-005-3211-2>.

- (115) Scanlon, J. T.; Willis, D. E. Calculation of Flame Ionization Detector Relative Response Factors Using the Effective Carbon Number Concept. *J Chromatogr Sci* **1985**, 23 (8), 333–340. <https://doi.org/10.1093/chromsci/23.8.333>.
- (116) Lu, J.; Liu, B.; Greeley, J. P.; Feng, Z.; Libera, J. A.; Lei, Y.; Bedzyk, M. J.; Stair, P. C.; Elam, J. W. Porous Alumina Protective Coatings on Palladium Nanoparticles by Self-Poisoned Atomic Layer Deposition. *Chem. Mater.* **2012**, 24 (11), 2047–2055. <https://doi.org/10.1021/cm300203s>.
- (117) Schubert, U.; Huesing, N.; Lorenz, A. Hybrid Inorganic-Organic Materials by Sol-Gel Processing of Organofunctional Metal Alkoxides. *Chem. Mater.* **1995**, 7 (11), 2010–2027. <https://doi.org/10.1021/cm00059a007>.
- (118) Breitscheidel, B.; Zieder, J.; Schubert, U. Metal Complexes in Inorganic Matrixes. 7. Nanometer-Sized, Uniform Metal Particles in a Silica Matrix by Sol-Gel Processing of Metal Complexes. *Chem. Mater.* **1991**, 3 (3), 559–566. <https://doi.org/10.1021/cm00015a037>.
- (119) Chiang, Y.-D.; Dutta, S.; Chen, C.-T.; Huang, Y.-T.; Lin, K.-S.; Wu, J. C. S.; Suzuki, N.; Yamauchi, Y.; Wu, K. C.-W. Functionalized Fe₃O₄@Silica Core–Shell Nanoparticles as Microalgae Harvester and Catalyst for Biodiesel Production. *ChemSusChem* **2015**, 8 (5), 789–794. <https://doi.org/10.1002/cssc.201402996>.
- (120) Du, Y.-P.; Héroguel, F.; Trung Nguyen, X.; S. Luterbacher, J. Post-Synthesis Deposition of Mesoporous Niobic Acid with Improved Thermal Stability by Kinetically Controlled Sol–Gel Overcoating. *Journal of Materials Chemistry A* **2019**. <https://doi.org/10.1039/C9TA01459D>.
- (121) Yamada, K.; Chow, T. Y.; Horihata, T.; Nagata, M. A Low Temperature Synthesis of Zirconium Oxide Coating Using Chelating Agents. *Journal of Non-Crystalline Solids* **1988**, 100 (1), 316–320. [https://doi.org/10.1016/0022-3093\(88\)90039-7](https://doi.org/10.1016/0022-3093(88)90039-7).
- (122) Soled, S. Case Studies of Nobel-Metal Catalysts. In *Synthesis of Solid Catalysts*; John Wiley & Sons, Ltd, 2009; pp 353–367. <https://doi.org/10.1002/9783527626854.ch16>.
- (123) Ding, K.; Cullen, D. A.; Zhang, L.; Cao, Z.; Roy, A. D.; Ivanov, I. N.; Cao, D. A General Synthesis Approach for Supported Bimetallic Nanoparticles via Surface Inorganometallic Chemistry. *Science* **2018**, 362 (6414), 560–564. <https://doi.org/10.1126/science.aau4414>.
- (124) Cheng, N.; Banis, M. N.; Liu, J.; Riese, A.; Li, X.; Li, R.; Ye, S.; Knights, S.; Sun, X. Extremely Stable Platinum Nanoparticles Encapsulated in a Zirconia Nanocage by Area-Selective Atomic Layer Deposition for the Oxygen Reduction Reaction. *Advanced Materials* **2015**, 27 (2), 277–281. <https://doi.org/10.1002/adma.201404314>.
- (125) Du, Y.-P.; Luterbacher, J. S. Designing Heterogeneous Catalysts for Renewable Catalysis Applications Using Metal Oxide Deposition. *CHIMIA International Journal for Chemistry* **2019**, 73 (9), 698–706. <https://doi.org/10.2533/chimia.2019.698>.
- (126) Liu, S.; Tan, J. M.; Gulec, A.; Crosby, L. A.; Drake, T. L.; Schweitzer, N. M.; Delferro, M.; Marks, L. D.; Marks, T. J.; Stair, P. C. Stabilizing Single-Atom and Small-Domain Platinum via Combining Organometallic Chemisorption and Atomic Layer Deposition. *Organometallics* **2017**, 36 (4), 818–828. <https://doi.org/10.1021/acs.organomet.6b00869>.

- (127) Toebes, M. L.; van Dillen, J. A.; de Jong, K. P. Synthesis of Supported Palladium Catalysts. *Journal of Molecular Catalysis A: Chemical* **2001**, *173* (1), 75–98. [https://doi.org/10.1016/S1381-1169\(01\)00146-7](https://doi.org/10.1016/S1381-1169(01)00146-7).
- (128) Kim, M.-Y.; Kyriakidou, E. A.; Choi, J.-S.; Toops, T. J.; Binder, A. J.; Thomas, C.; Parks, J. E.; Schwartz, V.; Chen, J.; Hensley, D. K. Enhancing Low-Temperature Activity and Durability of Pd-Based Diesel Oxidation Catalysts Using ZrO₂ Supports. *Applied Catalysis B: Environmental* **2016**, *187*, 181–194. <https://doi.org/10.1016/j.apcatb.2016.01.023>.
- (129) Zhang, H.; Gu, X.-K.; Canlas, C.; Kropf, A. J.; Aich, P.; Greeley, J. P.; Elam, J. W.; Meyers, R. J.; Dumesic, J. A.; Stair, P. C.; et al. Atomic Layer Deposition Overcoating: Tuning Catalyst Selectivity for Biomass Conversion. *Angewandte Chemie International Edition* **2014**, *53* (45), 12132–12136. <https://doi.org/10.1002/anie.201407236>.
- (130) Liang, H.; Zhang, B.; Ge, H.; Gu, X.; Zhang, S.; Qin, Y. Porous TiO₂/Pt/TiO₂ Sandwich Catalyst for Highly Selective Semihydrogenation of Alkyne to Olefin. *ACS Catal.* **2017**, *7* (10), 6567–6572. <https://doi.org/10.1021/acscatal.7b02032>.
- (131) Cargnello, M.; Jaén, J. J. D.; Garrido, J. C. H.; Bakhmutsky, K.; Montini, T.; Gámez, J. J. C.; Gorte, R. J.; Fornasiero, P. Exceptional Activity for Methane Combustion over Modular Pd@CeO₂ Subunits on Functionalized Al₂O₃. *Science* **2012**, *337* (6095), 713–717. <https://doi.org/10.1126/science.1222887>.
- (132) Hackett, S. F. J.; Brydson, R. M.; Gass, M. H.; Harvey, I.; Newman, A. D.; Wilson, K.; Lee, A. F. High-Activity, Single-Site Mesoporous Pd/Al₂O₃ Catalysts for Selective Aerobic Oxidation of Allylic Alcohols. *Angewandte Chemie* **2007**, *119* (45), 8747–8750. <https://doi.org/10.1002/ange.200702534>.
- (133) Kattel, S.; Liu, P.; Chen, J. G. Tuning Selectivity of CO₂ Hydrogenation Reactions at the Metal/Oxide Interface. *J. Am. Chem. Soc.* **2017**, *139* (29), 9739–9754. <https://doi.org/10.1021/jacs.7b05362>.
- (134) Kwak, J. H.; Kovarik, L.; Szanyi, J. Heterogeneous Catalysis on Atomically Dispersed Supported Metals: CO₂ Reduction on Multifunctional Pd Catalysts. *ACS Catal.* **2013**, *3* (9), 2094–2100. <https://doi.org/10.1021/cs4001392>.
- (135) Park, J.-N.; McFarland, E. W. A Highly Dispersed Pd–Mg/SiO₂ Catalyst Active for Methanation of CO₂. *Journal of Catalysis* **2009**, *266* (1), 92–97. <https://doi.org/10.1016/j.jcat.2009.05.018>.
- (136) Kattel, S.; Yan, B.; Chen, J. G.; Liu, P. CO₂ Hydrogenation on Pt, Pt/SiO₂ and Pt/TiO₂: Importance of Synergy between Pt and Oxide Support. *Journal of Catalysis* **2016**, *343*, 115–126. <https://doi.org/10.1016/j.jcat.2015.12.019>.
- (137) Wang, X.; Shi, H.; Kwak, J. H.; Szanyi, J. Mechanism of CO₂ Hydrogenation on Pd/Al₂O₃ Catalysts: Kinetics and Transient DRIFTS-MS Studies. *ACS Catal.* **2015**, *5* (11), 6337–6349. <https://doi.org/10.1021/acscatal.5b01464>.
- (138) Bibby, D. M.; Howe, R. F.; McLellan, G. D. Coke Formation in High-Silica Zeolites. *Applied Catalysis A: General* **1992**, *93* (1), 1–34. [https://doi.org/10.1016/0926-860X\(92\)80291-J](https://doi.org/10.1016/0926-860X(92)80291-J).
- (139) Wang, J.; Li, G.; Li, Z.; Tang, C.; Feng, Z.; An, H.; Liu, H.; Liu, T.; Li, C. A Highly Selective and Stable ZnO–ZrO₂ Solid Solution Catalyst for CO₂ Hydrogenation to

- Methanol. *Science Advances* **2017**, *3* (10), e1701290. <https://doi.org/10.1126/sciadv.1701290>.
- (140) Samson, K.; Śliwa, M.; Socha, R. P.; Góra-Marek, K.; Mucha, D.; Rutkowska-Zbik, D.; Paul, J.-F.; Ruggiero-Mikołajczyk, M.; Grabowski, R.; Słoczyński, J. Influence of ZrO₂ Structure and Copper Electronic State on Activity of Cu/ZrO₂ Catalysts in Methanol Synthesis from CO₂. *ACS Catal.* **2014**, *4* (10), 3730–3741. <https://doi.org/10.1021/cs500979c>.
- (141) Li, K.; Chen, J. G. CO₂ Hydrogenation to Methanol over ZrO₂-Containing Catalysts: Insights into ZrO₂ Induced Synergy. *ACS Catal.* **2019**, *9* (9), 7840–7861. <https://doi.org/10.1021/acscatal.9b01943>.
- (142) Petrov, A. W.; Ferri, D.; Tarik, M.; Kröcher, O.; Bokhoven, J. A. van. Deactivation Aspects of Methane Oxidation Catalysts Based on Palladium and ZSM-5. *Top Catal* **2017**, *60* (1–2), 123–130. <https://doi.org/10.1007/s11244-016-0724-6>.
- (143) Moulijn, J. A.; van Diepen, A. E.; Kapteijn, F. Catalyst Deactivation: Is It Predictable?: What to Do? *Applied Catalysis A: General* **2001**, *212* (1), 3–16. [https://doi.org/10.1016/S0926-860X\(00\)00842-5](https://doi.org/10.1016/S0926-860X(00)00842-5).
- (144) Hu, K.-J.; Plant, S. R.; Ellis, P. R.; Brown, C. M.; Bishop, P. T.; Palmer, R. E. Atomic Resolution Observation of a Size-Dependent Change in the Ripening Modes of Mass-Selected Au Nanoclusters Involved in CO Oxidation. *J. Am. Chem. Soc.* **2015**, *137* (48), 15161–15168. <https://doi.org/10.1021/jacs.5b08720>.
- (145) Gilroy, K. D.; Elnabawy, A. O.; Yang, T.-H.; Roling, L. T.; Howe, J.; Mavrikakis, M.; Xia, Y. Thermal Stability of Metal Nanocrystals: An Investigation of the Surface and Bulk Reconstructions of Pd Concave Icosahedra. *Nano Lett.* **2017**, *17* (6), 3655–3661. <https://doi.org/10.1021/acs.nanolett.7b00844>.
- (146) Bahmanpour, A. M.; Héroguel, F.; Kılıç, M.; Baranowski, C. J.; Artiglia, L.; Röthlisberger, U.; Luterbacher, J. S.; Kröcher, O. Cu–Al Spinel as a Highly Active and Stable Catalyst for the Reverse Water Gas Shift Reaction. *ACS Catal.* **2019**, *9* (7), 6243–6251. <https://doi.org/10.1021/acscatal.9b01822>.
- (147) Aitbekova, A.; Wu, L.; Wrasman, C. J.; Boubnov, A.; Hoffman, A. S.; Goodman, E. D.; Bare, S. R.; Cargnello, M. Low-Temperature Restructuring of CeO₂-Supported Ru Nanoparticles Determines Selectivity in CO₂ Catalytic Reduction. *J. Am. Chem. Soc.* **2018**, *140* (42), 13736–13745. <https://doi.org/10.1021/jacs.8b07615>.
- (148) Wang, C.; Guan, E.; Wang, L.; Chu, X.; Wu, Z.; Zhang, J.; Yang, Z.; Jiang, Y.; Zhang, L.; Meng, X.; et al. Product Selectivity Controlled by Nanoporous Environments in Zeolite Crystals Enveloping Rhodium Nanoparticle Catalysts for CO₂ Hydrogenation. *J. Am. Chem. Soc.* **2019**, *141* (21), 8482–8488. <https://doi.org/10.1021/jacs.9b01555>.
- (149) Chen, X.; Su, X.; Su, H.-Y.; Liu, X.; Miao, S.; Zhao, Y.; Sun, K.; Huang, Y.; Zhang, T. Theoretical Insights and the Corresponding Construction of Supported Metal Catalysts for Highly Selective CO₂ to CO Conversion. *ACS Catal.* **2017**, *7* (7), 4613–4620. <https://doi.org/10.1021/acscatal.7b00903>.
- (150) Matsubu, J. C.; Yang, V. N.; Christopher, P. Isolated Metal Active Site Concentration and Stability Control Catalytic CO₂ Reduction Selectivity. *J. Am. Chem. Soc.* **2015**, *137* (8), 3076–3084. <https://doi.org/10.1021/ja5128133>.

- (151) Kwak, J. H.; Kovarik, L.; Szanyi, J. CO₂ Reduction on Supported Ru/Al₂O₃ Catalysts: Cluster Size Dependence of Product Selectivity. *ACS Catal.* **2013**, *3* (11), 2449–2455. <https://doi.org/10.1021/cs400381f>.
- (152) Matsubu, J. C.; Zhang, S.; DeRita, L.; Marinkovic, N. S.; Chen, J. G.; Graham, G. W.; Pan, X.; Christopher, P. Adsorbate-Mediated Strong Metal–Support Interactions in Oxide-Supported Rh Catalysts. *Nature Chemistry* **2017**, *9* (2), 120–127. <https://doi.org/10.1038/nchem.2607>.
- (153) Cerrato, G.; Bordiga, S.; Barbera, S.; Morterra, C. Surface Characterization of Monoclinic ZrO₂: I. Morphology, FTIR Spectral Features, and Computer Modelling. *Applied Surface Science* **1997**, *115* (1), 53–65. [https://doi.org/10.1016/S0169-4332\(96\)00586-7](https://doi.org/10.1016/S0169-4332(96)00586-7).
- (154) Kattel, S.; Yan, B.; Yang, Y.; Chen, J. G.; Liu, P. Optimizing Binding Energies of Key Intermediates for CO₂ Hydrogenation to Methanol over Oxide-Supported Copper. *J. Am. Chem. Soc.* **2016**, *138* (38), 12440–12450. <https://doi.org/10.1021/jacs.6b05791>.
- (155) Bhattacharyya, K.; Danon, A.; K. Vijayan, B.; Gray, K. A.; Stair, P. C.; Weitz, E. Role of the Surface Lewis Acid and Base Sites in the Adsorption of CO₂ on Titania Nanotubes and Platinized Titania Nanotubes: An in Situ FT-IR Study. *J. Phys. Chem. C* **2013**, *117* (24), 12661–12678. <https://doi.org/10.1021/jp402979m>.
- (156) Ren, J.; Guo, H.; Yang, J.; Qin, Z.; Lin, J.; Li, Z. Insights into the Mechanisms of CO₂ Methanation on Ni(111) Surfaces by Density Functional Theory. *Applied Surface Science* **2015**, *351*, 504–516. <https://doi.org/10.1016/j.apsusc.2015.05.173>.
- (157) Huygh, S.; Bogaerts, A.; Neyts, E. C. How Oxygen Vacancies Activate CO₂ Dissociation on TiO₂ Anatase (001). *J. Phys. Chem. C* **2016**, *120* (38), 21659–21669. <https://doi.org/10.1021/acs.jpcc.6b07459>.
- (158) Zhang, X.; Zhu, X.; Lin, L.; Yao, S.; Zhang, M.; Liu, X.; Wang, X.; Li, Y.-W.; Shi, C.; Ma, D. Highly Dispersed Copper over β-Mo₂C as an Efficient and Stable Catalyst for the Reverse Water Gas Shift (RWGS) Reaction. *ACS Catal.* **2017**, *7* (1), 912–918. <https://doi.org/10.1021/acscatal.6b02991>.
- (159) Baxter, E. T.; Ha, M.-A.; Cass, A. C.; Alexandrova, A. N.; Anderson, S. L. Ethylene Dehydrogenation on Pt_{4,7,8} Clusters on Al₂O₃: Strong Cluster Size Dependence Linked to Preferred Catalyst Morphologies. *ACS Catal.* **2017**, *7* (5), 3322–3335. <https://doi.org/10.1021/acscatal.7b00409>.
- (160) Ren, Y.; Xin, C.; Hao, Z.; Sun, H.; Bernasek, S. L.; Chen, W.; Xu, G. Q. Probing the Reaction Mechanism in CO₂ Hydrogenation on Bimetallic Ni/Cu(100) with Near-Ambient Pressure X-Ray Photoelectron Spectroscopy. *ACS Appl. Mater. Interfaces* **2020**, *12* (2), 2548–2554. <https://doi.org/10.1021/acsami.9b19523>.
- (161) Daniell, W.; Schubert, U.; Glöckler, R.; Meyer, A.; Noweck, K.; Knözinger, H. Enhanced Surface Acidity in Mixed Alumina–Silicas: A Low-Temperature FTIR Study. *Applied Catalysis A: General* **2000**, *196* (2), 247–260. [https://doi.org/10.1016/S0926-860X\(99\)00474-3](https://doi.org/10.1016/S0926-860X(99)00474-3).
- (162) Zecchina, A.; Otero Areán, C. Diatomic Molecular Probes for Mid-IR Studies of Zeolites. *Chemical Society Reviews* **1996**, *25* (3), 187–197. <https://doi.org/10.1039/CS9962500187>.

- (163) Decanio, E. C.; Edwards, J. C.; Bruno, J. W. Solid-State ^1H MAS NMR Characterization of γ -Alumina and Modified γ -Aluminas. *Journal of Catalysis* **1994**, *148* (1), 76–83. <https://doi.org/10.1006/jcat.1994.1187>.
- (164) Ravenelle, R. M.; Copeland, J. R.; Kim, W.-G.; Crittenden, J. C.; Sievers, C. Structural Changes of γ - Al_2O_3 -Supported Catalysts in Hot Liquid Water. *ACS Catal.* **2011**, *1* (5), 552–561. <https://doi.org/10.1021/cs1001515>.
- (165) Zaki, M. I.; Hasan, M. A.; Al-Sagheer, F. A.; Pasupulety, L. In Situ FTIR Spectra of Pyridine Adsorbed on SiO_2 - Al_2O_3 , TiO_2 , ZrO_2 and CeO_2 : General Considerations for the Identification of Acid Sites on Surfaces of Finely Divided Metal Oxides. *Colloids and Surfaces A: Physicochemical and Engineering Aspects* **2001**, *190* (3), 261–274. [https://doi.org/10.1016/S0927-7757\(01\)00690-2](https://doi.org/10.1016/S0927-7757(01)00690-2).
- (166) Liu, X. DRIFTS Study of Surface of γ -Alumina and Its Dehydroxylation. *J. Phys. Chem. C* **2008**, *112* (13), 5066–5073. <https://doi.org/10.1021/jp711901s>.
- (167) Aguado, J.; Escola, J. M.; Castro, M. C.; Paredes, B. Metathesis of 1-Hexene over Rhenium Oxide Supported on Ordered Mesoporous Aluminas: Comparison with $\text{Re}_2\text{O}_7/\gamma$ - Al_2O_3 . *Applied Catalysis A: General* **2005**, *284* (1–2), 47–57. <https://doi.org/10.1016/j.apcata.2005.01.017>.
- (168) Harriott, P. *Chemical Reactor Design*; CRC Press, 2002.
- (169) Gómez-Díaz, D.; Mejuto, J. C.; Navaza, J. M.; Rodríguez-Álvarez, A. Viscosities, Densities, Surface Tensions, and Refractive Indexes of 2,2,4-Trimethylpentane + Cyclohexane + Decane Ternary Liquid Systems at 298.15 K. *J. Chem. Eng. Data* **2002**, *47* (4), 872–875. <https://doi.org/10.1021/je010288n>.
- (170) Dynamic Viscosity of 1-Butanol from Dortmund Data Bank http://www.ddbst.com/en/EED/PCP/VIS_C39.php (accessed Mar 12, 2018).
- (171) Sastri, S. R. S.; Mohanty, S.; Rao, K. K. Liquid Volume at Normal Boiling Point. *Can. J. Chem. Eng.* **1996**, *74* (1), 170–172. <https://doi.org/10.1002/cjce.5450740122>.
- (172) Davis, M. E.; Davis, R. J. *Fundamentals of Chemical Reaction Engineering*; McGraw-Hill Higher Education: New York, NY, 2003. <https://authors.library.caltech.edu/25070/10/FundChemReaxEngCh9.pdf>.
- (173) Li, S.; Xu, Q.; Uchaker, E.; Cao, X.; Cao, G. Comparison of Amorphous, Pseudohexagonal and Orthorhombic Nb_2O_5 for High-Rate Lithium Ion Insertion. *CrystEngComm* **2016**, *18* (14), 2532–2540. <https://doi.org/10.1039/C5CE02069G>.
- (174) Kim, H. N.; Lee, S. K. Atomic Structure and Dehydration Mechanism of Amorphous Silica: Insights from ^{29}Si and ^1H Solid-State MAS NMR Study of SiO_2 Nanoparticles. *Geochimica et Cosmochimica Acta* **2013**, *120*, 39–64. <https://doi.org/10.1016/j.gca.2013.05.047>.
- (175) Weng, W.-L. Densities and Viscosities for Binary Mixtures of Anisole with 2-Butanol, 2-Methyl-1-Propanol, and 2-Methyl-2-Propanol. *J. Chem. Eng. Data* **1999**, *44* (4), 788–791. <https://doi.org/10.1021/je980283z>.
- (176) González, B.; Calvar, N.; Gómez, E.; Domínguez, Á. Density, Dynamic Viscosity, and Derived Properties of Binary Mixtures of Methanol or Ethanol with Water, Ethyl Acetate, and Methyl Acetate at $T=(293.15, 298.15, \text{ and } 303.15)\text{K}$. *The Journal of Chemical Thermodynamics* **2007**, *39* (12), 1578–1588. <https://doi.org/10.1016/j.jct.2007.05.004>.

- (177) Elements of Chemical Reaction Engineering - H. Scott Fogler - 9780133887518 (75) <https://www.pearson.ch/Informatik/PrenticeHall/EAN/9780133887518/Elements-of-Chemical-Reaction-Engineering> (accessed Nov 29, 2019).
- (178) Fuller, E. N.; Schettler, P. D.; Giddings, J. Calvin. NEW METHOD FOR PREDICTION OF BINARY GAS-PHASE DIFFUSION COEFFICIENTS. *Ind. Eng. Chem.* **1966**, 58 (5), 18–27. <https://doi.org/10.1021/ie50677a007>.
- (179) Lommerts, B. J.; Graaf, G. H.; Beenackers, A. A. C. M. Mathematical Modeling of Internal Mass Transport Limitations in Methanol Synthesis. *Chemical Engineering Science* **2000**, 55 (23), 5589–5598. [https://doi.org/10.1016/S0009-2509\(00\)00194-9](https://doi.org/10.1016/S0009-2509(00)00194-9).
- (180) Obalová, L.; Jiráťová, K.; Karásková, K.; Chromčáková, Ž. N₂O Catalytic Decomposition – From Laboratory Experiment to Industry Reactor. *Catalysis Today* **2012**, 191 (1), 116–120. <https://doi.org/10.1016/j.cattod.2012.03.045>.
- (181) Frontmatter. In *Handbook of Heterogeneous Catalysis*; John Wiley & Sons, Ltd, 2008; pp I–XIX. <https://doi.org/10.1002/9783527619474.fmatter>.

Curriculum Vitae

Yuan-Peng Du

Department of Chemical Science and Engineering

École Polytechnique Fédérale de Lausanne

EPFL SB ISIC LPDC CH H2 555 (Bâtiment CH) Station 6 CH-1015 Lausanne

Email: yuan-peng.du@epfl.ch / r02223108@ntu.edu.tw

Education

March 2016—2020 (oral exam: February 19th, public defence: April 8th)

École Polytechnique Fédérale de Lausanne (EPFL), Lausanne, Switzerland

PhD candidate in Chemical Engineering, Thesis advisor: Prof. Dr. Jeremy Luterbacher

September 2013—June 2015

National Taiwan University (NTU), Taipei, Taiwan

Master's degree in Chemistry, Thesis advisor: Prof. Dr. Jerry Chun Chung Chan

September 2009—June 2013

National Tsing Hua University (NTHU), Hsinchu, Taiwan

Bachelor's degree in Chemistry

Publications

1. **Y.-P. Du**, H.-H. Chang, S.-Y. Yang, S.-J. Huang, Y.-J. Tsai, J. J.-T. Huang, J. C. C. Chan*, Study of binding interaction between Pif80 protein fragment and aragonite. *Scientific Reports*, **2016**, 6, 30883.
2. F. Héroguel, L. Silvioli, **Y.-P. Du**, J. S. Luterbacher*, Controlled deposition of titanium oxide overcoats by non-hydrolytic sol gel for improved catalyst selectivity and stability. *Journal of Catalysis*, **2018**, 358, 50-61.

3. **Y.-P. Du**, F. Héroguel, J. S. Luterbacher*, Slowing the kinetics of alumina sol-gel chemistry for controlled catalyst overcoating and improved catalyst stability and selectivity. *Small*, **2018**, 14, 1801733.
4. **Y.-P. Du**, F. Héroguel, X. T. Nguyen, J. S. Luterbacher*, Post-synthesis deposition of mesoporous niobic acid with improved thermal stability by kinetically controlled sol-gel overcoating. *Journal of Materials Chemistry A*, **2019**, 7, 23803-2381. (selected as back cover)
5. **Y.-P. Du**, J. S. Luterbacher*, Designing heterogeneous catalysts for renewable catalysis applications using metal oxide deposition. *CHIMIA International Journal for Chemistry*, **2019**, 73 (9), 698-706.
6. **Y.-P. Du**, A. Bahmanpour, L. Milosevic, F. Héroguel, O. Kröcher, J. S. Luterbacher*, Engineering Pd-ZrO₂ interface for selective CO₂ hydrogenation by overcoating atomically dispersed pre-catalyst. *Manuscript in preparation*.
7. W. Lan, **Y.-P. Du**, F. Héroguel, J. S. Luterbacher*, Hydrogenolysis of acetal protected lignin in continuous flow-through system *Manuscript in preparation*.

Conference Presentations

Oral presentations

1. **Annual Meeting of American Institute of Chemical Engineers (AIChE)**
Pittsburgh, USA, October 2018
 Slowing the kinetics of alumina sol-gel chemistry for controlled catalyst overcoating and improved catalyst stability and selectivity.
2. **Annual Meeting of American Chemical Society (ACS)**
San Diego, USA, August 2019
 Post-synthesis deposition of mesoporous niobic acid with improved thermal stability by kinetically controlled sol-gel overcoating.

3. **Annual Meeting of Swiss Chemical Society (SCS)**

Zurich, Switzerland, September 2019

Post-synthesis deposition of mesoporous niobic acid with improved thermal stability by kinetically controlled sol-gel overcoating.

Poster presentations

1. **Annual Meeting of Taiwan Magnetic Resonance Society**

Tainan, Taiwan, January 2015

Investigation of the polymorph selectivity and aragonite binding characteristic of Pif80 peptide fragments.

2. **Graduate Student Competition in the Department of Chemistry**

National Taiwan University, Taipei, Taiwan, May 2015

Effect of Pif80 protein fragments on the mineralization process of calcium carbonate.

3. **Annual Meeting of Swiss Chemical Society (SCS)**

Bern, Switzerland, August 2017

Catalyst overcoating by non-hydrolytic sol-gel technique.

4. **Annual Meeting of Swiss Chemical Society (SCS)**

Lausanne, Switzerland, September 2018

Slowing the kinetics of alumina sol-gel chemistry for controlled catalyst overcoating and improved catalyst stability and selectivity.

Teaching Activities

Teaching assistantship

1. **Physical Chemistry Laboratory**, NTU, Spring semester, 2014
2. **Chemical Engineering Laboratory**, EPFL, Fall semesters, 2016—2018
3. **Eco-friendly production of the chemicals and process intensification**, EPFL, Spring semesters, 2017—2018

Supervision of students

1. **Undergraduate project by Zhong-Hong Guo**, Fall semester, 2014, NTU
2. **Master thesis by Luka Milošević**, Spring semester, 2019, EPFL

Academic Awards

1. **Department fellowship** from National Tsing Hua University, Fall semester, 2012
2. **Poster award** in Annual Meeting of Taiwan Magnetic Resonance Society, January 2015
3. **Poster award** in the competition of graduate students from the chemistry department of National Taiwan University, May 2015
4. **Dean's award** from National Taiwan University, June 2015
5. **Travel award** from Swiss Chemical Society, April 2019

Personal skills

1. **Language skills:** Chinese Mandarin (mother tongue), English (C1), and French (A2)
2. **Digital competences:** Microsoft office, Adobe illustrator, Origin, Chemdraw, and MATLAB
3. **Material characterization techniques:** XRD, FTIR, electron microscopy (SEM, TEM and STEM), chemisorption, physisorption, and solid-state NMR
4. **Synthesis and analytical skills:** glove box, Schlenk line, GC and HPLC
5. **High pressure reaction system:** Swagelok manipulation and Parr reactor